Thermophysical Properties of Wisconsin Rocks for Application in Geothermal Energy

by

Lauren L. Meyer

A thesis submitted in partial fulfillment of

the requirements for the degree of

Masters of Science

(Geological Engineering)

at the

University of Wisconsin-Madison

2013

Thermophysical Properties of Wisconsin Rocks for Application in Geothermal Energy

Approved

6/11/13

date

James M. Tinjum

Assistant Professor

6/11/2013

date

Dante Fratta

Associate Professor

ABSTRACT

Limited information exists about the geothermal gradient and heat capacity of the geologic formations in Wisconsin. The viability of deep (≈ 300 m) geothermal exchange systems in Wisconsin depends on the thermal properties (e.g., thermal gradient, thermal conductivity, thermal diffusivity, specific heat, and heat production) of the rock formations. To aid the evaluation of Wisconsin's heat capacity, thermal conductivity and specific heat tests were conducted in the laboratory to determine the thermal properties of a sample of Wisconsin rocks. Thermal property tests were conducted three to six times to ensure repeatability of results. In addition, quantitative X-ray diffraction (XRD) analysis was completed to determine relative mineral abundance and the corresponding calculated thermal property values for each specimen. These values were then compared to the experimental results. In the field, a novel ground source heat pump (GSHP) system, the *Deep, Insulated, Single Hole geothermal heat pump* (DISH) system was instrumented and installed to evaluate the viability of deep geothermal exchange systems in Wisconsin. However, collection and analysis of data from the DISH system must still be completed to determine system performance, efficiency, economic return and life cycle.

Samples were obtained from Wisconsin's Research Collections and Education Center though collaboration with the Wisconsin Geological and Natural History Survey (WGNHS) as well as from field sites located in central Wisconsin. Cylindrical specimens were trimmed to a diameter of 2.54 cm and length of 2.03 cm using a drill press, rock saw and surface grinder.

Using the guarded-comparative-longitudinal heat flow apparatus, thermal conductivities between 2.30 W m^{-1} K^{-1} and 6.71 W m^{-1} K^{-1} were measured. The thermal conductivity for the majority of the specimens (omitting the Barron Quartzite and St. Lawrence Dolomite) ranged between 2.30 W m^{-1} K^{-1} and 3.86 W m^{-1} K^{-1}. The Barron Quartzite had the highest thermal conductivity (6.71 W m^{-1} K^{-1}), and the St. Lawrence Dolomite had the second highest thermal conductivity (4.67 W m^{-1} K^{-1}). The thermal conductivity of the Precambrian Granites ranged from 3.10 W m^{-1} K^{-1} to 3.69 W m^{-1} K^{-1}. Sandstones ranged between 2.59 W m^{-1} K^{-1} and 3.86 W m^{-1} K^{-1}.

Using the “coffee-cup” calorimeter, specific heat values between 713 J kg^{-1} K^{-1} and 891 J kg^{-1} K^{-1} were obtained. The Tunnel City Sandstone had the highest specific heat (891 J kg^{-1} K^{-1}), and the St. Lawrence Dolomite had the second highest specific heat (872 J kg^{-1} K^{-1}). The specific heat of the Precambrian Granites ranged between 824 J kg^{-1} K^{-1} and 729 J kg^{-1} K^{-1}. Sandstones ranged between 818 J kg^{-1} K^{-1} and 891 J kg^{-1} K^{-1}.

Thermal property values obtained in the laboratory were compared to mixture-based calculated values from weighted averages based on XRD analysis and to literature. The majority of the thermal conductivity values obtained fall within the estimated range from literature and the calculated thermal conductivities values. Deviations from the expected or calculated values can be attributed to relative mineral abundances, density or porosity of the specimens.

The thermal property data was reliable based on a small-scale statistical analysis, although a thorough analysis of saturated rock thermal properties is

recommended. In addition, a parametric study should be completed to determine how strongly rock thermal properties control the ground source heat pump system design, efficiency and cost since the variation of thermal properties with rock type is small. Due to effects of anisotropies across microscopic, laboratory, and field scales, *in situ* thermal property testing methods warrant further research. Many variables affect the thermal properties of a given rock. Thus, simply selecting a value based on rock type, mineralogy, porosity or density may yield inaccurate analysis of a GSHP system.

ACKNOWLEDGEMENTS

The succeeding work was completed under the guidance of Dr. James Tinjum and Dr. Dante Fratta, to whom I owe the greatest of gratitude for their encouragement, support, and dedication to the progression of this research project. Moreover, their guidance has made my graduate experience at UW-Madison more than simply a continuation of my education, but a source of personal growth. Special thanks to Dr. Dave Hart for always providing a critical eye and for challenging me to think outside of the box. I would also like to thank Dr. William Likos for serving on my thesis committee.

I wish to extend special thanks to Xiaodong Wang for his technical assistance in the laboratory and the field, and to Joel Ballweg for assisting in the design of my experimental setup and for fabricating the equipment needed for my laboratory experiments. Additionally, thanks go to Robert Hyatt and the rest of Campbell Scientific for providing their expertise and assistance throughout the field instrumentation design and installation associated with this research project. I would also like to thank Doug Cobos and others at Decagon Devices, Inc. for providing intellectual support. To Ayşe Özdoğan-Dölçek, Andrew Ruetten and Matt Walker, I express my thanks for support during our weekly research meetings, assistance in the lab and field, and the extension of their knowledge.

I would like to dedicate the entirety of this work to my father, Bill and my mother, Nancy for their love and support, and for always believing in me. Special thanks to the rest of my family, particularly my brother Brett for proving insight,

motivation, and support throughout my graduate degree. Thanks are also extended to Christopher Bareither for supporting me through the challenging times, and for providing creative ideas and an external perspective regarding persistent laboratory complications. Lastly, thanks to all of my friends, particularly my fellow geo colleagues for their support and congeniality.

Financial support for this research was provided by the National Science Foundation, the Department of Energy, and the University of Wisconsin-Madison Innovation & Economic Development Research Program.

TABLE OF CONTENTS

LIST OF FIGURES

LIST OF TABLES

1. INTRODUCTION

Due to a lack of natural energy resources, Wisconsin's electrical energy largely comes from imported, non-renewable energy sources such as coal (62%), natural gas (9%) and nuclear power (21%) (U.S. Energy Information Administration, 2012). These fuels are imported from Canada, Louisiana, Texas, Oklahoma, Kansas, Wyoming and Illinois. The remaining 8% of Wisconsin's energy currently comes from renewable energy sources such as conventional hydroelectric power, solar, biomass, biogas and wind. Fig. 1-1 and Fig. 1-2 summarize the trend of energy use in Wisconsin between 1970 and 2009 based on fuel type and economic sector, respectively. In 2009, Wisconsin's total energy consumption decreased by approximately 5% from the previous year and only showed a net increase in energy consumption for the agricultural sector (Wisconsin Office of Energy Independence, 2010).

As shown in Table 1-1, in 2010, only 0.2×10^{12} W-hr of geothermal energy were used in residences on average in Wisconsin in comparison to the 36.6×10^{12} W-hr of natural gas, 9.0×10^{12} W-hr of petroleum (i.e. liquefied petroleum gas (LPG), distillate fuel oil, and kerosene) and 7.2×10^{12} W-hr of biomass used for heating/cooling of homes. Commercial and Industrial operations show similar distributions of resource use. Fig. 1-2 shows that the total energy consumption from the buildings we inhabit is significantly larger than that for transportation. With the adoption of innovative geothermal exchange systems, Wisconsin would lessen the

demand of imported energy and increase the potential for industrial and economic development.

Geothermal heat pump systems are considered to be an efficient and renewable energy technology for the cooling and heating of buildings and other facilities. The U.S. Environmental Protection Agency (EPA) states that geothermal heat pumps are among the most efficient heating and cooling technologies currently available and that qualified geothermal heat pumps are > 45% more energy efficient when compared to standard options (US EPA, 2013). Geothermal exchange systems use the earth as a free energy reservoir or storage medium and can be applied nearly everywhere, even in areas of low geothermal gradient (ASHRAE, 2007).

The International Ground Source Heat Pump Association (IGSHPA) states that the efficiency of geothermal exchange systems is 50% to 70% higher for heating and 20% and 40% higher for cooling than conventional systems, allowing for a significant decrease in energy costs (Wisconsin Perspective, 2006). The EPA found that GSHP can reduce energy consumption and corresponding emissions up to 44% in comparison to conventional air-source heat pumps, and up to 72% in comparison to electric resistance heating with standard air-conditioning equipment (US EPA, 1997). The EPA also found that GSHP produce the lowest carbon dioxide emissions and the lowest overall environmental cost of all residential heating and cooling technology available (US EPA, 1993). The few emissions released occur through the use of electricity to run the system and relates directly to system efficiency. Over an

average 20-year lifespan, every 100,000 residential GSHP installed saves more than 11×10^{12} W-hr of energy, 2.18×10^{9} kg of carbon equivalents, and approximately $750 million in space conditioning costs at current prices. Additionally, GSHP use 25% to 50% less electricity than conventional resistive electrical heating systems correlating to about 300% system efficiency, while conventional systems can provide no more than 100% efficiency (Department of Energy, 2013). Thus, the coefficient of performance (COP) of most GSHP is three or above, meaning that for every one energy unit put into the system, three or more energy units are returned. Fig. 1-3 shows a GSHP with an efficiency of 300% in comparison to other conventional heating and cooling systems; this comparison does not include the perspective of energy loss for the primary input energy source.

The spike in interest of alternative energies spurred growth of geothermal exchange system installations in the Midwest (Penn, 2000). Applications that use the ground as a high-capacity heat sink to supply constant-temperature fluids for direct heating and cooling or for heat pump applications are expected to grow exponentially in the coming decades. With the adoption of innovative geothermal systems, Wisconsin would lessen the demand of imported energy and increase the potential for industrial and economic development because these systems could be designed, drilled, manufactured, and installed primarily with in-state resources and talent. Geothermal exchange system design is based on the extreme entering water temperature (EWT), necessary heating and cooling load, and the thermophysical properties of the soil and/or rock. The thermophysical properties are typically

estimated for residential systems due to the high cost of running a thermal response test (TRT) (approximately $8,000) or thermal property tests (Dickie, 2010). For larger commercial or industrial systems, running a TRT can be economical due to the ability to reduce borehole field size and thus pipe length and pump size.

Some drillers with the Wisconsin Water Well Association report that over 50% of their business is now aligned with geothermal installations (Walker, 2012). Current commercial-sized geothermal exchange systems in the Madison area include the Wisconsin Institute for Discovery, Epic Systems, and the First Unitarian Church. Each of these systems uses a large numbers of shallow borings (on the order of 55 m below ground surface). Urban and residential areas, however, might benefit from deeper vertical geothermal systems due to their smaller footprints and large capacity demands. With an increase in residential, commercial and industrial use of geothermal exchange systems, Wisconsin could greatly reduce its reliance on natural gas for space conditioning and would, in turn, reduce impacts to the environment. However, limited information exists about the geothermal gradient and heat capacity of the geologic formations in Wisconsin. The viability of deep (≈ 300 m) geothermal exchange systems in Wisconsin depends on the thermal properties (e.g., thermal gradient, thermal conductivity, thermal diffusivity, specific heat, and heat production) of the rock formations.

The objective of this project is to determine the thermal properties (i.e. thermal conductivity and specific heat) of a selected group of rock formations in Wisconsin. The thermal property values obtained from this research can be used to

better characterize the geothermal heat capacity in Wisconsin as well as improve GSHP design in the state.

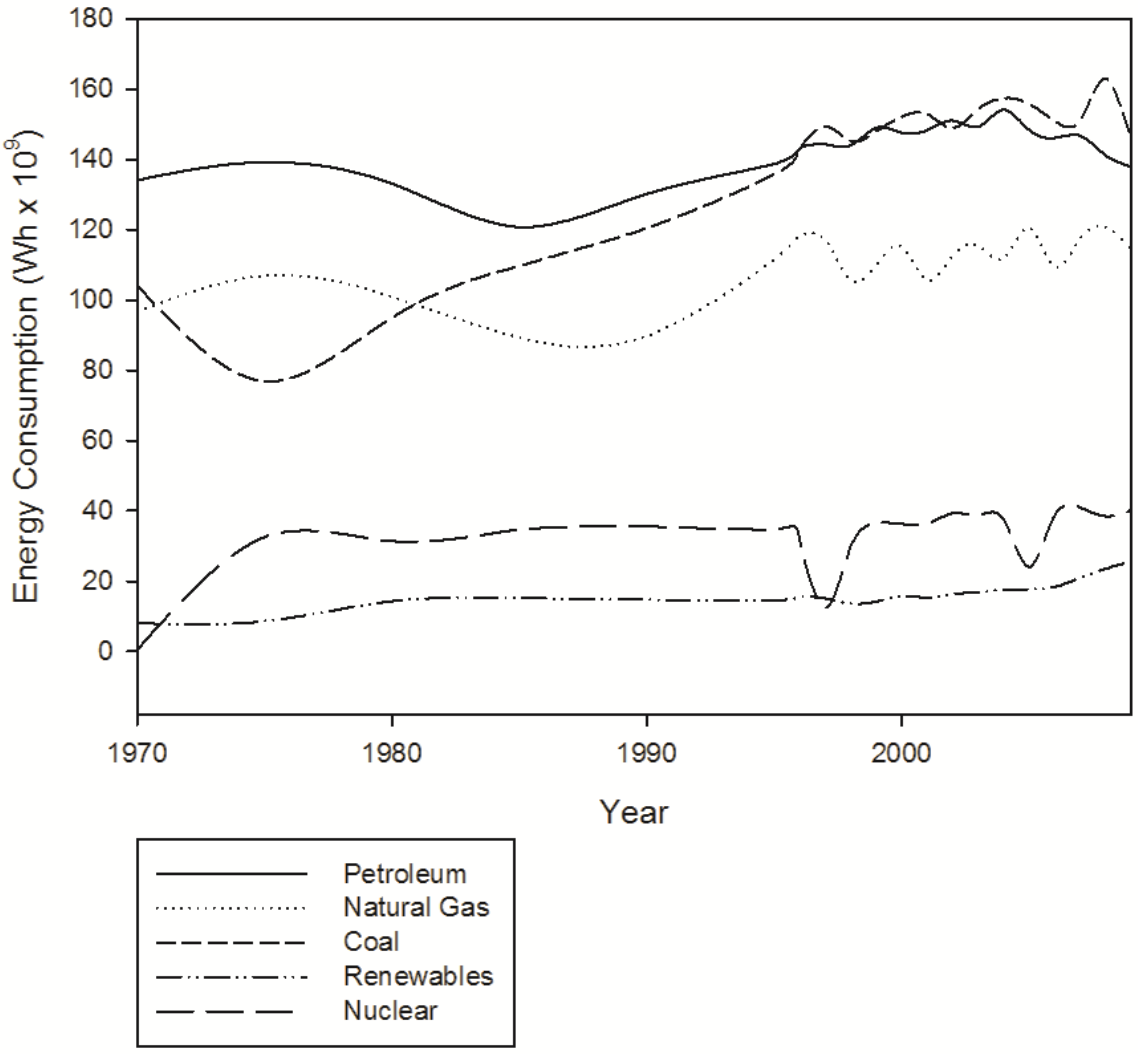

Fig. 1-1: Wisconsin energy consumption by fuel type for 1970-2009 adapted from Wisconsin Office of Energy Independence (2010).

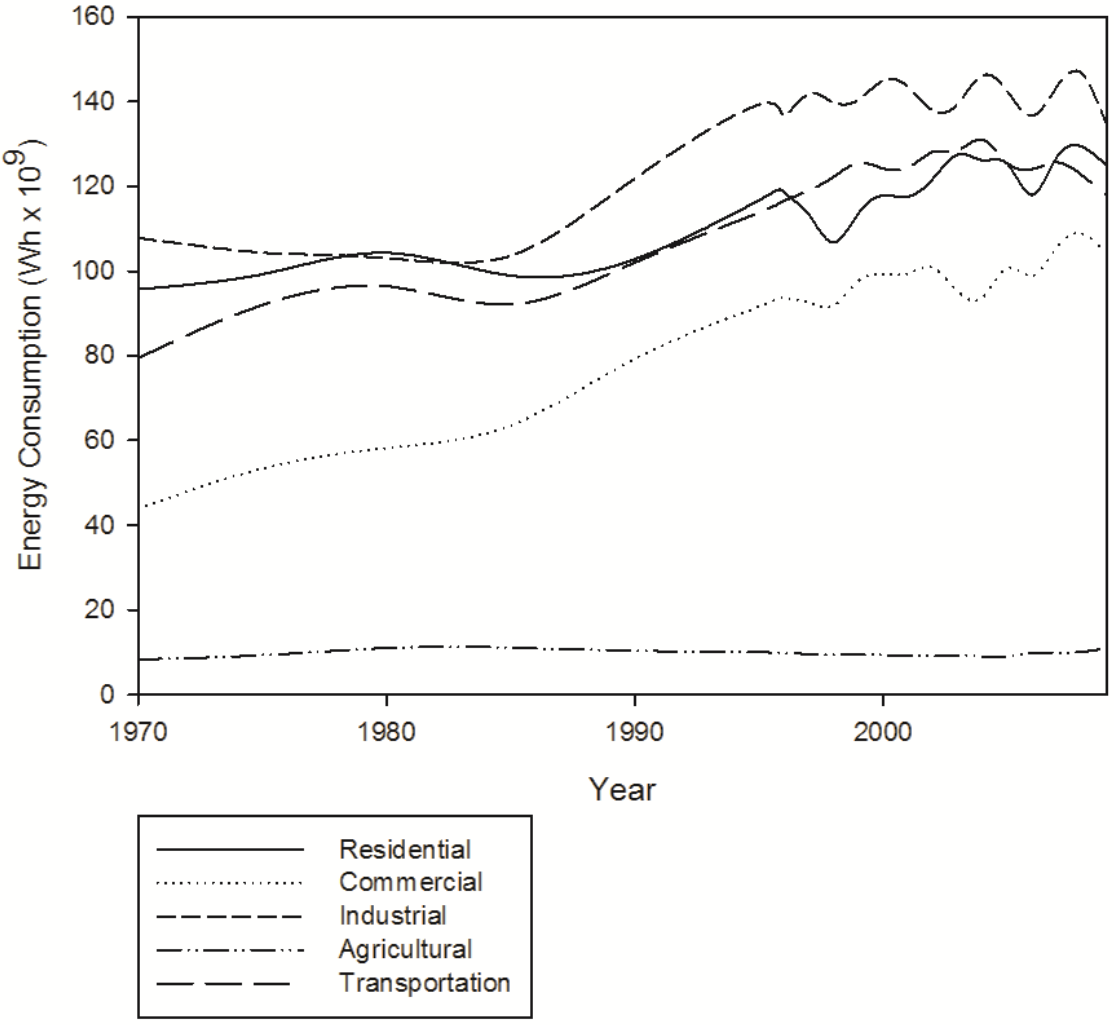

Fig. 1-2: Wisconsin energy consumption by economic sector for 1970-2009 adapted from Wisconsin Office of Energy Independence (2010).

Table 1-1: Energy consumption estimates for Wisconsin (2010) based on sector in W-hr x 10^9 adapted from U.S. Energy Information Administration (2012).

	Energy Sector			
Source	**Residential**	**Commercial**	**Industrial**	**Transportation**
Coal	0.1	0.8	10.3	0
Natural Gas	36.6	24.3	35.9	0.9
Petroleum				
Distillate Fuel Oil	1.9	1.2	6.3	32.1
Kerosene	0.1	(s)	-	-
LPG	7.0	1.0	1.2	0.2
Motor Gasoline	-	0.1	1.6	92.0
Residual Fuel Oil	-	0	0.3	0
Other	-	-	11.8	4.7
Total	9.0	2.3	21.2	129.0
Hydro-Electric Power	-	(s)	0.4	-
Biomass				
Wood	7.2	-	-	-
Wood and Waste	-	1.3	16.9	-
Losses and Co-Products	-	-	8.5	-
Geothermal	0.2	0	0	-
Solar/PV	0.1	-	-	-
Retail Electricity Sales	22.3	23.0	23.4	0.0
Net Energy	75.5	51.7	116.7	129.9
Electrical System Energy	49.9	51.4	52.5	0.0
Total	125.3	103.2	169.2	129.9

(s) - value less than 0.015 trillion W*h

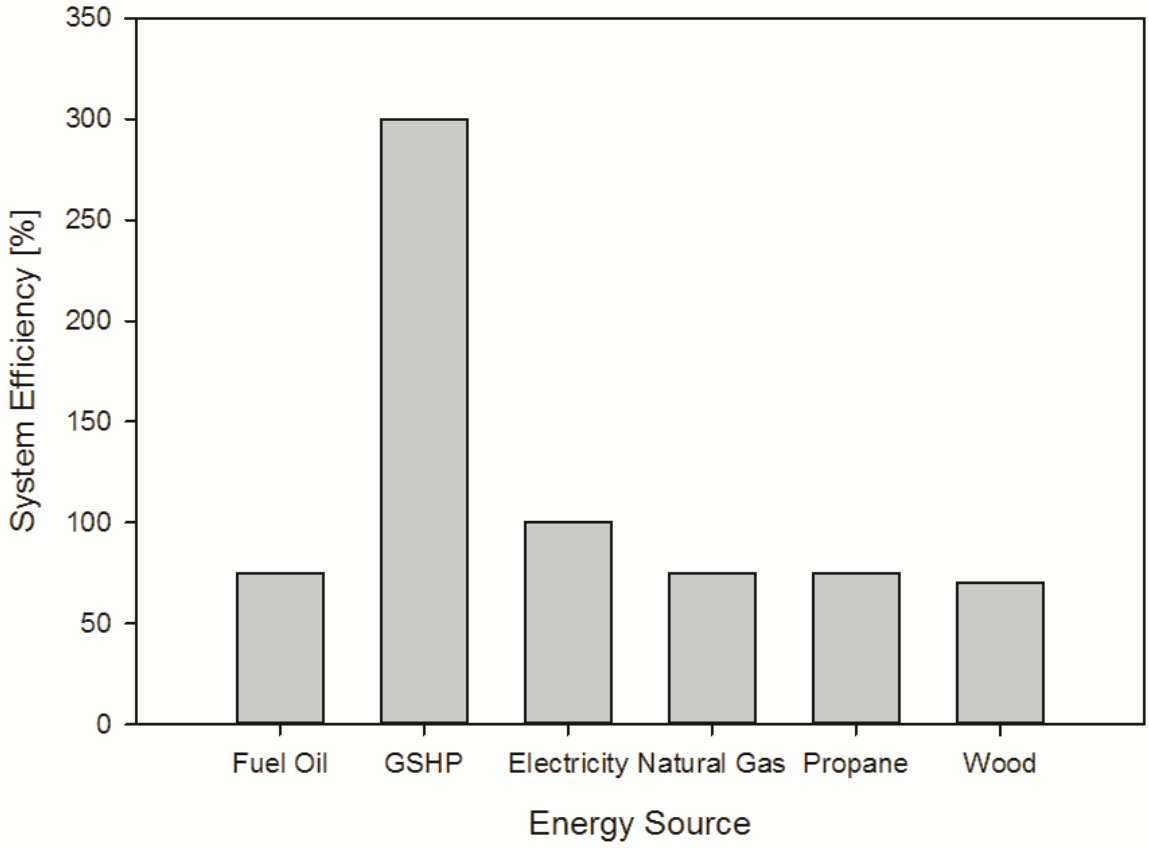

Fig. 1-3: Approximate efficiency of GSHP compared to conventional heating systems. GSHPs outperform the most efficient furnaces by over three times based on Environmental Information Administration (EIA) averages (Energy Information Administration, 2011). Plot does not include perspective of energy loss for the primary input energy source (e.g., for GSHP, the system efficiency is not reduced for losses associated with burning coal to create the electricity used or to account for transmission losses of the electrical power from point of generation to point of consumption).

2. BACKGROUND

2.1. Ground Source Heat Pumps

Ground source heat pumps use the constant temperature of the earth at depth to provide heating and cooling for residential, commercial and industrial buildings. A small energy input is needed to run a compressor and circulate water in the system; however the energy yield is typically three or four times larger than the input depending on the system COP. The heat pump transfers heat stored in the Earth into a building during the winter and out of the building during the summer.

Ground source heat pumps have three main components: (1) the earth connection, (2) heat pump, and (3) heat distribution system (ASHRAE, 2007; Omer, 2008; Lund et al., 2004). Typically, the earth connection system consists of a series of closed-loop pipes that are buried either horizontally or vertically. Fluid is circulated through these pipes allowing the heat to be transferred from the ground to the building and vice versa. For heating, the heat pump extracts heat from the circulating fluid, concentrates it and transfers heat to the building. For cooling, the process is reversed. The heat distribution system is a conventional ductwork used to distribute heated or cooled air throughout the building. For vertical closed-loop systems, heat exchange between the fluid and the ground depends on the thermal properties of the material in the borehole and the subsurface. The boreholes are typically backfilled with a thermally enhanced bentonite grout to promote heat transfer.

Assuming a heating-dominate climate, as in Wisconsin, one can roughly estimate how changes in rock thermal conductivity, λ, and bottom hole temperature

(i.e., changes in geothermal gradient) would affect GSHP design. Assuming steady state, a building load of 17500 W and an extreme borehole fluid temperature of 273.15 K, the following equation from ASHRAE (2007) was used to create trends with varying conductivity and bottom hole temperature (Fig. 2-1 and Fig. 2-2 respectively):

$$q = L \times (t_g - t_w) \times \lambda \ \text{[W]} \qquad [1]$$

where q is the heat transfer load, L is the required borehole length [m], t_g is the ground temperature [K], t_w is the borehole fluid temperature [K], and λ is in [W m^{-1} K^{-1}]. The average ground temperatures used for this analysis were estimated as bottom hole temperature, thus representing the best case scenario for the given parameters. Fig. 2-1 shows that increasing thermal conductivity results in a decrease of borehole length. Across the spectrum of 1.5 W m^{-1} K^{-1} and 7 W m^{-1} K^{-1}, the borehole length decreases from > 800 m to < 200 m. Similarly, with an increase in the bottom hole temperature (e.g., through the natural geothermal gradient), there is a decrease in borehole length. Over the typical range of bottom hole temperatures for Wisconsin (280 K to 296 K) (based on raw data from the WGNHS), borehole length decreases from > 875 m to < 305 m. Increases in bottom hole temperature can also effect the COP. Wells with higher bottom hole temperatures will have higher EWT, thus resulting in higher COP for a heating dominant climate (Fig. 2-3). Based on data from WaterFurnace International, Inc., (2012), an increase in EWT of 5 K can increase the COP by approximately 1.0.

GSHP design and performance is also sensitive to changes in specific heat, C_p. Specific heat, however, is a transient property that is more important for long-term analysis of system performance. Specific heat is a necessary parameter for modeling of geothermal systems, particularly for GSHPs which use the ground as a storage medium. To explore these effects, an analytical model based on a line source was created in MATLAB from the following equation (Eklöf & Gehlin, 1996):

$$T_q(r,t) = \frac{q}{4\pi\lambda} E_T\left(\frac{Dt}{r^2}\right) \text{ [K]} \quad [2]$$

$$E_T(\tau) = \int_{1/4\tau}^{\infty} \left(\frac{1}{s}\right)^{-s} ds \quad [3]$$

$$\tau = \frac{r^2}{Dt} \quad [4]$$

$$D = \frac{\lambda}{C_p} \quad [5]$$

where $T_q(r,t)$ is the temperature at a point r, q is the heating load [W/m], D is the diffusivity [m^2/s], t is time [s], r is the distance from the borehole [m], E_T is a function that gives the temperature change with time at the radial distance r from the borehole, and τ and s are integration parameters. Fig. 2-4 and Fig. 2-5 were created using this model and display how changes in specific heat affect the temperature of the ground at a distance of 3 m from the borehole. Both plots show that a longer time is required for a rock with a higher specific heat to transfer heat, thus reducing the rate of borehole degradation. Additionally, rocks with a higher specific heat will act as a more efficient storage medium.

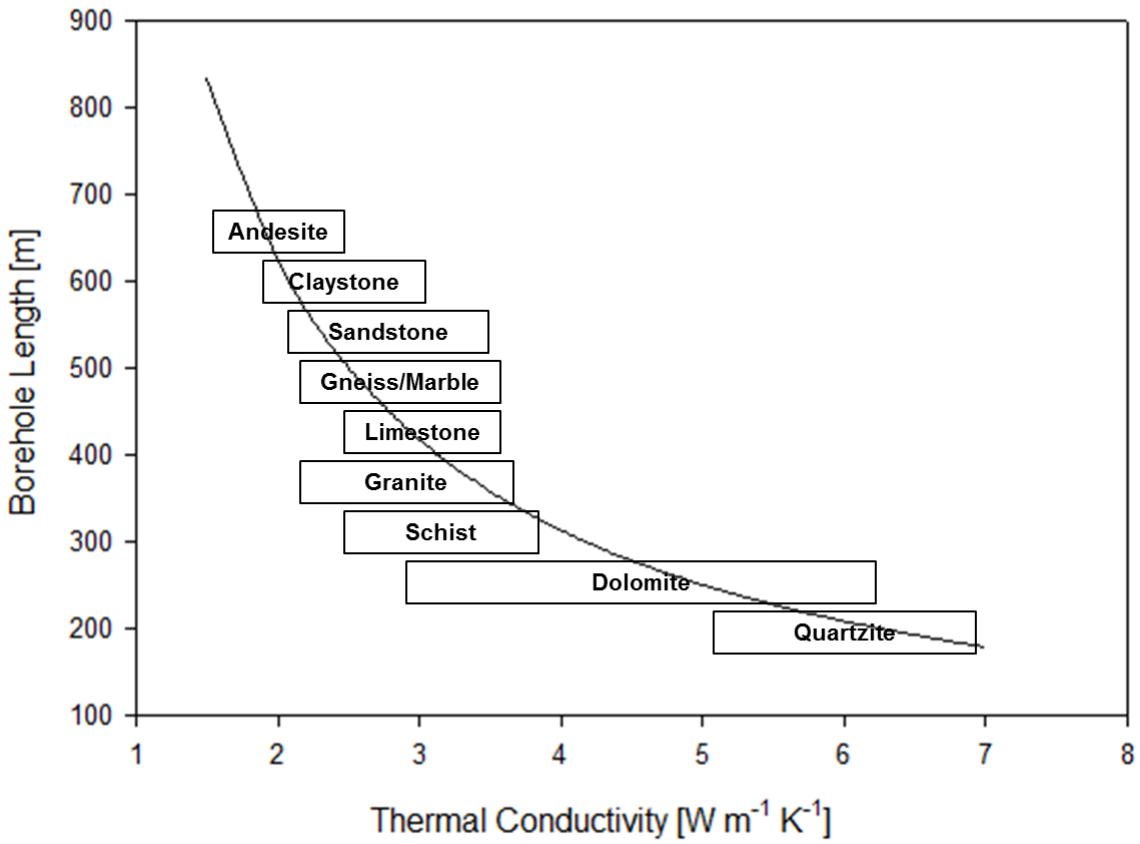

Fig. 2-1: Changes in borehole length with ground thermal conductivity assuming a constant bottom hole temperature of 287.15 K, a building load of 17500 W, and an extreme borehole fluid temperature of 273.15 K (derived from Eqn [1]).

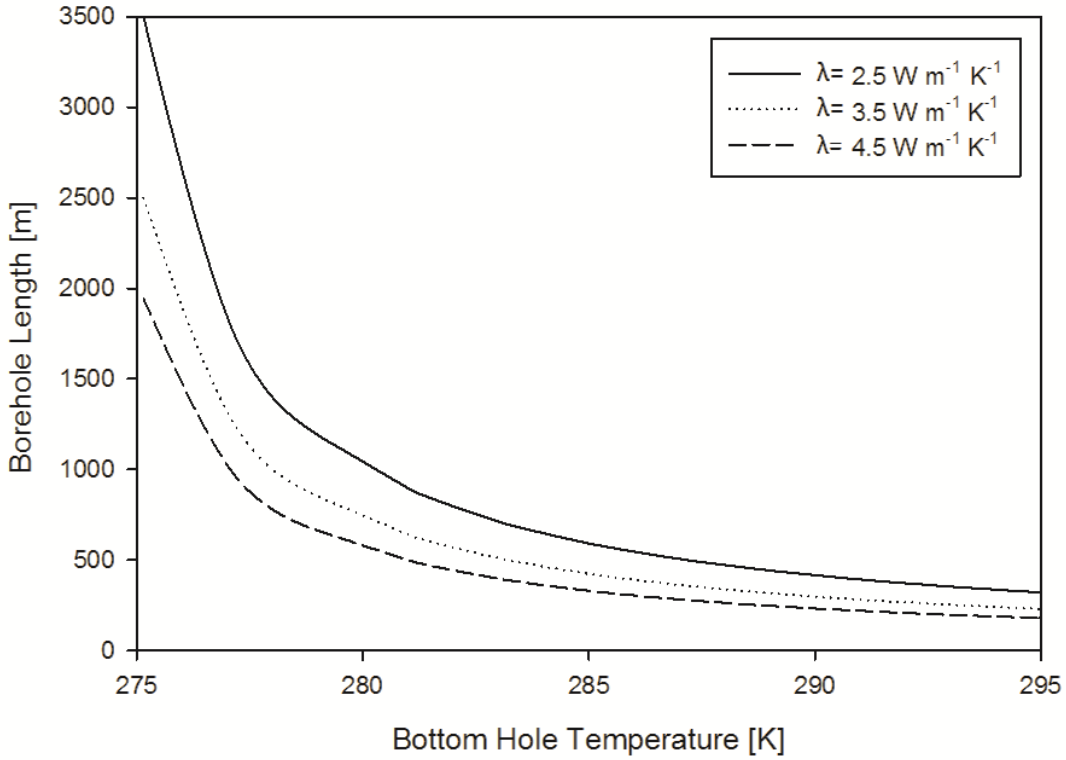

Fig. 2-2: Changes in borehole length with bottom hole temperature assuming a thermal conductivity of 2.5 W m^{-1} K^{-1}, a building load of 17500 W, and an extreme borehole fluid temperature of 273.15 K (derived from Eqn [1]).

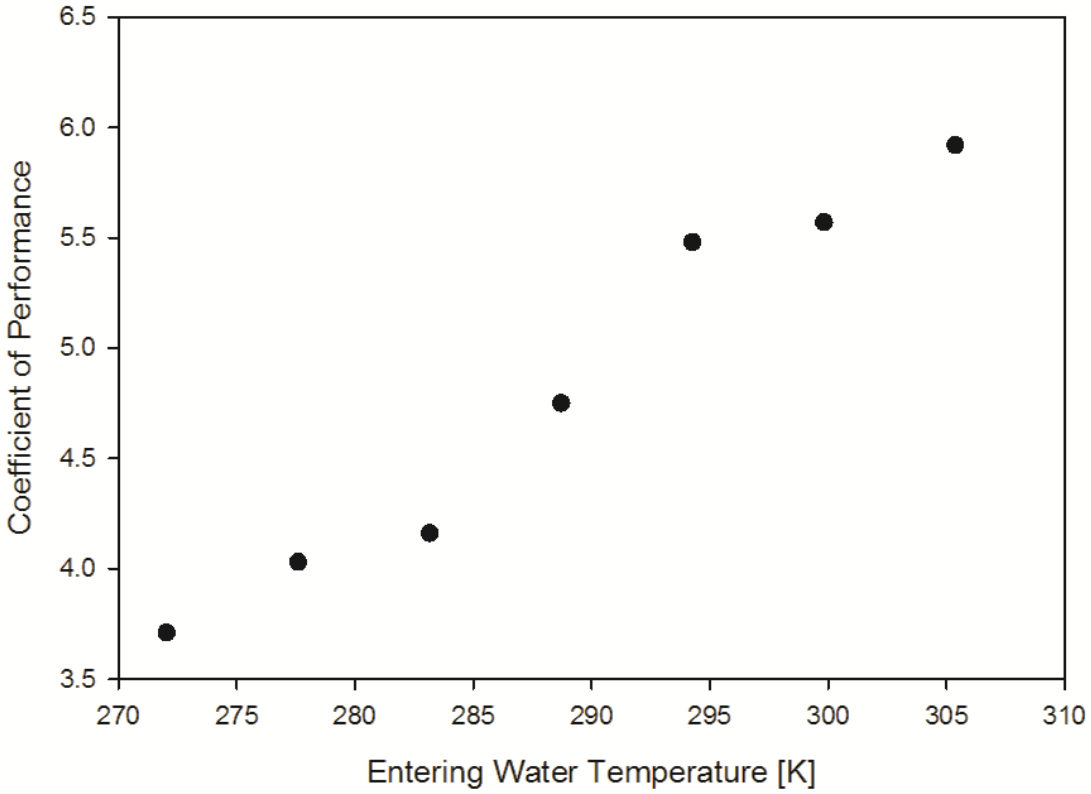

Fig. 2-3: Changes in COP with increasing EWT from the well field during heating mode for a WaterFurnace NV036 that is circulating the well fluid at 11.4 liters per minute and blowing air into a building at 2082 liters per minute (WaterFurnace International, Inc., 2012).

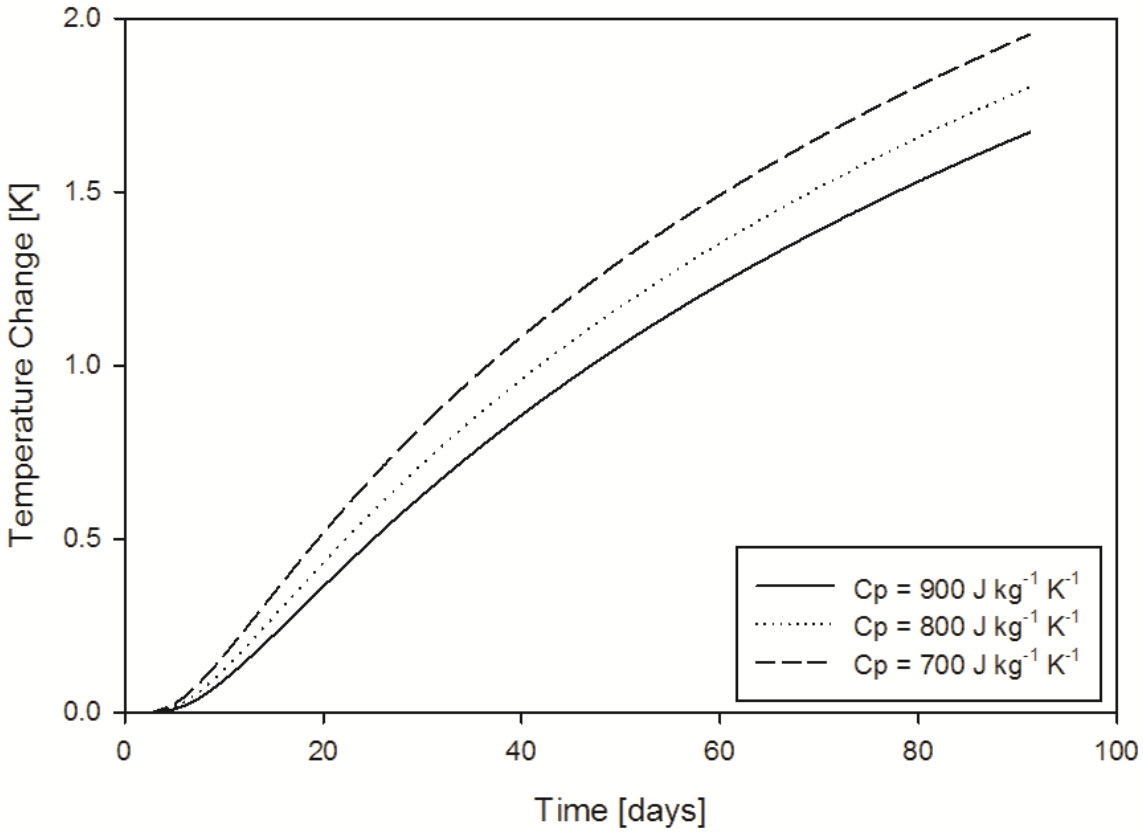

Fig. 2-4: Change in temperature 3 m from the borehole with time for a granite with specific heat ranging from 900 J kg^{-1} K^{-1} to 700 J kg^{-1} K^{-1}. Assumes λ = 3.5 W m^{-1} K^{-1}, ρ = 2600 kg/m^3, borehole depth of 300 m, and a heating load of 17500 W (derived from Eqn [2]).

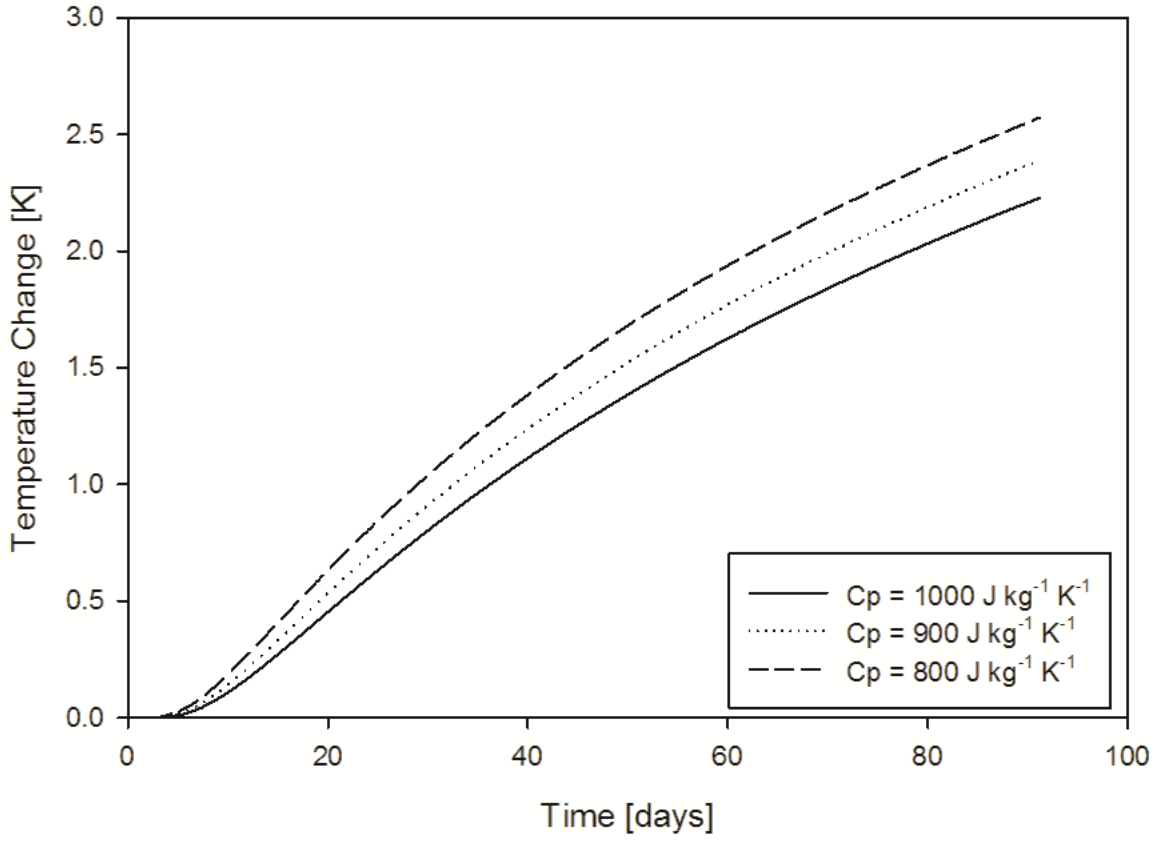

Fig. 2-5: Change in temperature 3 m from the borehole with time for a sandstone with specific heats ranging from 1000 J kg^{-1} K^{-1} to 800 J kg^{-1} K^{-1}. Assumes λ = 2.5 W m^{-1} K^{-1}, ρ = 1800 kg/m^3, borehole depth of 300 m, and a heating load of 17500 W (derived from Eqn [2]).

2.2. Geologic History of Wisconsin

2.2.1. Precambrian

The oldest rocks identified in Wisconsin are Precambrian granite gneisses in central Wisconsin (Dott & Attig, 2004). These granites formed approximately 3,500 million years ago (mya) when intense volcanic activity dominated Wisconsin, Minnesota, Michigan, and Ontario. Approximately 1,000 million years later, additional volcanic activity deformed and metamorphosed these ancient granites into a complex of gneisses forming a small continent. Along the southern edge of this small continent, marine sediments containing fossils were deposited in shallow seas. Around 2,000 mya, iron-rich sediments formed banded iron formations along the shallow seas surrounding the mini continent (Dott & Attig, 2004; LaBerge, 1984). Volcanic activity began again approximately 1,900 mya when a volcanic island chain was formed under a hot spot that migrated northeast across central Wisconsin and erupted volcanic rocks. The island chain continued to move northward, and eventually collided with the margin of the old Superior continent thus forming the Penokean Mountains, while producing large volumes of granitic intrusions around 1890 mya. About 100 million years later, another heating event produced more granitic intrusions and erupted rhyolitic volcanic material across the southern half of Wisconsin (Dott & Attig, 2004; Wenner & Lloyd, 2006). When this volcanic action ceased, red sandstones, black shales and banded iron formations were deposited across the state and into Minnesota. Around 1,650 mya, the volcanic rocks were deformed and metamorphosed and approximately 200 million years later a large

granitic complex, the Wolf River batholith, intruded east-central Wisconsin. About 1,100 mya, the last major geologic occurrence, continental rifting along the Lake Superior rift in northwestern Wisconsin, began with the eruption of large volumes of basaltic lavas. When the eruptions ended, the ruptured crust began to subside. This continued for 200 to 300 million years and red conglomerates, sandstones, and shales were deposited in the rift.

The volcanic rocks that formed during the Precambrian comprise the majority of the basement rock under Wisconsin (Fig. 2-6). These rocks contain high concentrations of heat-producing elements uranium and thorium (8 mg/kg and 50 mg/kg respectively) (Mursky et al. 1988).

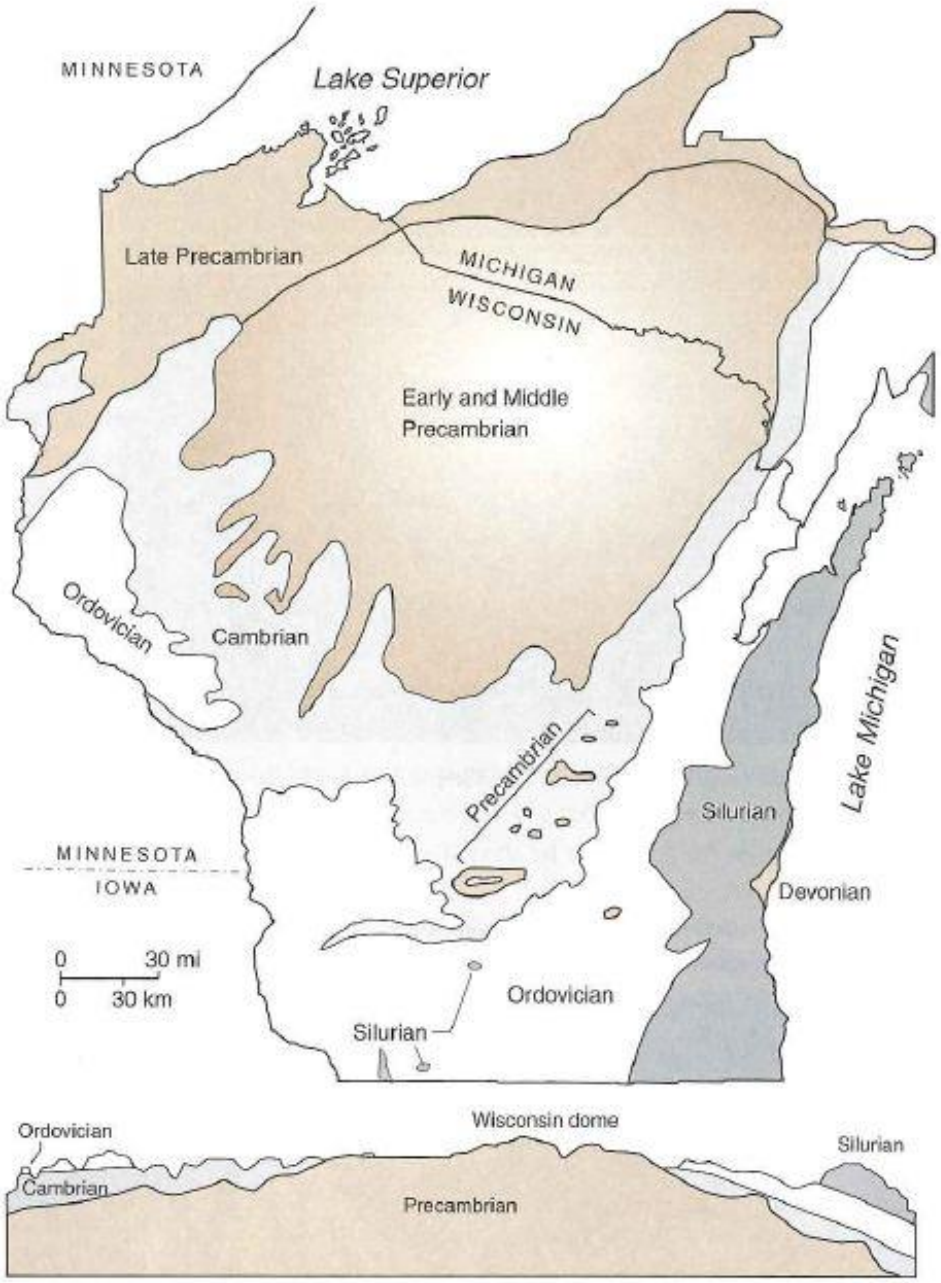

Fig. 2-6: Simplified map of bedrock geology of Wisconsin. The Precambrian rocks in the north form a dome with the Paleozoic strata dipping slightly away from it (Dott & Attig, 2004).

2.2.2. Paleozoic

As subsidence of the Lake Superior rift continued and basins in Michigan to the east and Iowa to the southwest began to subside, the Precambrian crust began to upwarp under Wisconsin creating the Wisconsin Dome (Dott & Attig, 2004). The period of volcanic activity had also ceased, and major sedimentary deposition occurred from 520 to 400 mya as much of Wisconsin was covered in shallow seas. During the Cambrian, most of the land was exposed to erosion from wind and rivers crossing the area, producing very well-rounded sand grains. Subsequently, these eroded sand particles were re-deposited by ocean waves and currents producing Cambrian seas no deeper than 30 m. Characteristic of beaches and tidal environments, these deposits display strata of sand and fine pebbles fining upward and contain ripple marks, burrows, and crawling tracks that were overlain by more sandy sediments produced from migrating underwater dunes. Further ashore, the deposits consisted of fine sands and muds. Through the remainder of the Paleozoic, vast areas were covered by limestone, some containing fossils after the introduction of brachiopods, brozoans, corals, clams and crinoids (Dott & Attig, 2004; LaBerge, 1984). Much of this limestone was altered to dolomite through various diagenetic processes (Dott & Attig, 2004; Smith & Simo, 1997). The sea level continued to rise and fall, eroding and re-depositing sediments while stromatolites formed along the shoreline. One soft shale deposit formed, the Maquoketa Shale, though this deposit is easily eroded and rarely appears in outcrops. These sedimentary rocks form a U-shaped pattern surrounding the northern Precambrian rocks on the west, south and

east (Fig. 2-6). A more detailed bedrock geology map of Wisconsin can be seen in Fig. 2-7. From approximately 400 to 2.5 mya, there is a section missing in the rock record. This unconformity was caused by erosion.

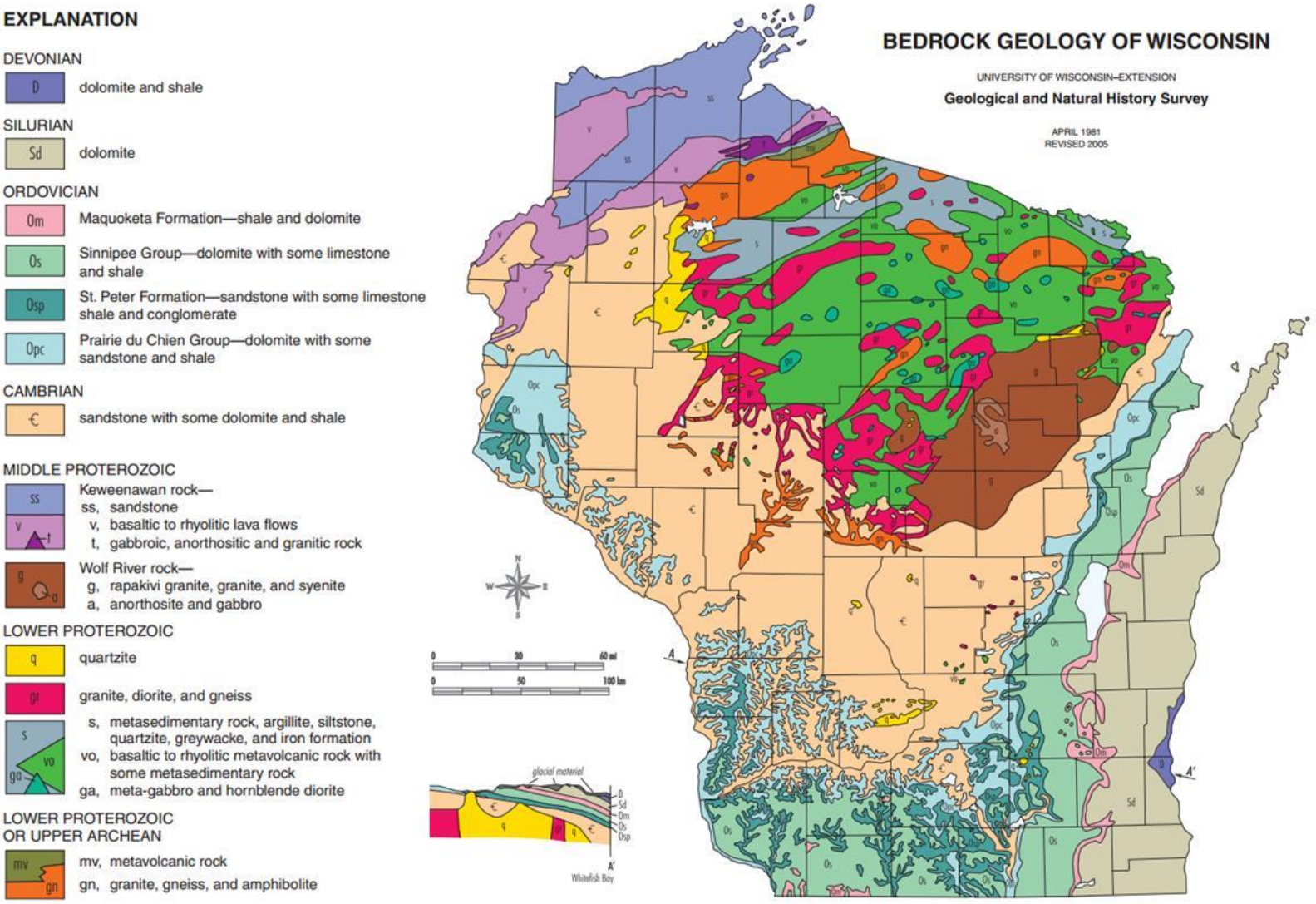

Fig. 2-7: Bedrock geologic map of Wisconsin (WGNHS, 2005).

2.2.3. Quaternary

The next geologic event to impact Wisconsin was the Ice Age. Over the last 2.5 million years, the climate cooled and glacial sheets moved repeatedly across the majority of Wisconsin (Dott & Attig, 2004; Schneider, 1983; LaBerge, 1984). The only area not covered by glaciers was the Driftless Area in Wisconsin to the West and Southwest (Fig. 2-8). Many of the glacial lobes encroached on this area at different times, but the Driftless Area was never surrounded completely at one given time. The glaciers vastly modified the landscape, producing moraines, drumlins, eskers, and outwash plains as the glaciers advanced and retreated, depositing till as they went. During this time, across all of Wisconsin, the ground would have been frozen to depths of tens or hundreds of meters deep (Dott & Attig, 2004). As the glaciers began to melt, the Mississippi and Missouri rivers carried silt-rich meltwater from the ice sheets. When the river flow diminished, these silts and clays were deposited on the river beds. When this material dried, it was then picked up by prevailing westerly winds and blown east across the state of Wisconsin, thus creating a layer of loess.

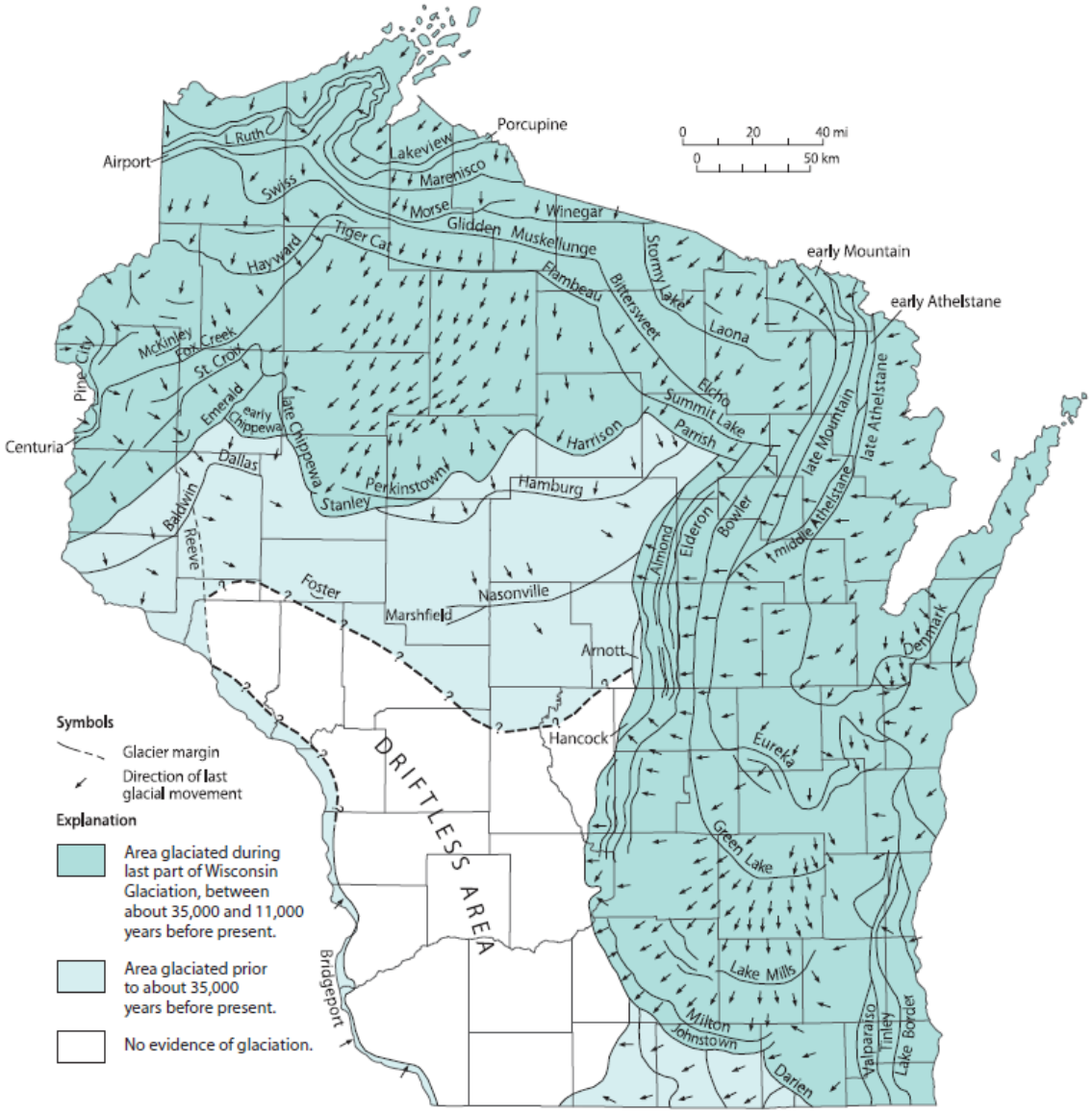

Fig. 2-8: Phases of Wisconsin glaciation (Attig et al., 2011).

2.3. Thermal Gradient in Wisconsin

Limited information exists about the geothermal gradient in Wisconsin. Currently, estimations of the geothermal gradient have been based off of a sparse set of data that covers the southern portion of the state. Worldwide, the average geothermal gradient is between 25 K/km and 30 K/km (Dickson & Fanelli, 2004), while Wisconsin's geothermal gradient has been estimated at or below 20 K/km (Blackwell et al., 2007). This value could be higher due to the high concentrations of heat-producing, radioactive elements such as U, Th, and K (> 4 mg/kg, 17 mg/kg and 3.2 mg/kg respectively) in Wisconsin's granites (Mursky et al., 1988), and due to a lack of data for the state. However, climatic variations also need to be considered. Stacey & Davis (2008) state that climatic variations extending back hundreds to thousands of years can be reflected in the top few hundred meters of continental crust. Thus, due to extensive glaciation, the gradient in Wisconsin has likely also been affected by the long-term exposure to cold surface temperatures.

To further explore Wisconsin's geothermal gradient, five wells were recently drilled across central and northern Wisconsin by the WGNHS to fill in the gaps of missing geothermal gradient data. Three wells, GW1, GW2 and GW3, were drilled in Wausau, WI in Precambrian granite. GW4 and GW5 were drilled in Arlington, WI and Fort McCoy, WI respectively. Both of these wells were comprised of granites overlain by sandstone. Three more wells (GW6, GW7 and GW8) will be drilled in the future.

With data obtained by the WGNHS, a semi-comprehensive map of the geothermal gradient in Wisconsin has been created (Fig. 2-9). Wells vary between 113 m and 592 m in depth, and the thermal gradient varies between 0 and 39 K/km. The average geothermal gradient for Wisconsin appears to range between 16 K/km and 24 K/km, close to the approximation made by Blackwell et al. (2007). However, according to the data summarized in Fig. 2-9, some wells drilled in the sedimentary sequences in central Wisconsin have higher geothermal gradients. This is likely due to the heat-producing granite underlying the sedimentary rocks in these regions. Further exploration of these hypotheses must be completed before a conclusion can be made about Wisconsin's geothermal potential and additional data must be collected to completely analyze Wisconsin's thermal gradient and heat production.

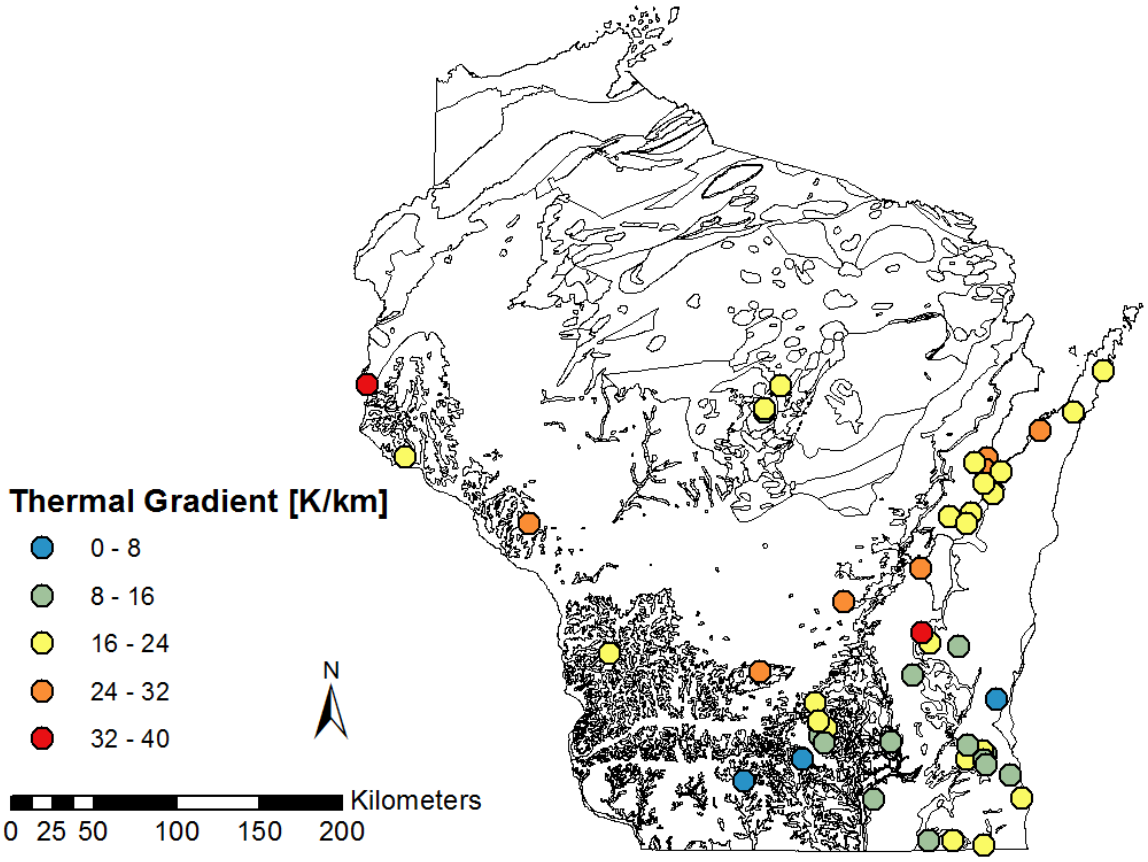

Fig. 2-9: Geothermal gradient map of Wisconsin. Circle color designates the thermal gradient range. The black lines represent a change in geologic formation based on Fig. 2-7.

2.4. Thermophysical Properties

Heat is transferred through four different mechanisms in the earth: radiation, advection/convection, transient diffusion and stead-state conduction; conduction being the dominant mechanism in the Earth's lithosphere (Clauser & Huenges, 1995; Clauser C. , 2009). Radiation is a minor contribution to heat transfer in most materials until they have reached 873 K and is not efficient until after 1473 K. Temperatures this high are not found in the Earth's crust, thus heat transfer due to radiation is typically ignored. However, heat transfer due to advection or convection (i.e., groundwater flow) can affect highly porous or fractured rocks by creating localized areas of comparatively higher or lower temperatures.

Typical geothermal heat pump system designs use the thermal conductivity and specific heat, or thermal diffusivity, of the surrounding soil/ rock to determine the required bore length for the system (ASHRAE 2007, Kavanaugh et al., 1997). These values are also used to solve geothermal problems related to heat extraction and heat storage in the ground and play an important role in the heating and cooling of buildings and some industrial processes (Schärli & Rybach, 2001). For bore length design, thermophysical properties are typically estimated due to the high cost of running a thermal response test (TRT) (approximately $8,000) or thermal property tests, particularly for residential systems (Dickie, 2010). Due to the inability to guarantee the thermal properties of the underlying rock formations, a factor of safety must be applied. However, running a TRT for larger commercial or industrial systems can be valuable. By completing a TRT or measuring the thermal properties

of the rock or soil, the system efficiency can be improved and cost can be reduced. Once the thermal conductivity of the rock or soil is determined, a reduced factor of safety can be used for system design. This will reduce the total system bore and pipe length, thus lowering costs.

2.4.1. Thermal Conductivity

Thermal conductivity is a measure of the amount of heat a material can transmit for a given temperature gradient and is defined by Fourier's law of heat transfer for one dimensional flow:

$$q = -\lambda \left(\frac{dT}{dy}\right) \text{ [W/m}^2\text{]} \quad [6]$$

where q is the heat flux, λ [W $m^{-1}K^{-1}$] is the thermal conductivity, and T [K] is the temperature. The thermal conductivity of a given rock formation depends on many factors such as temperature, pressure, porosity, saturation, and mineralogy. Thus, the thermal conductivity for any given rock can vary by a factor of two or three due to mineral content and other physical factors (Clauser & Huenges, 1995).

Plutonic and volcanic rocks generally have isotropic heat flow that is mostly vertical. This is because their mineralogical makeup is generally consistent across a large area. Sedimentary or metamorphic rocks, on the other hand, are strongly anisotropic due to bedding, laminations, and other small scale factors that preferentially direct heat flow (Clauser & Huenges, 1995). Controlling factors of thermal conductivity for both metamorphic and plutonic rocks are the quartz, feldspar, and mafic mineral content. With increasing quartz content, there is a general increase in thermal conductivity and, conversely, with increasing feldspar

content, there is a general decrease in thermal conductivity. The main controlling factors of thermal conductivity for volcanic and sedimentary rocks are porosity and saturation. This is because the water and air filling the void spaces of these rocks are relatively lower in thermal conductivity, thus decreasing the bulk thermal conductivity of the rock (Table 2-1). Rocks that are less porous will have a higher thermal conductivity.

For most rock types, there is a general decrease in thermal conductivity with increasing temperature (Clauser & Huenges, 1995). The amount of decrease depends on the main mineral phases in the rock and the corresponding thermal expansion of these minerals. Minerals with higher thermal expansions can exhibit thermal cracking due to differential expansion, which can create contact resistances between mineral grains that effectively decrease the bulk thermal conductivity of the rock.

Table 2-1: Thermal conductivity of quartz in comparison to water and air.

Material	λ [W m^{-1} K^{-1}]
Quartz	7.69
Water	0.58
Air	0.025

2.4.2. Specific Heat Capacity and Thermal Diffusivity

The specific heat capacity, C_p, of a body is defined as the energy required to raise the temperature of a unit mass of a material by one degree. When a material experiences a temperature increase, this heat is stored in the material's molecules in the form of higher translational, rotational, and vibrational energies (Waples & Waples, 2004). When the material cools, the stored heat is released.

The thermal diffusivity, D, is a measure of the propagation rate of thermal disturbances through a material and is defined as a ratio of the thermal conductivity to the volumetric specific heat capacity. Thus, the variables can be arranged as:

$$C_p = \frac{\lambda}{\rho D} \quad [\text{J kg}^{-1}\ \text{K}^{-1}] \qquad [7]$$

where ρ [kg/m^3] is the density, and D is in units of m^2/s.

Thermal diffusivity and specific heat vary more strongly with change in temperature than thermal conductivity (Clauser, 2009; Vosteen & Schellschmidt, 2003). While thermal conductivity decreases 4% to 7% over 274.15 K to 373.15 K, thermal diffusivity decreases 18% to 22%. Inversely, the specific heat of rocks increases with increasing temperature. In comparison to temperature effects, pressure effects on thermal diffusivity are negligible (Čermák & Rybach, 1982; Waples & Waples, 2004). The increase in thermal diffusivity with increasing pressure cancels out with the increase in thermal conductivity when referring to Eqn. 7.

There also appears to be a correlation between specific heat capacity and rock mineral density, particularly for low- and medium-density minerals (ρ= 4 g/cm^3) (Waples & Waples, 2004). These rocks display a gradual increase in specific heat

capacity with increasing density. Conversely, with high-density minerals, the specific heat decreases with increasing density; this decrease is particularly noticeable for materials containing precious metals. Thermal diffusivity on the other hand tends to increase with increasing density among rocks of similar composition and structure (Hanley et al., 1987). It was also noted by Clauser (2009) that the specific heat seems to decrease with rock age.

Mineral composition also tends to control the specific heat capacity and thermal diffusivity of rocks. The specific heat capacities of sedimentary, felsic and mafic rocks tend to be similar (between 700 J kg^{-1} K^{-1} and 800 J kg^{-1} K^{-1}); however, they are typically lower than the specific heat capacities of ultramafic rocks, which have very low silica content (Waples & Waples, 2004). The lowest specific heat capacity values generally occur in rocks containing heavy-metals (sulfides, silver halides, tungstates, and some oxides and carbonates), while higher values generally occur in rocks containing hydroxides or contain significant amounts of crystalized water (epsomite, brucite, and gypsum). Thermal diffusivities, on the other hand, vary with quartz, calcite and feldspar contents. Rocks with high quartz contents tend to have higher thermal diffusivities whereas those with high calcite contents yield lower thermal diffusivities (Hanley et al., 1987). Rocks containing high feldspar contents typically have intermediate thermal diffusivity values. Table 2-2 shows typical values used as thermal property estimates.

Table 2-2: Thermal properties of rocks at 298.15 K. Adapted from Kavanaugh et al. (1997).

Rock Type	% [1] Occurrence in Earth's Crust	λ [2] All [W m^{-1} K^{-1}]	λ [3] 80% [W m^{-1} K^{-1}]	C_p [J kg^{-1} K^{-1}]	ρ [kg/m3]	D [m^2/s]
Igneous Rocks						
Granite (10% Quartz)	10.4	1.9 - 5.2	2.2 - 3.3	879.2	2643	9.7E-07 - 1.4E-06
Granite (25% Quartz)			2.6 - 3.6			1.1E-06 - 1.5E-06
Amphibolite	42.8	1.9 - 4.7	2.6 - 3.8		2803 - 3124	
Andesite		1.4 - 4.8	1.6 - 2.4	502.4	2563	1.2E-06 - 1.8E-06
Basalt		2.1 - 2.4		711.8 - 879.2	2883	7.5E-07 - 9.7E-07
Gabbro (Cen. Plains)		1.6 - 2.8		753.6	2963	7.0E-07 - 1.2E-06
Gabbro (Rocky Mtns.)		2.1 - 3.6				9.1E-07 - 1.6E-06
Diorites	11.2	2.1 - 3.3	2.1 - 2.9	921.1	2883	7.5E-07 - 1.1E-06
Granodiorites		2.1 - 3.5		879.2	2723	8.6E-07 - 1.4E-06
Sedimentary Rocks						
Claystone		1.9 - 2.9				
Dolomite		1.6 - 6.2	2.8 - 6.2	879.2	2723 - 2803	1.2E-06 - 2.5E-06
Limestone		1.4 - 4.5	2.4 - 2.8	921.1	2403 - 2803	1.1E-06 - 1.5E-06
Rock Salt		6.4		837.4	2082 - 2162	
Sandstone	1.7	2.1 - 3.5		1004.8	2563 - 2723	7.5E-07 - 1.3E-06
Siltstone		1.4 - 2.4				
Wet Shale (25% Qrtz.)	4.2	1.0 - 4.0	1.7 - 3.1	879.2	2082 - 2643	9.7E-07 - 1.3E-06
Wet Shale (No Qrtz.)			1.0 - 1.6			5.4E-07 - 6.5E-07
Dry Shale (25% Qrtz.)			1.4 - 2.4			7.5E-07 - 1.1E-06
Dry Shale (No Qrtz.)			0.9 - 1.4			4.8E-07 - 5.9E-07
Metamorphic Rocks						
Gneiss	21.4	1.7 - 5.7	2.2 - 3.5	921.1	2562 - 2803	9.7E-07 - 1.3E-06
Marble	0.9	2.1 - 5.5	2.1 - 3.3	921.1	2723	8.6E-07 - 1.3E-06
Quartzite		5.2 - 6.9		837.4	2563	2.4E-06 - 5.4E-06
Schist	5.1	2.1 - 4.5	2.4 - 3.8		2723 - 3204	
Slate		1.6 - 2.6		921.1	2723 - 2803	6.5E-07 - 9.7E-07

[1] Percentage of sedimentary rocks is higher near the surface

[2] "All" represents the conductivity range of all samples tested

[3] "80%" represents the mid-range for samples of rock

2.4.3. Radiogenic Heat

When radioactive decay occurs, part of the decaying mass is converted into energy. Most of the energy is in the form of alpha or beta particles or electromagnetic radiation (Van Schmus, 1995; Clauser, 2009; Mursky et al., 1988). A minute portion of this energy is lost to the atmosphere, but the rest is absorbed by the rock mass and turned into heat through particle vibration. In general, the mean heat generation per unit mass H of the earth can be given as:

$$H = \frac{Q}{M} \text{ [W/kg]} \quad [8]$$

where Q is the is the total heat flow and M is the mass of the earth (Turcotte & Schubert, 1982). The heat production in an individual rock can be approximated as:

$$H_0 = \rho(C_0^U H_U + C_0^{Th} H_{Th} + C_0^K H_K) \quad [9]$$

where C_0 is the concentration of the element.

About 80% of the heat produced in the earth comes from the decay of radioactive isotopes, and the remaining 20% of the heat production comes from the cooling of the Earth (Turcotte & Schubert, 1982). The radioactive heating of the mantle crust comes from the decay of ^{235}U, ^{238}U, ^{232}Th, and ^{40}K. Since the radioactive decay of the isotopes yields stable isotopes, heat production due to radioactive decay decreases with time. Due to their shorter half-lives, ^{235}U and ^{40}K contribute less to radioactive heat production than ^{238}U and ^{232}Th. These radioactive isotopes can be incorporated into a rock via six mechanisms: (1) mineral formation (e.g., Thorite, Uraninite, etc), (2) deposition in the structure of the rock minerals by structural defects in the crystals, (3) cation exchange positions, (4) absorption on the

surfaces of the crystals, (5) dissolution in fluid inclusions within the rock minerals and (6) dissolution in intergranular fluids (Neuerburg, 1955; Mursky et al.,1988). Most uranium and thorium isotopes are of igneous origin; however, determining the mechanism associated with the incorporation of these isotopes proves difficult. Uranium content is typically not homogenous across a large body of rock. This heterogeneity is typically correlated with the abundance of accessory minerals such as uraninite, thorite, monazite, zircon, and allanite. Other minerals typically associated with these radioactive elements are listed in Table 2-3.

Table 2-3: Typical minerals bearing K, U, and Th (Van Schmus, 1995).

		Abundances[1]		
Mineral	**Nominal Composition**	**K**	**U**	**Th**
Adularia	$KAlSi_3O_8$	14.0		
Allanite	$(Ca,Ce,Y,Th)_2(Al,Fe,Mg)_3Si_3O_{12}(OH)$		*	***
Alunite	$KAl_3(SO_4)_2(OH)_6$	9.4	-	-
Apatite	$Ca_5(PO_4)_3(F,Cl,OH)$	-	*	*
Apophyllite	$KCa_4(Si_8O_{20})(OH,F)*8H_2O$	4.1	-	-
Autunite	$Ca(UO_2)_2(PO_4)_2*10\text{-}12H_2O$	-	48 - 50	-
Baddeleyite	ZrO_2	-	**	**
Biotite	$K(Mg,Fe)_3(AlSi_3O_{10})(OH)_2$	8-9	-	-
Carnallite	$KMgCl*6H_2O$	14.1	-	-
Carnotite	$K_2(UO_2)_2(VO_4)_2*3H_2O$	7.2	53	-
Glauconite	$K(Fe,Mg,Al)_2(Si_4O_{10})(OH)_2$	4.6 - 6.2	-	-
Hornblend	$NaCa_2(Mg,Fe,Al)_5(Si,Al)_8O_{22}(OH)_2$	***	-	-
Jarosite	$KFe_3(SO_4)_2(OH)_6$	7.8	-	-
Lepidolite	$KLi_2Al(Si_4O_{10})(OH)_2$	7.1 - 8.3	-	-
Leucite	$KAlSi_2O_6$	17.9	-	-
Microcline	$KAlSi_3O_8$	14.0	-	-
Monazite	$(Ce,La,Y,Th)PO_4$	-	**	2 - 20
Muscovite	$K(Al)_2(AlSi_3O_{10})(OH)_2$	9.8	-	-
Nepheline	$(Na,K)AlSiO_4$	3 - 10	-	-
Orthoclase	$KAlSi_3O_8$	14.0	-	-
Phlogopite	$KMg_3(AlSi_3O_{10})(OH)_2$	9.4	-	-
Pitchblend	Massive UO_2	-	88	-
Polyhalite	$K_2Ca_2Mg(SO_4)_4*2H_2O$	13.0	-	-
Sanidine	$KAlSi_3O_8$	14.0	-	-
Spene (Titanite	$CaTiSiO_5$	-	*	*
Sylvite	KCl	52.4	-	-
Thoranite	ThO_2	-	-	88
Thorite	$ThSiO_4$	-	***	72
Torbernite	$Cu(UO_2)_2(PO_4)_2*8\text{-}12H_2O$	-	32 - 36	-
Tyuyamunite	$Ca(UO_2)_2(VO_4)_2*5\text{-}8.5H_2O$	-	45 - 48	-
Uraninite	UO_2	-	88	-
Xenotime	YPO_4	-	***	**
Zircon	$ZrSiO_4$	-	**	**

[1]Percents except as noted: ***=0.5-3%; **=0.1-0.5%; *=0.001-0.1%

3. METHODS AND MATERIALS

3.1. Methods

3.1.1. Guarded-comparative-longitudinal heat flow apparatus

For the determination of rock thermal conductivity, a guarded-comparative-longitudinal heat flow apparatus was constructed following ASTM E 1225 specifications (Fig. 3-1a), but omitting the heater guard. The heater section and heat sink were constructed from Aluminum 6061. Aluminum 6061 was selected because it is easy to machine, is fairly inexpensive, and transfers heat well. The central column composing the heater section, reference materials, specimen, and stainless steel plug will be referred to as the testing column. The aluminum plug was inserted in the space below the bottom reference material to minimize axial heat flow from the bottom of the column (Fig. 3-1a).

Perlite was selected as the insulating material due to its ease of use and low thermal conductivity (≈ 0.031 W m^{-1} K^{-1}). An 11.43-cm-diameter PVC pipe (0.19 W m^{-1} K^{-1}) was attached to the heat sink and used to contain the perlite insulation around the testing column. The insulation, lightly packed in five 100-cm^3 lifts, was approximately 4.45 cm thick and encompassed the entire testing column. Approximately 2.5 cm of self-adhesive foil and foam duct insulation was wrapped around the outside of the PVC pipe and a PVC cap for added protection from the elements.

ASTM E 1225 recommends the use of a reference material with a thermal conductivity on the same order of magnitude as the specimen being tested. Based

on an estimated range of thermal conductivity of 1 W m^{-1} K^{-1} to 8 W m^{-1} K^{-1} for the rock specimens, the reference material selected for this test setup was an Institute for Reference Materials and Measurements (IRMM) certified glass-ceramic (BCR-724). The IRMM certificate of analysis for BCR-724 states that the material has a thermal conductivity of:

$$\lambda = 2.332 + \frac{515.5}{T} \text{ [W m}^{-1} \text{ K}^{-1}\text{]} \quad [10]$$

Over the testing range of 273.15 K to 333.15 K, this yields a thermal conductivity of approximately 3.9 W m^{-1} K^{-1} to 4.0 W m^{-1} K^{-1}. Tye and Riko (1996) suggest the use of Pyroceram 9606 or Pyrex 7740 for specimens with a low thermal conductivity (< 5 W m^{-1} K^{-1}). The BCR (Bureau Communitaire de Reference) Pyrex glass products were very similar to Pyrex 7740 and were the only low thermal conductivity reference materials sold by national standards laboratories at the time of this research.

The heat source was created using a cartridge heater from High-Temp Industries. The cartridge heater was placed in the central aluminum heater section as shown in Fig. 3-1a and 3-1b and was controlled using an Opto 22 Solid State Relay (model 120D3) switch that was connected to a Campbell Scientific datalogger. The Campbell Scientific Loggernet software program signaled the heaters to turn on and off based on the desired testing temperature. The heater was also connected to a Superior Electric Co. Powerstat 136 Variable Autotransformer (120 V, ~20 Amps) to control the current entering the heater. Unlike conventional transformers, an autotransformer has only one winding, which allows a portion of the electrical energy

absorbed to be transformed and the remainder to flow conductively through its windings (Pansini, 1999). Thus, the autotransformer was used to reduce the current entering the heating element above the testing column, in turn reducing the range of temperatures the testing column experienced as the relay switch turned on or off.

A heat sink was created using a solid aluminum cylinder placed in a water bath that is cooled by a copper coil connected to a larger (~57 L) water bath in a freezer. A pump in the larger water bath circulated about 273-K water through plastic tubing to the copper coil in the smaller water bath until the water exited into another plastic tube that runs back into the freezer. The smaller water bath was encased in an extruded polystyrene (XPS) pink insulation to keep the bath cold and to reduce condensation. The XPS had an R value of 7.5 and was 3.81 cm thick.

The temperature sensors were Omega Type T thermocouples, which have a rated accuracy of the greater of 274.15 K or 0.75% above 273.15 K. A thermocouple is a set of two dissimilar metal wires joined together at the end to form a junction (Dunnicliff, 1988). At any temperature above 0 K, the wires produce a small voltage that is proportional to the temperature at the junction. These wires are connected to a datalogger calibrated for the voltage/temperature proportionality; thus, temperature data can be collected. Two thermocouples were placed in each reference material and an additional two were placed in the specimen tested. Before the thermocouples are placed in the materials, each thermocouple hole was filled with Artic Alumina thermal grease using a hypodermic needle to ensure a perfect contact with the materials tested. To maintain adequate contact between the reference materials and

the specimens sandwiched between them, small sheets of aluminum foil were cut to a diameter of 2.54 cm and placed between the material interfaces. The testing column and the thermocouples were held together using electrical tape. Additionally, a vertical pressure of 1 MPa was applied using a load frame and load cell to maintain contact between the specimen and the reference materials as well as to simulate *in situ* confinement. Data was collected using a Campbell Scientific datalogger. Refer to Fig. 3-1 through Fig. 3-7 for photos of the laboratory set up; note that none of the images include the added duct insulation around the PVC pipe. This test was run for unsaturated rock specimens.

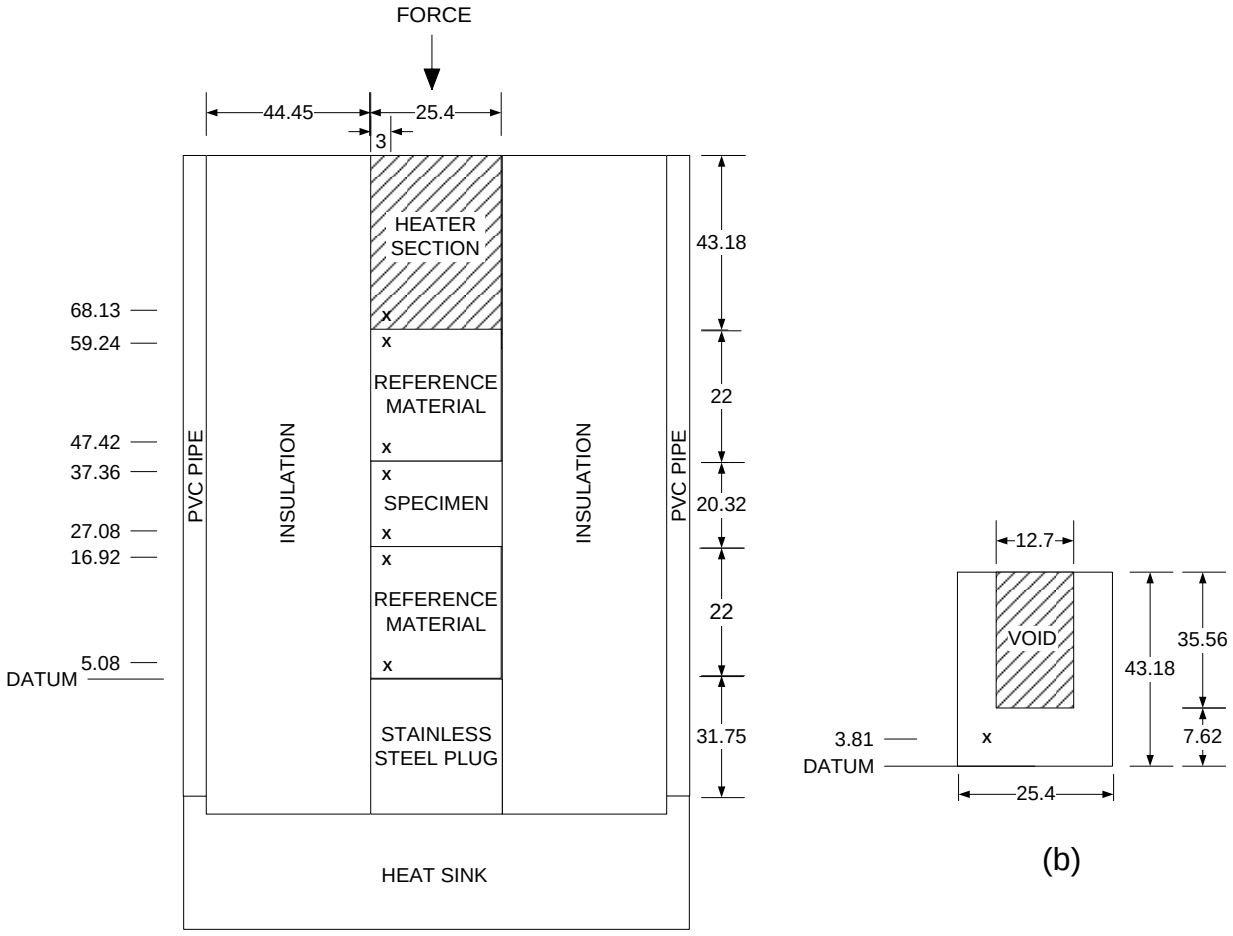

Fig. 3-1: Diagram of the guarded-comparative-longitudinal heat flow apparatus; X's denote thermocouple locations, all dimensions in mm. (a) cross sectional view of apparatus; (b) cross sectional view of the heater section, central hole denotes where the heater is inserted.

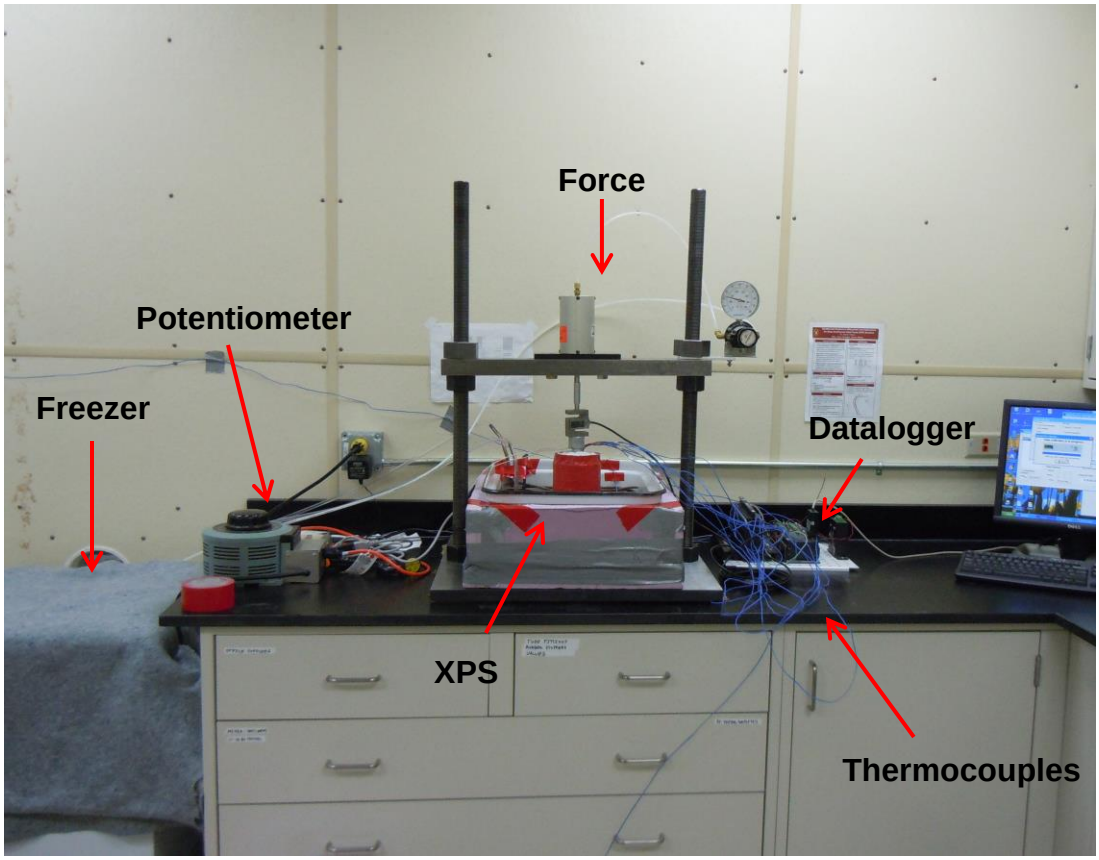

Fig. 3-2: Guarded-comparative-longitudinal heat flow set up in the laboratory.

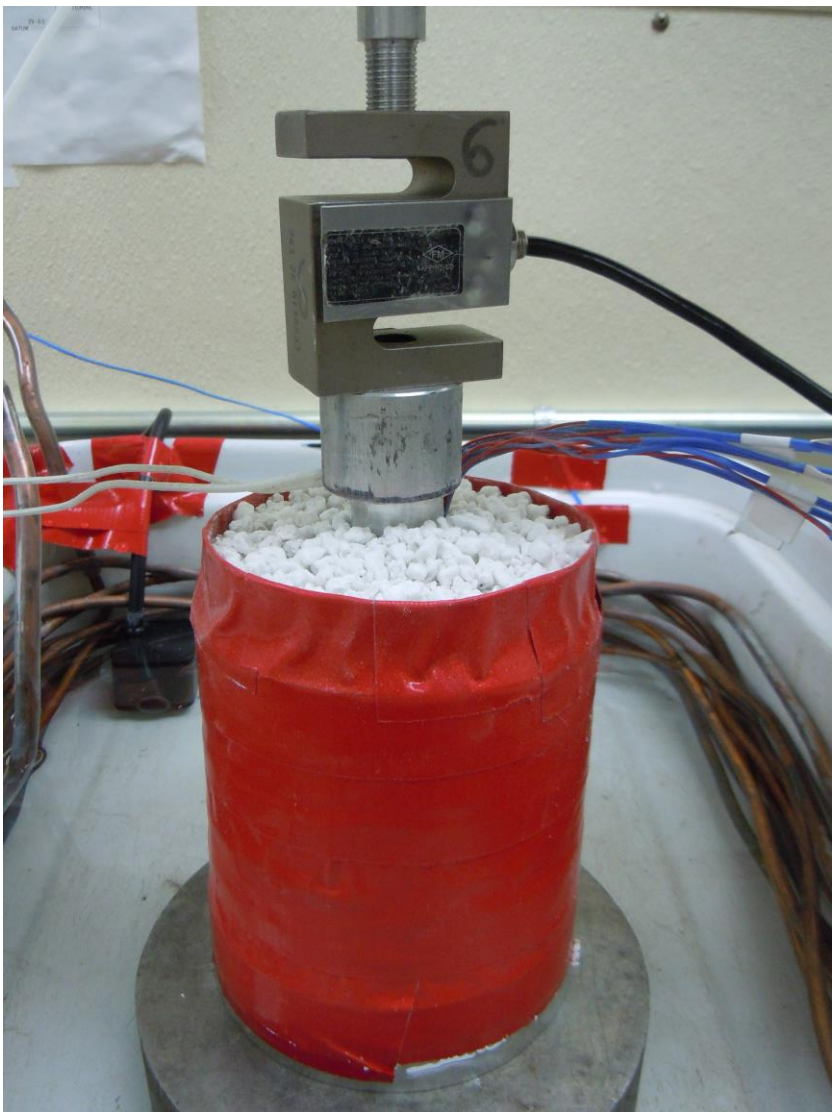

Fig. 3-3: Close-up of testing cell with applied load.

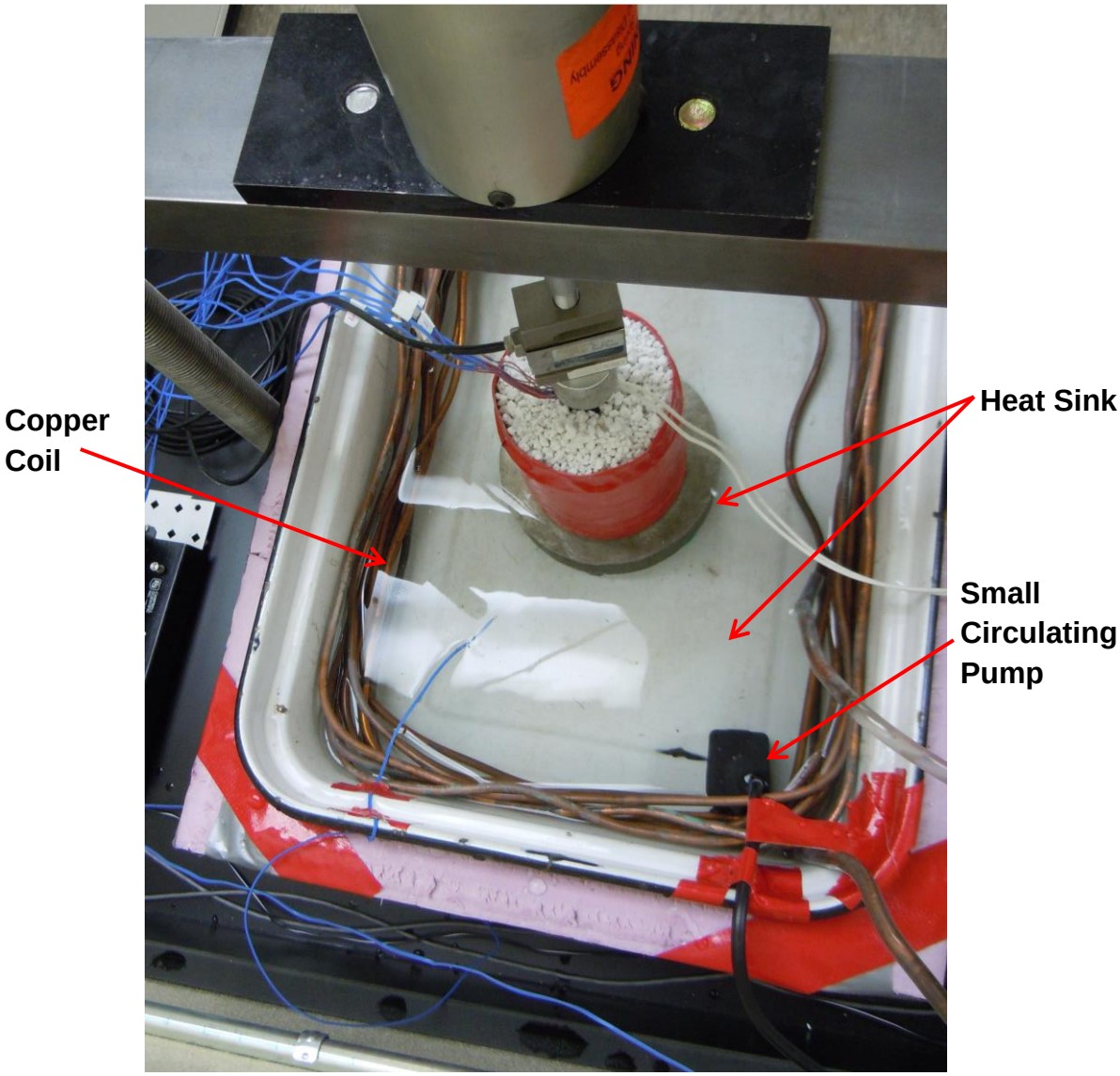

Fig. 3-4: Close-up on the testing column and the small water bath with the copper coil used for cooling the system and the small pump used to circulate water in the bath.

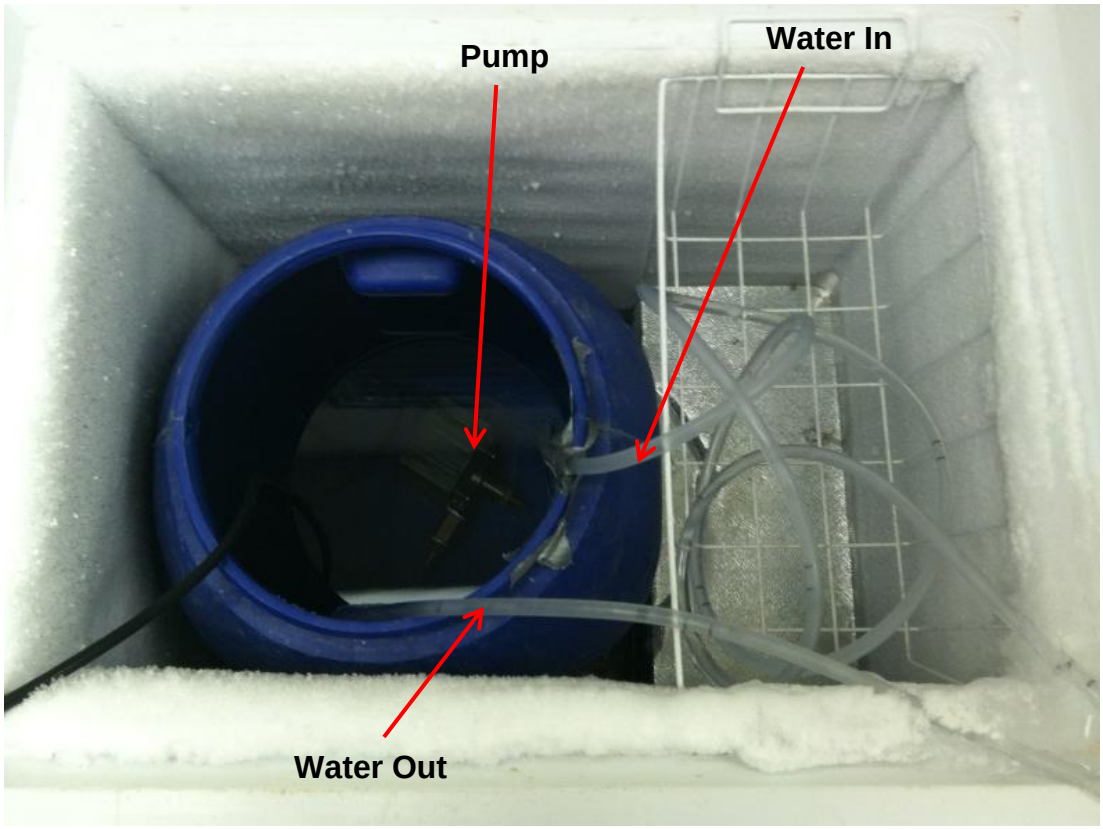

Fig. 3-5: Freezer with large (57 L) water bath and pumping system.

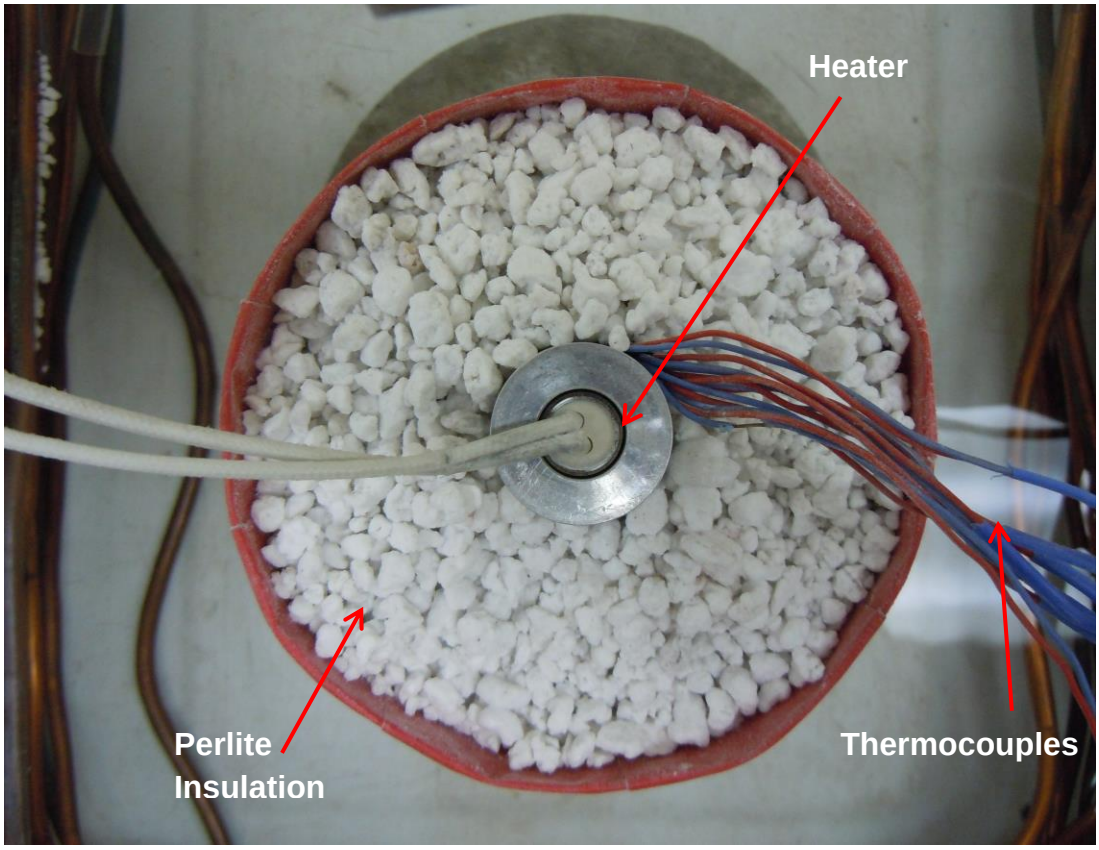

Fig. 3-6: Top view of the testing column with the load removed from the top. The location of the heater placed in the central heater section is visible. The thermocouples exit along the side of the testing column.

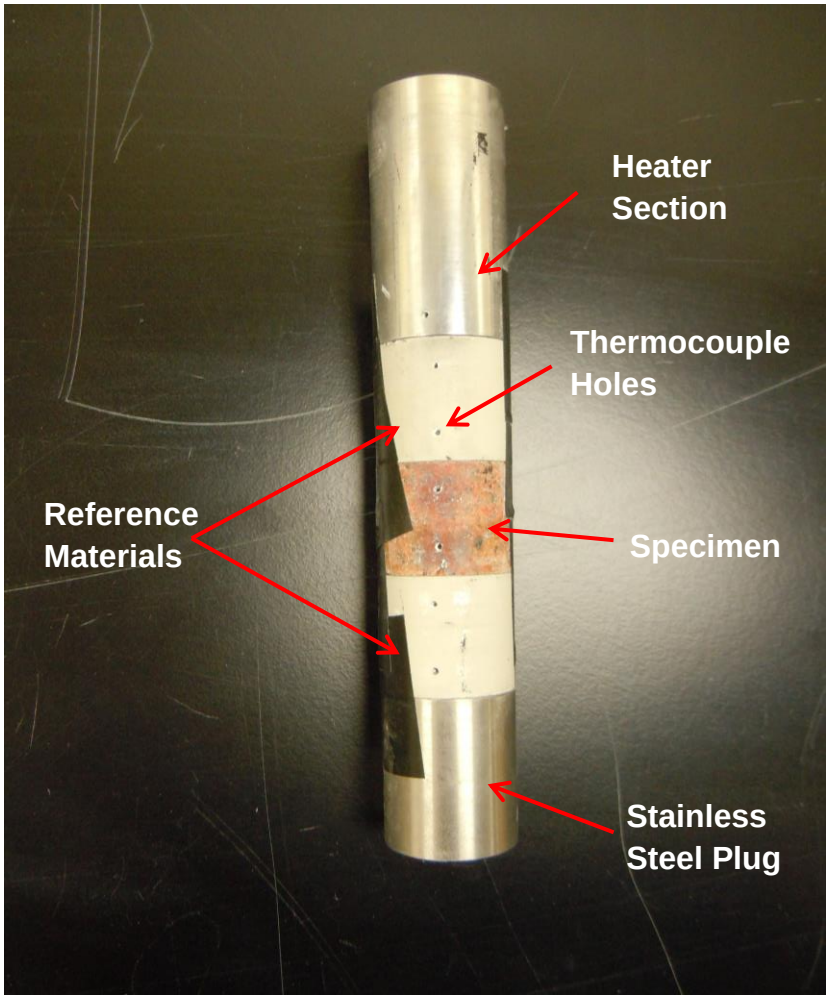

Fig. 3-7: View of central testing column and drilled thermocouple holes.

3.1.1.1. Instrumentation Development

ASTM E1225 describes the standard test method for determining the thermal conductivity of opaque solids and is effective for materials with conductivities between $0.2 < \lambda < 200$ W m^{-1} K^{-1} over the range of 90 to 1300 K (ASTM International, 2009). This method differs from other conductivity methods (ASTM C177, ASTM C518, and ASTM C1113) in that it requires the use of a heater guard. The purpose of the heater guard is to ensure the temperature gradient on the outside of the testing column is equal to that within the testing column to reduce radial heat flow. However, due to difficulties in matching the two gradients, the heater guard was omitted. Research has been conducted on the necessity of the heater guard, and some have stated that due to the additional cost of implementing the heater guard and the added complication associated with it, the heater guard can be omitted (Niencheski & Müller, 2008; Slifka, 2000). Niencheski & Müller (2008) showed that the modified apparatus without the heater guard was suitable for the assessment of specimens with thermal conductivities of 10 W m^{-1} K^{-1} and above. The rock specimens being tested are expected to be between 1 W m^{-1} K^{-1} and 8 W m^{-1} K^{-1} and thus do not fall in the range specificed by Niencheski & Müller (2008). However, Slifka (2000) states that the heater guard is not necessary for smaller scale testing because the heat loss on the small scale is negligible. Temperature measurememnts taken over shorter distances ensures negligible heat loss. With increased insulation volume surrounding the apparatus, the heat flow apparatus yielded an experimental error up to ± 0.70 W m^{-1} K^{-1}. The experimental error

analysis was completed using simplified statistics for small numbers of observations. Each specimen was tested three times to ensure repeatability as well as to obtain a median and corresponding confidence interval for error (Dean & Dixon, 1951). Values reported represent the greater of the experimental error or calculated uncertainty error.

3.1.1.2. Kline McClintock Uncertainty Analysis

Uncertainty analysis for the guarded-comparative-longitudinal heat flow apparatus was completed using the Kline McClintock second power relation (Figliola & Beasley, 2000). This method is derived from a linear approximation of the Taylor series expansion for multivariable functions. Thus, for a linear equation Z = X × Y, the uncertainty can be determined using the following:

$$U_Z = \sqrt{\left(\left(\frac{dZ}{dX}\right)U_X\right)^2 + \left(\left(\frac{dZ}{dY}\right)U_Y\right)^2} \quad [11]$$

where U_Z is the uncertainty in the variable Z, U_X is the uncertainty in the measurement X, and U_Y is the uncertainty in the measurement Y.

In the measurement of thermal conductivity, the total error propagates from errors associated with the measurement of length, area, heat transfer and temperature. Thus, all variables need to be considered when completing the error analysis. The equation used to determine the error in the thermal conductivity measurements (U_λ) can be represented by the equation below:

$$U_\lambda = \pm\sqrt{\left[\left(\frac{l}{A\Delta T}\right)(U_q)\right]^2 + \left[\left(\frac{q}{A\Delta T}\right)(U_l)\right]^2 + \left[\left(\frac{ql}{A^2\Delta T}\right)(U_a)\right]^2 + \left[\left(\frac{ql}{A\Delta T^2}\right)(U_{\Delta T})\right]^2} \quad [12]$$

where l is the specimen length [m], A is the cross sectional area of the specimen [m^2], ΔT is the change in temperature [K], q is the heat flow [W], U_l is the uncertainty in the length [m], U_a is the uncertainty in the cross sectional area [m^2], $U_{\Delta T}$ is the uncertainty in the change in temperature [K], and U_q is the uncertainty of the heat flow [W]. U_l was determined using the following adaptation of the Taylor series expansion for multivariable functions:

$$U_l = \pm\sqrt{((l)(U_c))^2} \quad [13]$$

where U_c is the uncertainty in the calipers used to measure the length [m]. U_a was found in a similar manner, but using the following equation:

$$U_a = \pm\sqrt{((0.5\pi d)(U_c))^2} \quad [14]$$

where d is the diameter of the specimen [m]. The uncertainty in the heat flow U_q was found using:

$$U_q = \pm\,\lambda_{ins}\,A_s\,\frac{T_{spec} - T_{room}}{t_{ins}} \quad [15]$$

where λ_{ins} is the thermal conductivity of the insulation [W m^{-1} K^{-1}], A_s is the surface area exposed to the insulation [m^2], T_{spec} is the specimen temperature [K], T_{room} is the room temperature [K], and t_{ins} is the thickness of the insulation [m]. The uncertainty in the temperature change of the thermocouples was found with the following equation:

$$U_{\Delta T} = \pm\sqrt{6}U_T \quad [16]$$

where U_T is the uncertainty in the thermocouples. This statement is valid because U_T was the same for all 6 thermocouples used in the experimental setup.

The uncertainty analysis yielded error values between 0.04 W m^{-1} K^{-1} and 0.05 W m^{-1} K^{-1}. This corresponds to a relative error of < 3% for the experimental setup, which is much less than the observed experimental error and is indicative of sufficient system design.

3.1.2. Calorimeter

To determine specific heat, calorimetry tests were conducted on each specimen using a “coffee-cup” calorimeter. The insulating cup used to hold the water was surrounded with perlite in a 30 cm x 38 cm insulating box made from 3.81-cm-thick XPS pink insulation (R value of 7.5). An Omega Type T thermocouple was inserted into the water in the insulating calorimeter cup to monitor temperature.

Tests were run with an initial specimen temperature of 333.15 K to match the temperature conditions of the thermal conductivity tests. The procedure for the calorimetry testing is based conceptually on Science First (2003):

1. Find the mass of the water in the calorimeter cup (m_{H2O}) (just enough to cover specimen while in cup) and of the specimen (m_s).
2. Place specimen and tongs in oven set at 333.15 K for 2 h to ensure the rock specimen reaches equilibrium.
3. Place insulating cup filled with water in insulating box filled with perlite (Fig. 3-8). Launch Campbell Scientific Loggernet program and watch thermocouple measurements to ensure temperature of water in the insulating cup is at

equilibrium with room temperature, T_{min} (program should be set to take measurements every 10 s).

4. After T_{min} is achieved, note the time and set T_{min} at t_0.
5. Record the oven temperature and then remove the rock specimen from the oven using the warm tongs. After removing the insulating cup lid, quickly place the specimen into the water and replace lid. Note the time at which the specimen was placed in the water.
6. Close lid on insulating box and cover with insulating blanket. Agitate the box throughout the duration of the test to ensure thorough mixing of the water.
7. Set the Campbell Scientific Loggernet program to record temperature at least every 10 s for 5 min to 10 min at which point the temperature of the water in the insulating cup begins to decrease. Total duration of recording temperatures is typically between 15 to 20 min.
8. When the temperature of the water begins to decrease, the temperature of the specimen and water have reached equilibrium, T_{max}, and the test is terminated.

After T_{max} is determined (highest temperature that the aluminum calorimeter experiences during the test), the specific heat of the specimen is calculated as:

$$C_{ps} = \frac{m_{cal} * C_{pcal}(T_{max} - T_{min})}{m_s(T_s - T_{max})} \text{ [J kg}^{-1}\text{ K}^{-1}\text{]} \quad [17]$$

where C_{ps} is the specific heat of the specimen, C_{pcal} is the specific heat of the aluminum cup and T_s is the initial temperature of the specimen. This test was run for unsaturated rock specimens.

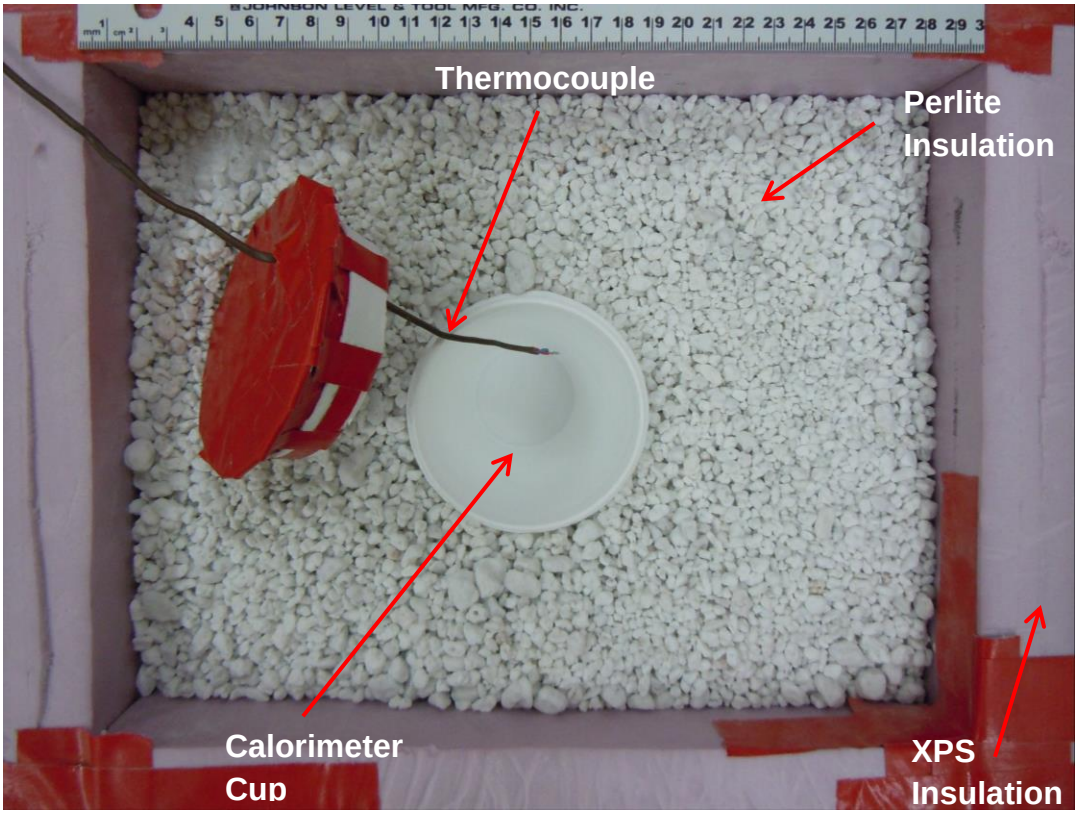

Fig. 3-8: Calorimeter setup using perlite and XPS insulation as insulating material.

3.1.2.1. Instrumentation Development

The original calorimeter used to determine specific heat was a dry aneroid calorimeter from Fisher Scientific. However, the insulating material surrounding the calorimeter cup was not sufficient to eliminate effects from the surrounding elements. As a remedy, the dry aneroid calorimeter was insulated further, but the desired results could not be obtained. A new design based on the “coffee-cup” calorimeter was then constructed using a Styrofoam insulating calorimeter cup filled with water in an XPS insulating box filled with perlite. The box was agitated to maintain thermal homogeneity in the cup while the test was running. To reduce error, the volume of water used for testing was minimized to between 45 g and 55 g, just covering the specimen. With the modified experimental setup, the coffee-cup calorimeter yielded a maximum experimental error of ± 69 J kg^{-1} K^{-1}. Each specimen was tested at least three times to ensure repeatability. Values reported represent the 95% confidence interval of the experimental values (Dean & Dixon, 1951).

3.1.2.2. Kline McClintock Uncertainty Analysis

Like the method used for the guarded-comparative-longitudinal heat flow apparatus, the uncertainty analysis for the calorimeter was completed using the Kline McClintock second power relation (Figliola & Beasley, 2000). In the measurement of specific heat, the total error propagates from errors associated with the measurement of mass and temperature. Thus, both variables must be considered when completing the error analysis. The equation used to determine the error in the thermal conductivity measurements (U_{cps}) can be represented as:

$$U_{cps} = C_{pc*}\sqrt{\left[\left(\frac{\Delta Tw}{ms*\Delta Ts}\right)(U_{mw})\right]^2+\left[\left(\frac{mw}{ms*\Delta Ts}\right)(U_{\Delta Tw})\right]^2+\left[\left(\frac{\Delta Tw*mw}{ms^2*\Delta Ts}\right)(U_{ms})\right]^2+\left[\left(\frac{\Delta Tw*mw}{ms*\Delta Ts^2}\right)(U_{\Delta Ts})\right]^2} \quad [18]$$

where C_{pc} is the specific heat of the calorimeter [J kg^{-1} K^{-1}], m_s is the mass of the specimen [kg], ΔT_w is the change in temperature of the water [K], ΔT_s is the change in temperature of the specimen [K], U_{mw} is the uncertainty in the mass of the water [kg], U_{ms} is the uncertainty in the mass of the specimen [kg], $U_{\Delta Tw}$ is the uncertainty in the temperature of the water [K], $U_{\Delta Ts}$ is the uncertainty in the temperature of the specimen [K]. U_{mw} and U_{ms} were determined using the following adaptations of the Taylor series expansion for multivariable functions:

$$U_{mw} = \pm\sqrt{((mw)(U_s))^2} \quad [19]$$

$$U_{ms} = \pm\sqrt{((ms)(U_s))^2} \quad [20]$$

where U_s is the uncertainty in the scale used to measure the mass [kg]. $U_{\Delta Tw}$ and $U_{\Delta Ts}$ were found using:

$$U_{\Delta Tw} = \pm\sqrt{3}U_T \quad [21]$$

$$U_{\Delta Ts} = \pm\sqrt{3}U_T \quad [22]$$

where U_T is the uncertainty in the thermocouples. This statement is valid because U_T was the same for all three thermocouples measurements used in the experimental set up.

The uncertainty analysis yielded error values in C_p between 250 J kg^{-1} K^{-1} and 145 J kg^{-1} K^{-1}, suggesting possible insufficiencies in system design. However, since the maximum experimental error was ± 69 J kg^{-1} K^{-1} for a series of three or more tests per specimen, the uncertainty analysis results are insignificant. Since the

calculated uncertainty analysis error greatly exceeded the observed experimental error, the values reported only represent the experimental error.

3.1.3. Density and Porosity

Specimen density (ρ) was determined by first measuring the length and diameter of the specimens with a calipers to obtain their volume (V_{total}) and then determining each specimen's mass [m] using a scale. Density was calculated using:

$$\rho = \frac{m}{V_{total}} \text{ [kg/m}^3\text{]} \quad [23]$$

Specimen porosity (n) was determined using a Helium porosimeter in the Weeks Hall Geophysics Laboratory at the University of Wisconsin-Madison using the following procedure:

1. Using oven dry specimens, measure specimen length and diameter.
2. Place billets into sample cell, and record billet volume (B).
3. Bleed small amount to helium gas through chamber line.
4. Close the sample cell and keep helium line open.
5. Apply vacuum to the sample cell until the multimeter shows a suitably low pressure, P_{zero} (approximately 2.0 – 2.7 kPa).
6. Close the chamber line/sample cell valve and turn off vacuum pump.
7. Introduce helium gas to the reference chamber until a pressure of 550 – 620 kPa is reached.
8. Close the helium gas valve and read the pressure on multimeter. Record value as $P_{load\text{-}in}$.

9. Open the chamber line/sample cell valve. Record new value on multimeter as $P_{final\text{-}in}$.
10. Repeat procedure after removing the billets to measure the load pressure ($P_{load\text{-}out}$) and final pressure ($P_{final\text{-}out}$) in empty cell. Calculate the reference chamber volume using:

$$R = \frac{B}{\frac{P_{load-out}}{P_{final-out}} + \frac{P_{load-in}}{P_{final-in}}} \text{ [cm}^3\text{]} \quad [24]$$

11. Place rock specimen into the sample cell and load billets in empty cell space (if any), repeat steps 3 through 8 recording load pressure with specimen ($P_{load\text{-}spec}$) and final pressure with specimen ($P_{final\text{-}spec}$).
12. Calculate porosity (n) of each specimen using the following:

$$V_{solid} = B + \frac{P_{load-in}}{P_{final-in}} \times R - \frac{P_{load-spec}}{P_{final-spec}} \times R \text{ [cm}^3\text{]} \quad [25]$$

$$n = \frac{V_{total} - V_{solids}}{V_{total}} \times 100 \text{ [\%]} \quad [26]$$

3.1.4. X-Ray Diffraction

X-ray diffraction testing was conducted in the S.W. Bailey X-Ray Diffraction Laboratory at the University of Wisconsin-Madison using a D/max Rapid II XRD machine based on the RIGAKU Rapid II Operating Instructions (S.W. Bailey X-ray Diffraction Laboratory, Dept of Geoscience UW-Madison, 2011). The diffractor was run at 50 kV and 50 mA and used Mo-Kα radiation. A 0.1-mm collimator was used for the 5-min tests where omega was 0 degrees and the phi-axis was spin, 2. Results were analyzed with Jade 9 WPF software using Rietveld refinement.

3.2. Materials

3.2.1. Sample Source & Radioactive Composition

The majority of the rock core samples were obtained from the WGNHS's geologic repository: the Research Collections and Education Center in Mt. Horeb, Wisconsin. This repository holds a variety of earth-science materials (i.e., rock cores, water-well cuttings, individual rock samples, etc.). Additionally, two rock samples (GW1 and GW3 in Table 3-1) were obtained in the field at the drilling sites for geothermal wells one (GW1) and three (GW3) (Fig. 3-9). The sample from well one was a granite, and the sample from well two was a moderately decomposed granite. Locations for all wells where samples were collected can be seen in Fig. 3-9.

Whole-rock uranium and thorium concentrations for a selection of Wisconsin rocks were completed using gamma-ray spectrometry (Mursky et al., 1988). Results showed that the highest concentrations were found in the younger, more differentiated units of the Wolf River batholith in Marathon County. Here, uranium values range from < 1 mg/kg to > 30 mg/kg and thorium values range from < 5 mg/kg to > 50 mg/kg. The Ninemile Pluton, also in Marathon County, contained concentrations of uranium between < 1 mg/kg and 15.6 mg/kg, and of thorium between 12.1 mg/kg and 56.4 mg/kg. Middle Proterozoic Quartzites and Metaconglomerates in northeastern and northwestern Wisconsin were also investigated. These units contained uranium and thorium concentrations of < 1 mg/kg to 5 mg/kg, and < 1 mg/kg to 32 mg/kg respectively.

Table 3-1: Basic rock sample descriptions from both field samples and from samples collected from Wisconsin's Research Collections and Education Center.

Sample ID	Shelf No.	Hole	Box No.	Core Depth [m]	Rock Type	Formation
From Field Sites						
-	-	GW1	-		Granite	Precambrian
-	-	GW3	-		Granite	Precambrian
From Wisconsin's Research Collections and Education Center						
13-1466	-	NS-2	1	18.3	Sandstone	Tunnel City
10-702	C4-2	Z1-1	3	46.6	Schist	Precambrian
2-111	D3-4	CA-1	1	25.3	Metagabbro	Precambrian
2-111	D3-4	CA-1	3	33.8	Basalt	Precambrian
33-331	O3-6	UPH-1	26	161.8	Sandstone	Jordan
33-331	O3-6	UPH-1	26	169.3	Sandstone	Jordan
33-331	O3-6	UPH-1	30	188.4	Dolomite	St. Lawrence
3-502	D2-2	RL1-1	13	50.3	Barron Quartzite	Barron Quartzite
37-1095	N2-6	K-1	5	16.2	Granite	Precambrian
4-203	F2-5	TL-2	4	27.7	Iron Formation	Iron Formation
9-328	Y3-1	86-1	21	79.2	Schist	Precambrian
9-328	Y3-1	86-1	26	93.7	Greenstone	Precambrian
9-333	K6-4	FR	19	73.3	Andesite	Precambrian
9-333	K6-5	FR	61	192.2	Dacite	Precambrian
9-334	J4-4	F144-B1	1	10.4	Granite	Precambrian

Fig. 3-9: Location of wells from which samples were taken (Google maps). Yellow, red and blue indicates the location where sedimentary, volcanic and metamorphic samples were taken respectively.

3.2.2. Specimen Preparation

3.2.2.1. Thermal Property Specimens

Each sample was drilled using a 2.54-cm-diameter core with a Wilton VSG Twenty (model number 2015) drill press and a diamond coring bit. The samples were then cut to an approximate length of 2.03 cm using a Felker Di-Met rock saw (G68-B CIG027) and/or a Felker Corporation Avco 41-A rock saw (11-1140). Specimen size was controlled by the smallest rock sample core diameter and length available at the Wisconsin Research Collections and Education Center.

To ensure each side of the sample was completely flat, each sample was polished on both ends using a Chevalier surface grinder (FSG-2A818). Once the samples were drilled, cut and polished, two 3-mm-diameter, 6.4-mm-deep holes for the thermocouples were drilled perpendicular to the side of the sample. The 6.4-mm holes were located approximately 0.5 cm from the top and bottom of the sample. These specimens were used both for thermal conductivity and specific heat testing. Fig. 3-10 displays the top and side views of the prepared specimens.

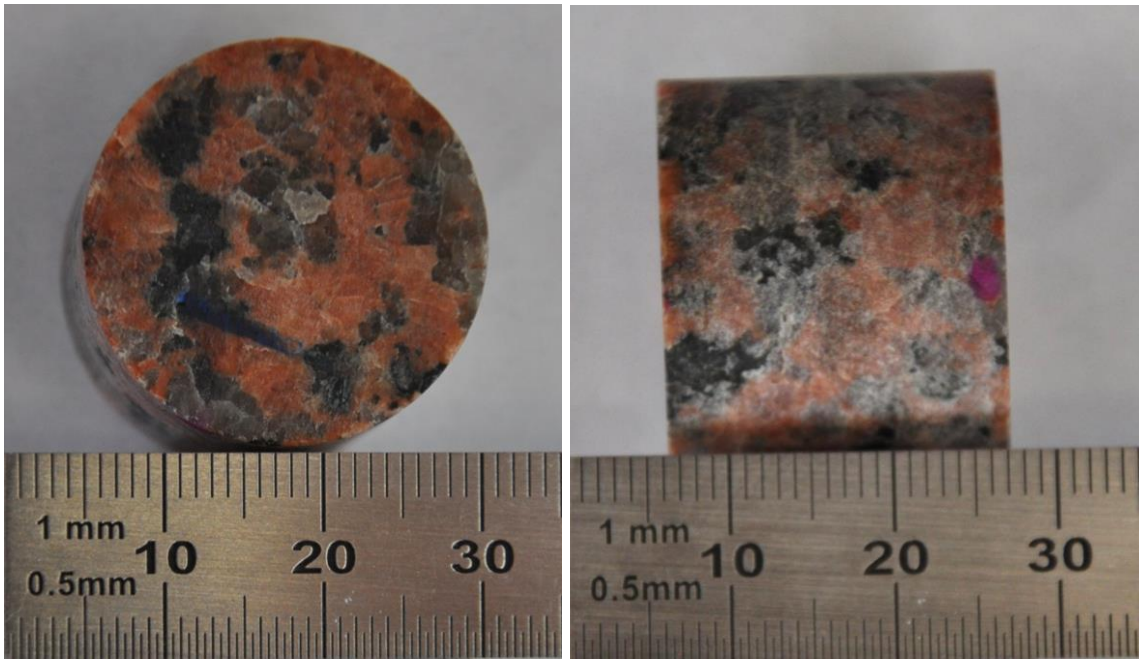

(a) (b)

Fig. 3-10: (a) top view and (b) side view of completed specimens used for thermal conductivity and specific heat testing. Specimens are 2.54 cm in diameter and 2.03 cm in length.

3.2.2.2. X-Ray Diffraction Specimens

For X-ray diffraction, the rock samples were ground to a powder using a rock hammer to break the rock into particles. A mortar and pestle was then used to create a fine powder (passing #200 ASTM sieve or < 75μm). The powder was placed into Hampton Research glass number 50 (borosilicate glass) capillaries. These capillary tubes are extremely thin walled (approximately 0.1-mm thick), resulting in increased X-ray diffraction response intensity.

3.2.3. Specimen Density and Porosity

Table 3-2 summarizes specimen density and porosity values. The Precambrian Schist (Z1-1_153) had the highest porosity of 22.9% followed by the sandstones (UPH-1_531, UPH-1_555, and NS-2_60) which had porosities between 12.8% and 22.2%. The remaining specimens had porosities of 1.6% and below.

Table 3-2: Specimen density and porosity.

WGNHS Sample ID	UW MSN Sample ID	Formation	Rock Type	ρ [kg/m^3]	n [%]
9-333	FR_240	Precambrian	Andesite	2808	0.4
2-111	CA-1_111	Precambrian	Basalt	3191	0.6
9-333	FR_630	Precambrian	Dacite	2718	1
33-331	UPH-1_618	St. Lawrence	Dolomite	2678	5
9-334	F144-B1_34	Precambrian	Granite	2650	1
-	GW1	Precambrian	Granite	2578	1.6
-	GW3-1	Precambrian	Granite	2616	0.7
37-1095	K-1_53	Precambrian	Granite	2604	1
9-328	86-1_307	Precambrian	Greenstone	2956	0.4
4-203	TL-2_91	Iron Formation	Iron Formation	3004	0.8
2-111	CA-1_83	Precambrian	Metagabbro	3722	0.6
3-502	RL1-1_165	Barron Qtz	Quartzite	2602	1.5
13-1466	NS-2_60	Tunnel City	Sandstone	2446	12.8
33-331	UPH-1_531	Jordan	Sandstone	2135	22.2
33-331	UPH-1_555	Jordan	Sandstone	2347	15.3
9-328	86-1_260	Precambrian	Schist	2880	1.8
10-702	Z1-1_153	Precambrian	Schist	2198	22.9

3.2.4. Mineralogical Composition by X-Ray Diffraction

Table 3-3 summarizes the results of the XRD analysis. The major mineral constituents were quartz, feldspar and biotite though some specimens contained large volumes of dolomite, pyroxene, amphibole and magnetite. Olivine and serpentine made up minor mineral constituents. Fig. 8-1 through Fig. 8-3 in APPENDIX B summarize the same results in bar graph form. Igneous specimens contained mainly feldspar, quartz and biotite with some pyroxene and olivine. Sedimentary rocks contained quartz and dolomite. Metamorphic rocks contained mainly quartz, amphibole, biotite and feldspar, some containing magnetite, pyroxene and serpentine. Complete XRD profiles for each specimen can be seen in APPENDIX B.

Table 3-3: XRD results obtained from Rietveld Refinement.

	Mineral Relative Abundance [%]								
Specimen	**Quartz**	**Feldspar**	**Biotite**	**Dolomite**	**Pyroxene**	**Amphibole**	**Olivine**	**Magnetite**	**Serpentine**
Andesite (FR_240)	-	73	22	-	5	-	-	-	-
Basalt (CA-1_111)	-	40	-	-	54	-	6	-	-
Dacite (FR_630)	59	34	7	-	-	-	-	-	-
Dolomite (UPH-1_618)	14	-	-	86	-	-	-	-	-
Granite (F144-B1_34)	44	54	2	-	-	-	-	-	-
Granite (GW1)	55	44	1	-	-	-	-	-	-
Granite (GW3-1)	38	62	-	-	-	-	-	-	-
Granite (K-1_53)	59	41	-	-	-	-	-	-	-
Greenstone (86-1_307)	-	32	-	-	-	68	-	-	-
Iron Formation (TL-2_91)	86	-	11	-	-	-	-	3	-
Metagabbro (CA-1_83)	-	-	-	-	26	-	-	74	-
Quatzite (RL1-1_165)	100	-	-	-	-	-	-	-	-
Sandstone (NS-2_60)	41	-	-	59	-	-	-	-	-
Sandstone (UPH-1_531)	100	-	-	-	-	-	-	-	-
Sandstone (UHP-1_555)	80	-	-	20	-	-	-	-	-
Schist (860-1_260)	7	39	23	-	-	31	-	-	-
Schist (Z1-1_153)	91	-	2	-	-	-	-	-	7

4. RESULTS AND DISCUSSION

4.1. Thermal Conductivity

Using the guarded-comparative-longitudinal heat flow apparatus, thermal conductivities between 2.30 W m^{-1} K^{-1} and 6.71 W m^{-1} K^{-1} were measured. The thermal conductivity for the majority of the specimens (omitting the Barron Quartzite and St. Lawrence Dolomite) ranged between 2.30 W m^{-1} K^{-1} and 3.86 W m^{-1} K^{-1}. The Barron Quartzite had the highest thermal conductivity (6.71 W m^{-1} K^{-1}), and the St. Lawrence Dolomite had the second highest thermal conductivity (4.67 W m^{-1} K^{-1}). The thermal conductivity of the Precambrian Granites ranged from 3.10 W m^{-1} K^{-1} to 3.69 W m^{-1} K^{-1}. Sandstones ranged between 2.59 W m^{-1} K^{-1} and 3.86 W m^{-1} K^{-1}.

Table 4-1 compares the experimental results to estimated values based on literature (Kavanaugh et al., 1997; Jaupart & Mareschel, 2011; Vosteen & Schellschmidt, 2003; Touloukain et al., 1981), and calculated thermal conductivities based on a weighted average from XRD analysis (Horai & Simmons, 1969; Clauser & Huenges, 1995). The following mixture model was used to determine the calculated thermal conductivities:

$$\lambda^{\beta} = (1-n)\lambda_m^{\beta} + n(1-S_r)\lambda_a^{\beta} \quad [27]$$

where λ^{β} is the calculated thermal conductivity [W m^{-1} K^{-1}] based on the parameter β which is equal to 0.1, n is the porosity, λ_m is the mineral thermal conductivity [W m^{-1} K^{-1}], S_r is the saturation, and λ_a is the thermal conductivity of air [W m^{-1} K^{-1}]. The majority of the measured thermal conductivities fall within the estimated range from literature. Additionally, the calculated thermal conductivities based on the mixture

model match the experimental results due to the ability to account for porosity in the calculated thermal conductivity values (Fig. 4-1). To account for variations due to specimen anisotropies, a parallel/series mixture analysis was also completed based on the following equations:

$$\lambda_p = (1 - n) * \lambda_m + \lambda_a * n \quad [28]$$

$$\lambda_s = \frac{1}{\frac{(1-n)}{\lambda_m} + \frac{n}{\lambda_a}} \quad [29]$$

where λ_p is the thermal conductivity in the parallel direction [W m^{-1} K^{-1}], and λ_s is the thermal conductivity in the series direction [W m^{-1} K^{-1}]. This analysis assesses the extreme effect of porosity and mineral/grain orientation on the thermal conductivity of each individual rock by assuming a completely parallel or series arrangement of solids and air. Thus, based on the composition of the specimens, the parallel/series analysis provided a broader predicted range for the thermal conductivities of the specimens. Most of the values fell within the expected range for this analysis (Fig. 4-2). Specimens with thermal conductivities near the center of the parallel/series range suggest specimen homogeneity (Granite, Sandstone, and Dacite). Conversely, specimens with thermal conductivities closer to the outer bounds of their parallel/series range suggest specimen anisotropy likely in the form of banding, foliations or lineations (Iron Formation, Greenstone, Schist, Basalt, Metagabbro, Dolomite, and Quartzite). Additional deviations from the expected or calculated values may be attributed to anisotropy or porosity of the specimens and inaccuracies in the XRD analysis (relative mineral abundances).

Thermal conductivity values were compared to porosity, as well as quartz and dolomite content. As stated by Clauser & Huenges (1995), the controlling factor in thermal conductivity for sedimentary rocks is the porosity and cementation of the rocks. This is because the water and air filling the void spaces of the porous matrix is fairly low in thermal conductivity, thus decreasing the bulk thermal conductivity of the rock (Table 2-1). Among the sedimentary specimens (UPH-618, UPH-1_555, UPH-1_531, NS-2_60), no general trend can be drawn between porosity and thermal conductivity (Fig. 4-3). This is likely due to the small number of specimens tested. The effect of porosity can be seen in a general sense when comparing the thermal conductivity of the sedimentary rocks to that of the quartzite. Quartzites have significantly lower porosities (approximately 0.0 – 0.05) than sedimentary rocks due to the pressure and temperature they are exposed to during metamorphism. The sedimentary rocks have thermal conductivity values ranging from 2.59 W m^{-1} K^{-1} to 4.67 W m^{-1} K^{-1}, while the quartzite had a thermal conductivity of 6.71 W m^{-1} K^{-1}.

Among the igneous rocks, quartz and feldspar content are the main controlling factors in thermal conductivity because the thermal conductivity of quartz (6.5 – 7.7 W m^{-1} K^{-1}) is higher than that of feldspars (approximately 1.5 – 2.5 W m^{-1} K^{-1}) (Clauser & Huenges, 1995; Horai & Simmons, 1969). The expected trend would be an increase in thermal conductivity with an increase in quartz content. Not all of the specimens follow this trend, though in general, thermal conductivities of the igneous specimens did increase with increasing quartz content (Fig. 4-4). As seen in

Fig. 4-3, the igneous rocks contradict the expected trend showing an increase in thermal conductivity with increasing porosity.

Determining a trend among the metamorphic rocks was slightly more difficult due to the variation in minerals present. Again, among the metamorphic rocks, quartz and feldspar content are the main controlling factors in thermal conductivity, though magnetite in this case plays a controlling factor as well due to its high thermal conductivity of 5.1 W m^{-1} K^{-1} (Horai & Simmons, 1969). In general the metamorphic rocks tested have a lower thermal conductivity due to the prevalence of minerals with lower thermal conductivity values such as feldspar, amphibole, biotite, and serpentine (approximately 1.5 W m^{-1} K^{-1} – 3.0 W m^{-1} K^{-1}). Although it was not tested, laminations and foliations in metamorphic rocks would also act as a controlling factor of the thermal conductivity. The thermal conductivity of a rock would be lower perpendicular to its laminations and foliations versus parallel to it due to ease of heat flow along the lamination and foliation planes. Additional comparisons of data can be seen in APPENDIX A.

Deviations of thermal conductivity values from literature values, calculated values and expected trends emphasize the importance of laboratory or *in situ* thermal conductivity measurements. The thermal conductivity within a given rock type can vary by a factor of two or three due to anisotropies on the microscopic (mineralogy), laboratory (foliations, laminations, etc.), and field (bedding, folding, fractures, pressure, temperature, etc.) scales (Clauser & Huenges, 1995). Danko & Mousset-Jones (1989 and 1991) showed laboratory results up to 20% lower than

those collected in the field. Thus, field tests are recommended for future testing. Additionally, errors may have been introduced to the experimental results through the following: (a) lack of perfect contact between specimen and reference materials, (b) contact between thermocouples and rocks, (c) exposure to coolant during specimen preparation (smoothing of surfaces using surface grinder), (d) calculated heat flux in ≠ calculated heat flux out, and (e) specimen size. Based on the 95% confidence interval experimental error analysis (maximum error of ± 0.70 W m^{-1} K^{-1}), these errors appear to be minimal.

Table 4-1: Thermal conductivity values for selected Wisconsin rocks using ASTM E1225. Literature values obtained from Kavanaugh et al. (1997), Clauser & Hugenges (1995), Jaupart & Marschel (2011), Touloukain et al. (1981) and Vosteen & Schellschmidt (2003). Calculated values based on Horai & Simmons (1969) and Clauser & Huenges (1995).

UW MSN Sample ID	Rock Type	ρ [kg/m^3]	λ [W m^{-1} K^{-1}]	Calculated λ [W m^{-1} K^{-1}]	λ from Literature [W m-1 K-1]
FR_240	Andesite	2808	3.09 ± 0.05	1.77	1.4 - 4.8
CA-1_111	Basalt	3191	2.93 ± 0.45	3.20	2.1 - 2.4
FR_630	Dacite	2718	3.76 ± 0.06	4.47	1.5 - 2.5
UPH-1_618	Dolomite	2678	4.67 ± 0.24	5.65	1.6 - 6.2
F144-B1_34	Granite	2650	3.10 ± 0.40	3.96	1.9 - 5.2
GW1	Granite	2578	3.69 ± 0.07	4.45	1.9 - 5.2
GW3-1	Granite	2616	3.35 ± 0.10	3.68	1.9 - 5.2
K-1_53	Granite	2604	3.36 ± 0.22	4.61	1.9 - 5.2
86-1_307	Greenstone	2956	2.57 ± 0.04	2.74	1.0 - 3.0
TL-2_91	Iron Formation	3004	2.47 ± 0.34	5.92	1.5 - 2.4
CA-1_83	Metagabbro	3722	2.94 ± 0.18	4.90	2.0 - 2.8
RL1-1_165	Quartzite	2602	6.71 ± 0.67	6.50	5.2 - 6.9
NS-2_60	Sandstone	2446	2.59 ± 0.38	5.91	2.1 - 3.5
UPH-1_531	Sandstone	2135	3.34 ± 0.46	6.50	2.1 - 3.5
UPH-1_555	Sandstone	2347	3.86 ± 0.59	6.30	2.1 - 3.5
86-1_260	Schist	2880	2.58 ± 0.70	2.38	2.1 - 4.5
Z1-1_153	Schist	2198	2.30 ± 0.05	6.14	2.1 - 4.5

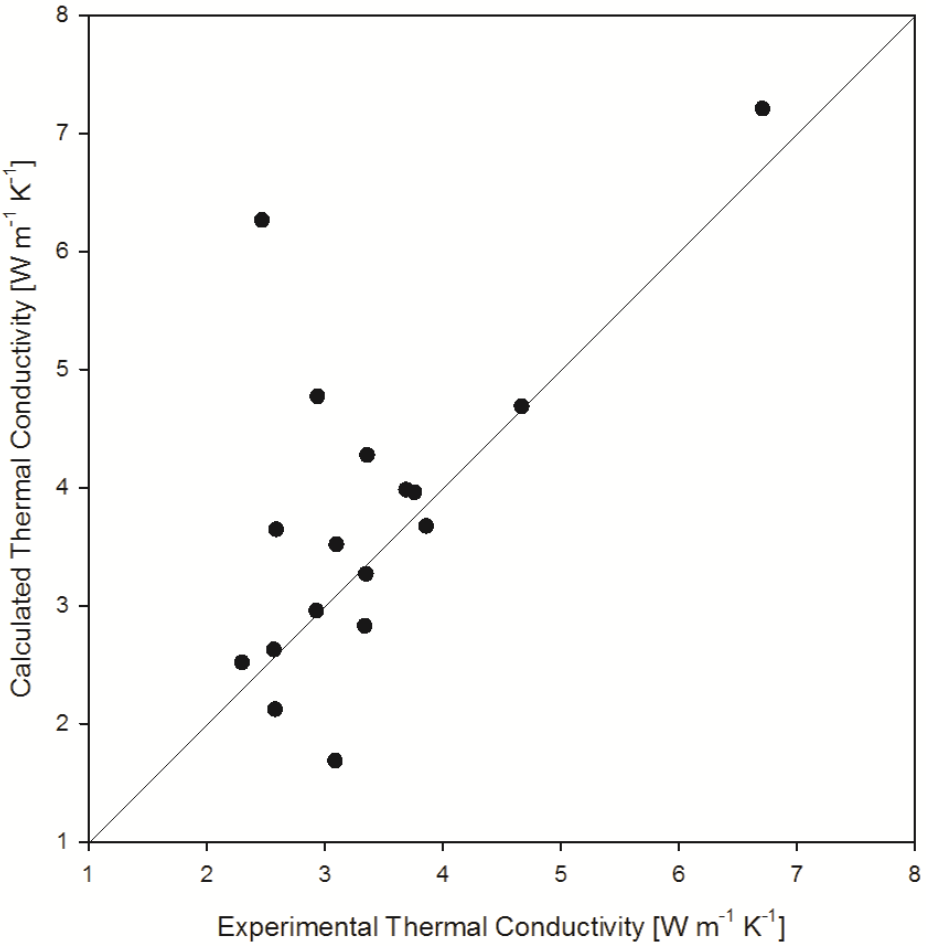

Fig. 4-1: Comparison of experimental thermal conductivity and calculated thermal conductivity from mixture model (Horai & Simmons, 1969; Clauser & Huenges, 1995).

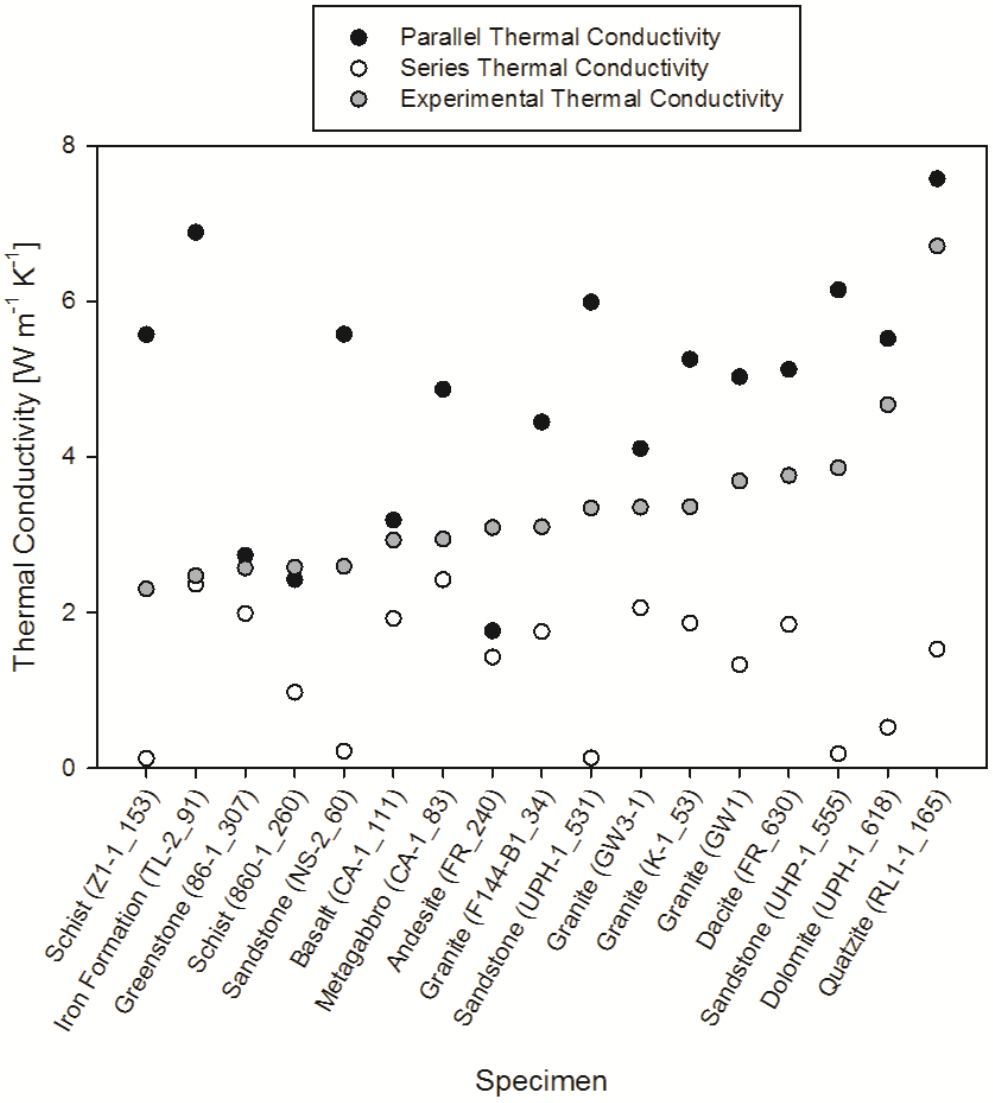

Fig. 4-2: Comparison of experimental thermal conductivity to parallel and series mixture analysis.

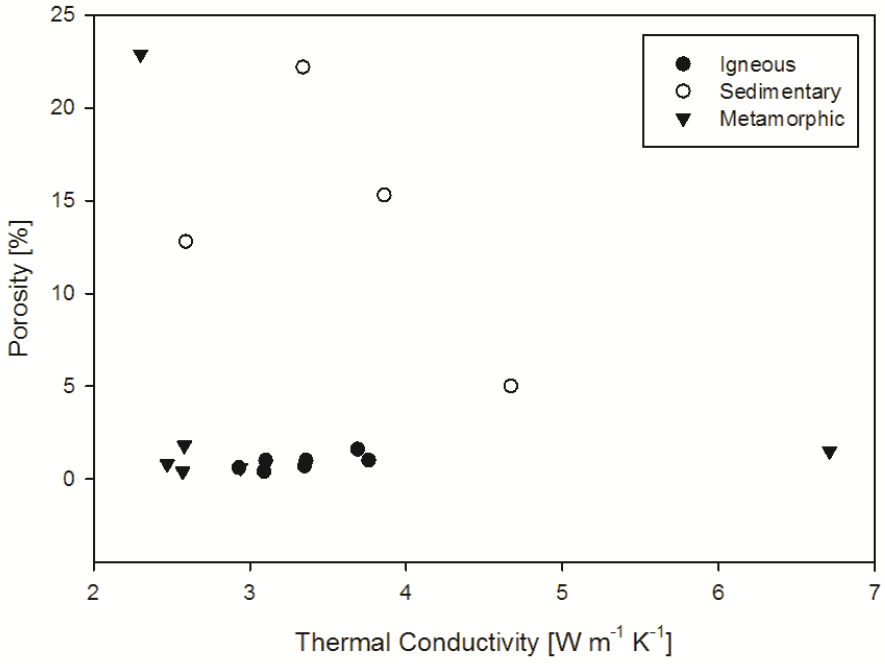

Fig. 4-3: Thermal conductivity of all specimens compared to specimen porosity.

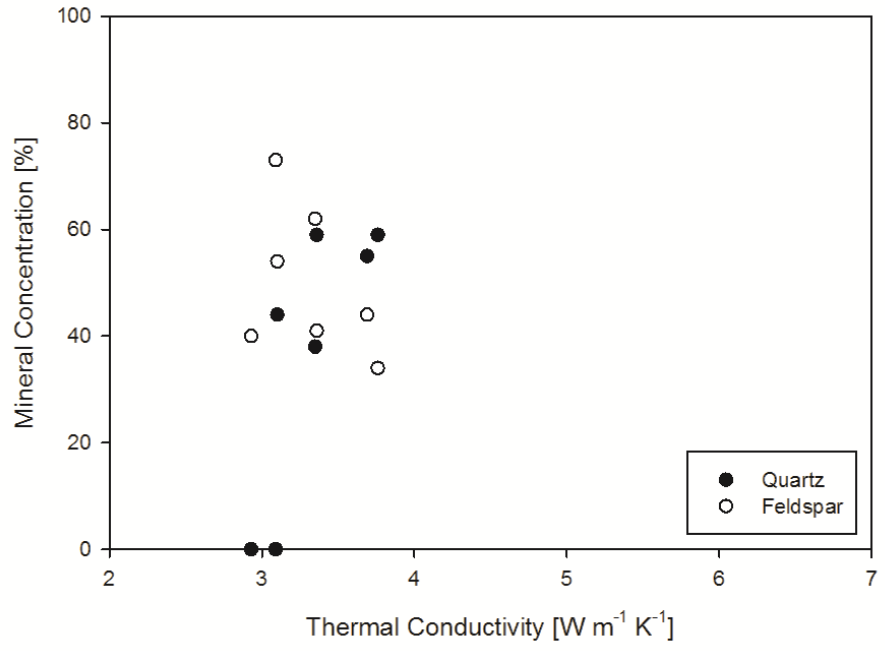

Fig. 4-4: Thermal conductivity of igneous specimens with quartz and feldspar content.

4.2. Specific Heat

Using the “coffee-cup” calorimeter, specific heat values between 713 J kg^{-1} K^{-1} and 891 J kg^{-1} K^{-1} were obtained. The Tunnel City Sandstone had the highest specific heat (891 J kg^{-1} K^{-1}), and the St. Lawrence Dolomite had the second highest specific heat (872 J kg^{-1} K^{-1}). The specific heat of the Precambrian Granites ranged between 824 J kg^{-1} K^{-1} and 729 J kg^{-1} K^{-1}. Sandstones ranged between 818 J kg^{-1} K^{-1} and 891 J kg^{-1} K^{-1}.

Table 4-2 compares experimental results to calculated specific heat values based on a weighted average from the XRD analysis (Waples & Waples, 2004), and estimated values based on literature (Kavanaugh et al., 1997; Vosteen & Schellschmidt, 2003). The following mixture model was used to determine the calculated specific heats:

$$C_p^{\beta} = (1-n)C_{pm}^{\beta} + n(1-S_r)C_{pa}^{\beta} \quad [30]$$

where C_p^{β} is the calculated specific heat [J kg^{-1} K^{-1}] based on the parameter β which is equal to 1, n is the porosity, C_{pm} is the mineral specific heat [J kg^{-1} K^{-1}], S_r is the saturation, and C_{pa} is the specific heat of air [J kg^{-1} K^{-1}]. The majority of the measured specific heats fall within the range expected from literature. Additionally, the calculated thermal conductivities based on the mixture model match the experimental results due to the ability to account for porosity in the calculated thermal conductivity values (Fig. 4-5). Any deviations from the expected or calculated values can be attributed to mineral density of the specimens and inaccuracies in the XRD analysis (relative mineral abundances).

The sedimentary rocks tested had specific heat values near the lower end of the estimated specific heat from literature. Furthermore, the calculated specific heat values from these same specimens typically were lower than the estimated values from literature. Waples & Waples (2004) stated that the specific heat of mafic and felsic rocks should be similar to those of sedimentary rocks but lower than ultramafic rocks, which have low silica content. Dolomite content also plays a role due to its high specific heat (approximately 870 J kg^{-1} K^{-1}). For the rocks tested, the specific heat values for the sedimentary and igneous rocks fall between 730 J kg^{-1} K^{-1} and 890 J kg^{-1} K^{-1}, the lower values are generally from rocks with lower silica content. Fig. 4-6 summarizes the specific heat of the sedimentary rocks with variations in quartz and dolomite content, and Fig. 4-7 summarizes the specific heat of the igneous rocks with variations in quartz and feldspar content. Due to the small number of specimens tested, trends are difficult to identify on these plots. Fig. 4-8 shows the change in specific heat with density. A general trend of increasing specific heat with decreasing density can be seen.

Waples & Waples (2004) also state that rocks with high concentrations of metallic minerals have the lowest specific heat values. Overall, this is true for the metagabbro (CA-1_83) and iron formation (TL-2_91) specimens tested that contained magnetite. These two specimens had the lowest and second lowest specific heats of all rocks tested at 723 J kg^{-1} K^{-1} and 713 J kg^{-1} K^{-1} respectively. A comparison of these rocks to other metamorphic rocks can be seen in APPENDIX A, along with other specific heat comparisons that yielded insignificant trends.

As with thermal conductivity, the deviation of specific heat from literature values, calculated values and expected trends emphasize the importance of laboratory or *in situ* specific heat measurements. As discussed, many variables affect the specific heat of a given rock. Thus, simply selecting a value based on rock type, mineralogy, or density may yield inaccurate analysis of a GSHP system.

For calorimetry testing, experimental errors may have been introduced through the following: (a) heat loss during specimen transfer from oven to calorimeter cup, (b) heterogeneity of water temperature in calorimeter cup, (c) oven temperature variation effecting equilibrium state of specimen used for determining specific heat, and (d) specimen size (Schärli & Rybach, 2001). Based on the 95% confidence interval experimental error analysis (maximum error of ± 69 J kg^{-1} K^{-1}), these errors appear to be minimal.

Table 4-2: Specific Heat values for selected Wisconsin rocks using a coffee-cup calorimeter. Literature values obtained from Kavanaugh et al. (1997), Touloukain et al. (1981), Vosteen & Schellschmidt (2003). Calculated values based on Waples & Waples (2004).

UW MSN Sample ID	Rock Type	ρ [kg/m^3]	C_p [J kg^{-1} K^{-1}]	Calculated C_p [J kg^{-1} K^{-1}]	C_p from Literature [J kg^{-1} K^{-1}]
FR_240	Andesite	2808	745 ± 27	725	502
CA-1_111	Basalt	3191	770 ± 39	714	712 - 879
FR_630	Dacite	2718	807 ± 27	732	879
UPH-1_618	Dolomite	2678	872 ± 69	852	879
F144-B1_34	Granite	2650	824 ± 38	735	879
GW1	Granite	2578	729 ± 27	736	879
GW3-1	Granite	2616	736 ± 10	734	879
K-1_53	Granite	2604	802 ± 41	736	879
86-1_307	Greenstone	2956	765 ± 16	732	775
TL-2_91	Iron Formation	3004	713 ± 16	740	879
CA-1_83	Metagabbro	3722	723 ± 58	629	754
RL1-1_165	Quartzite	2602	714 ± 22	740	837
NS-2_60	Sandstone	2446	891 ± 58	817	825 - 1005
UPH-1_531	Sandstone	2135	818 ± 42	740	825 - 1005
UPH-1_555	Sandstone	2347	818 ± 42	766	825 - 1005
86-1_260	Schist	2880	798 ± 38	746	775
Z1-1_153	Schist	2198	868 ± 39	734	775

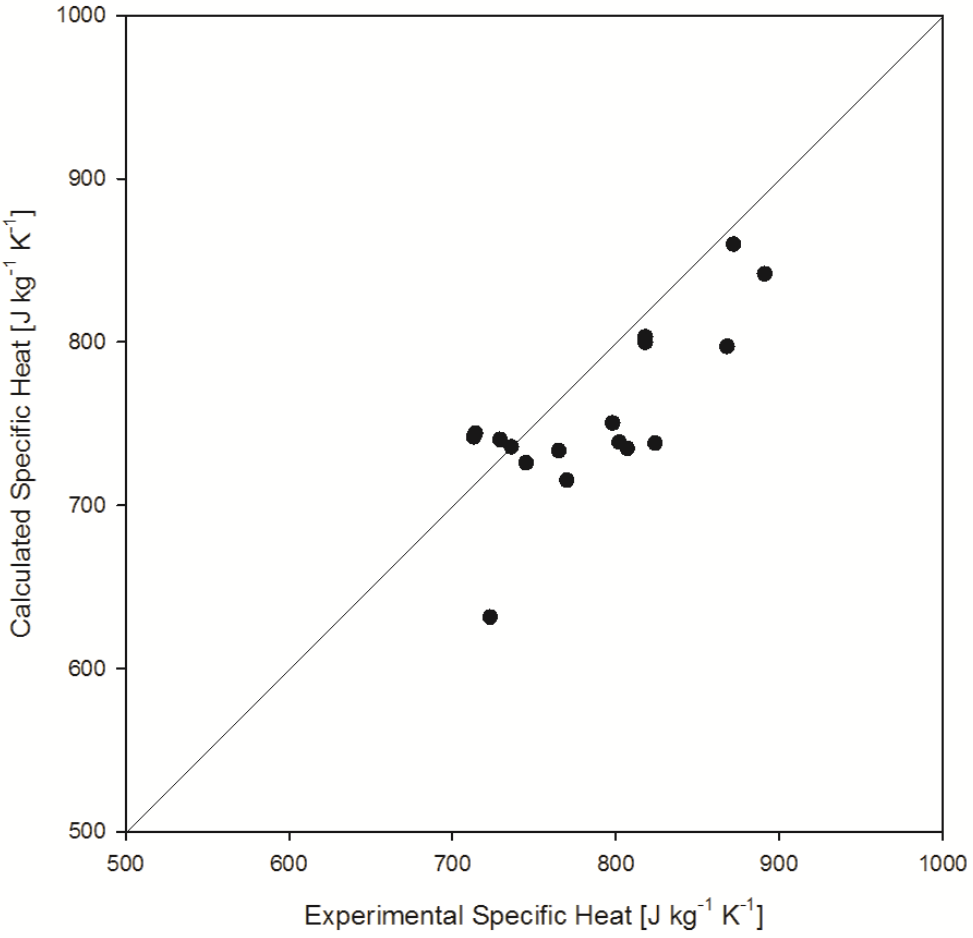

Fig. 4-5: Comparison of experimental specific heat and calculated specific heat from Waples & Waples (2004).

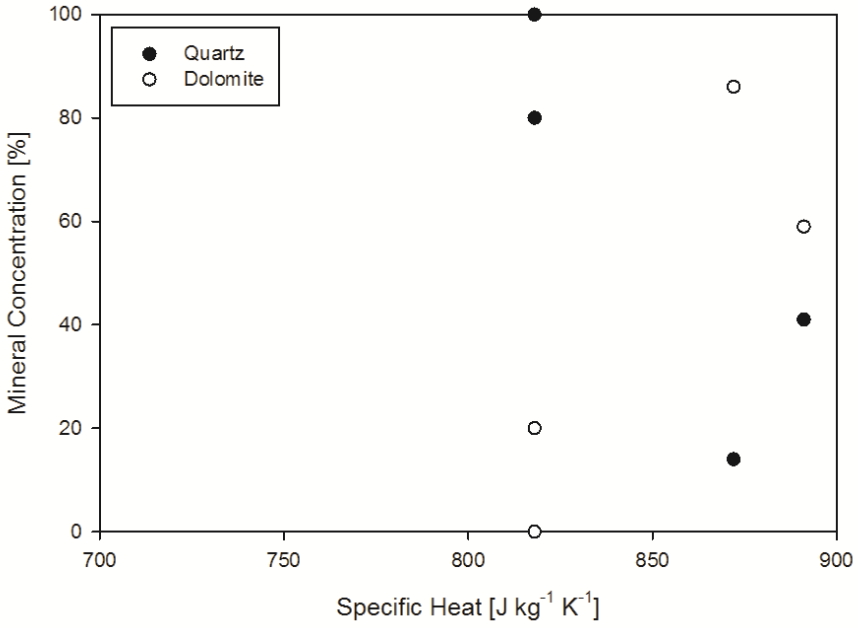

Fig. 4-6: Specific heat of sedimentary specimens with quartz and dolomite content.

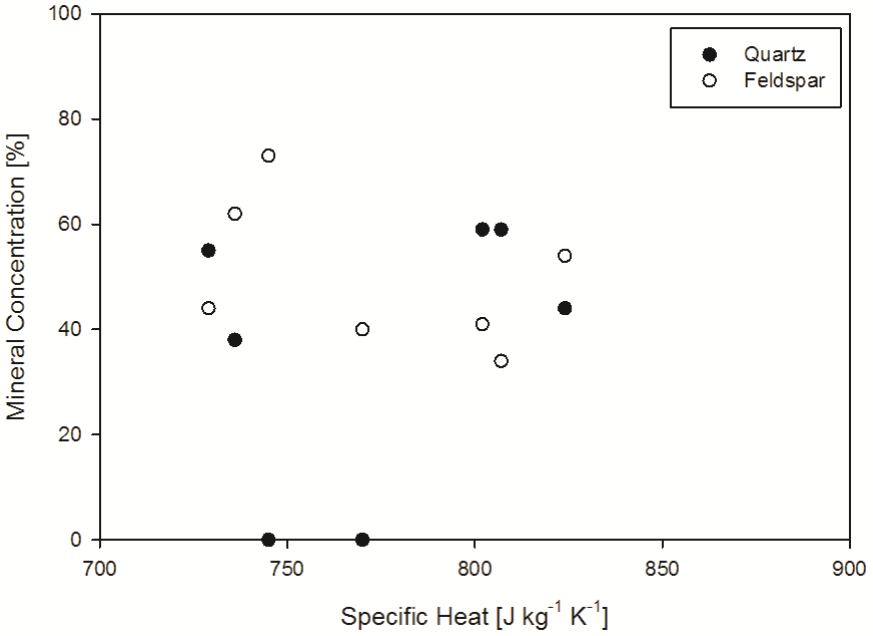

Fig. 4-7: Specific heat of igneous specimens with quartz and feldspar content.

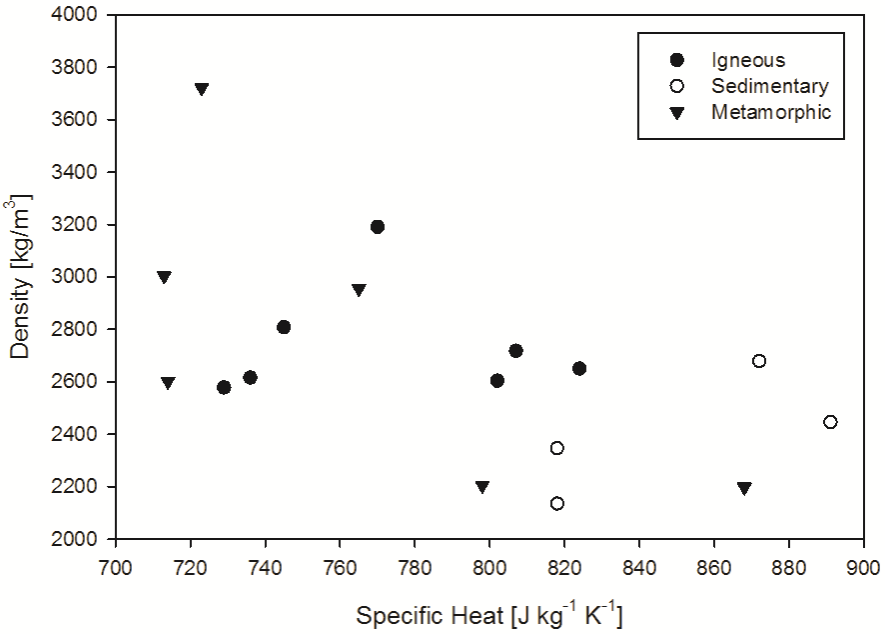

Fig. 4-8: Specific heat of all specimens compared to specimen density.

5. CONCLUSIONS

Thermal properties of Wisconsin rocks were explored through laboratory testing of thermal conductivity and specific heat. Thermal conductivity values between 2.30 W m^{-1} K^{-1} and 6.71 W m^{-1} K^{-1}, and specific heat values between 713 J kg^{-1} K^{-1} and 891 J kg^{-1} K^{-1} were measured for a selection of Wisconsin rocks. As supported by literature, the controlling factors for rock thermal properties are mineralogical content, specifically quartz and feldspar, as well as density, porosity and cementation. Silica and metallic mineral content also play a role in the specific heat of the tested rocks, though are not as strongly correlated. To fully examine these trends, further testing should be completed on a wider selection of specimens.

In some instances, experimental results for thermal conductivity and specific heat varied slightly from literature values, calculated values based on mineralogical fraction, and expected trends based on porosity, mineralogical content and density. These deviations emphasize the importance of laboratory or *in situ* thermal conductivity measurements prior to GSHP system design. If not evaluated carefully, system design based on estimated thermal property values could result in over or under design of the system, and thus system inefficiency. The thermal property values presented in this document represent the beginning of a thermal property database that will be recommended for use in the advancing geothermal industry in Wisconsin.

6. FUTURE STUDY

Moving forward, a more thorough analysis of rock thermal properties could be completed to include the rest of Wisconsin's rock formations, as well as properties of saturated rocks since many GSHPs are installed under saturated conditions, especially those installed in rock. Additionally, rock formation thermal properties could be characterized across different locations in Wisconsin to emphasize local variances and the effect of extraction depth. This data could be used to compile a complete thermal property database to aid the geothermal industry in Wisconsin. A thorough parametric study could be completed to determine how strongly rock thermal properties control system design, efficiency and cost since the variation of thermal properties with rock type is small. Lastly, due to effects of anisotropies across microscopic, laboratory, and field scales, *in situ* thermal property testing methods is an area that warrants further research.

To better understand Wisconsin's heat potential, additional data should be collected to further analyze Wisconsin's thermal gradient, heat capacity and heat production. Specifically, wells in northern Wisconsin could be logged, and the final three 300 m geothermal wells drilled (GW6, GW7, and GW8). In addition, further exploration of the effect of glaciation on thermal gradient in Wisconsin using very deep boreholes would be of interest, as would the use of geothermal profiles to evaluate and predict the impacts of global warming.

7. APPENDIX A

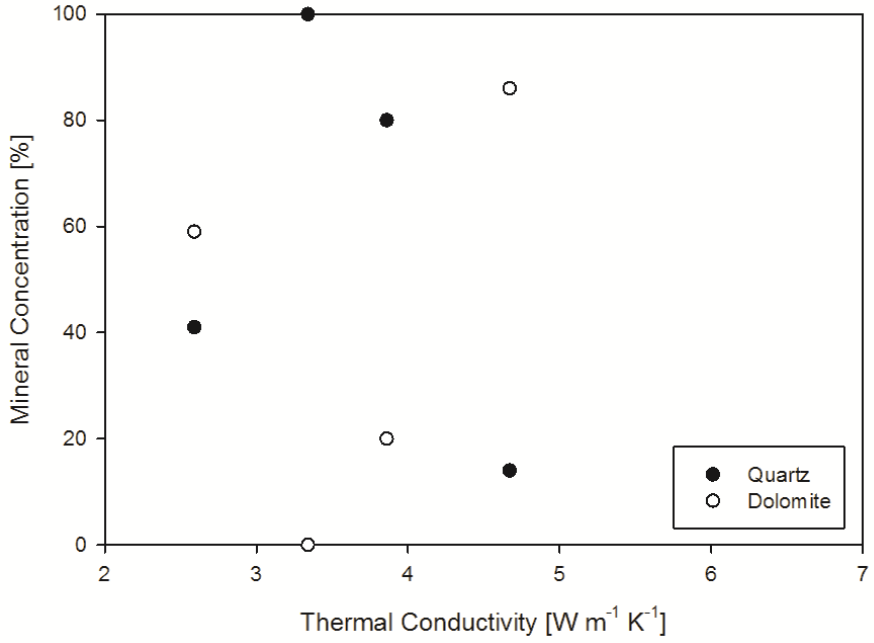

Fig. 7-1: Thermal conductivity of sedimentary specimens with quartz and dolomite content.

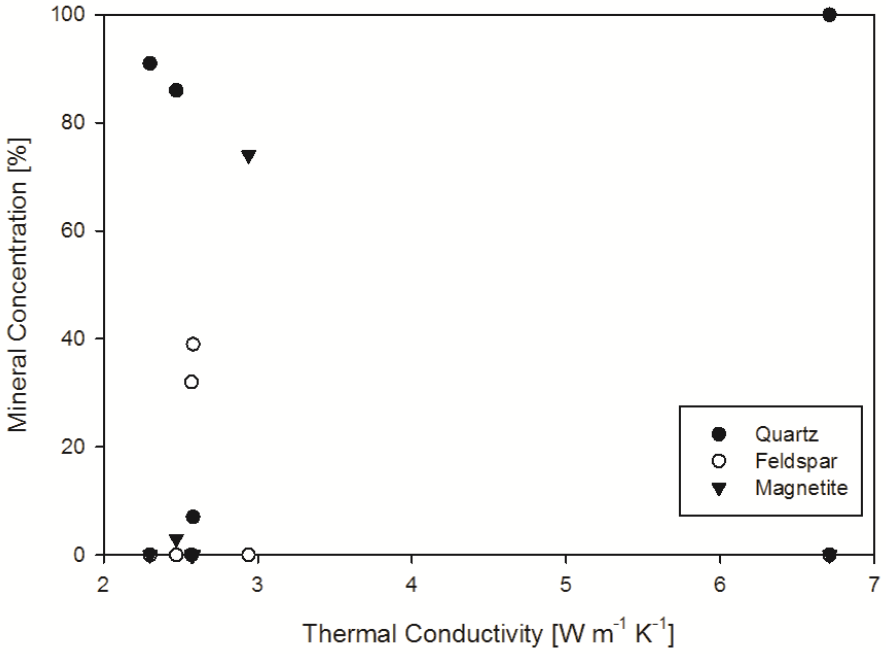

Fig. 7-2: Thermal conductivity of metamorphic specimens with quartz, feldspar and magnetite content.

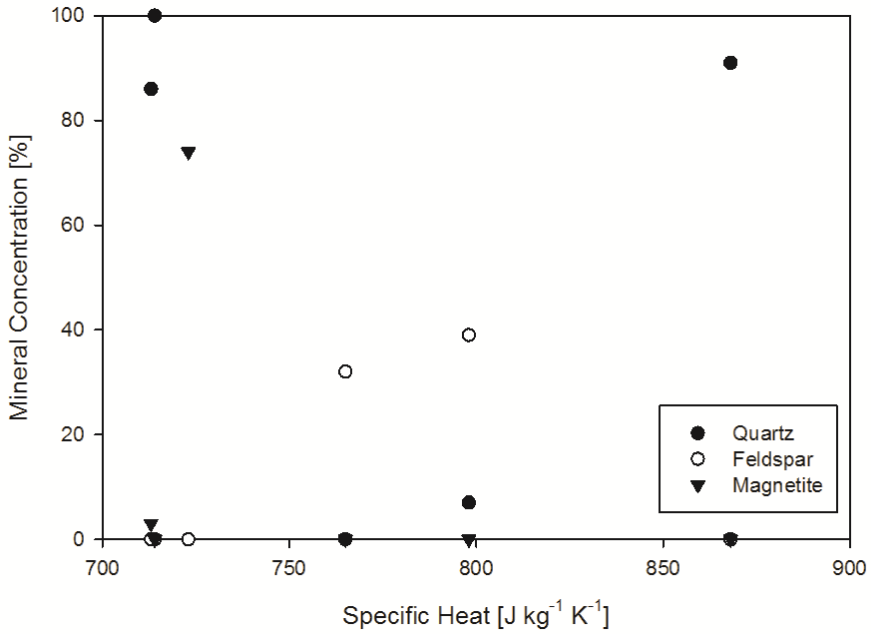

Fig. 7-3: Specific heat of metamorphic specimens with quartz, feldspar and magnetite content.

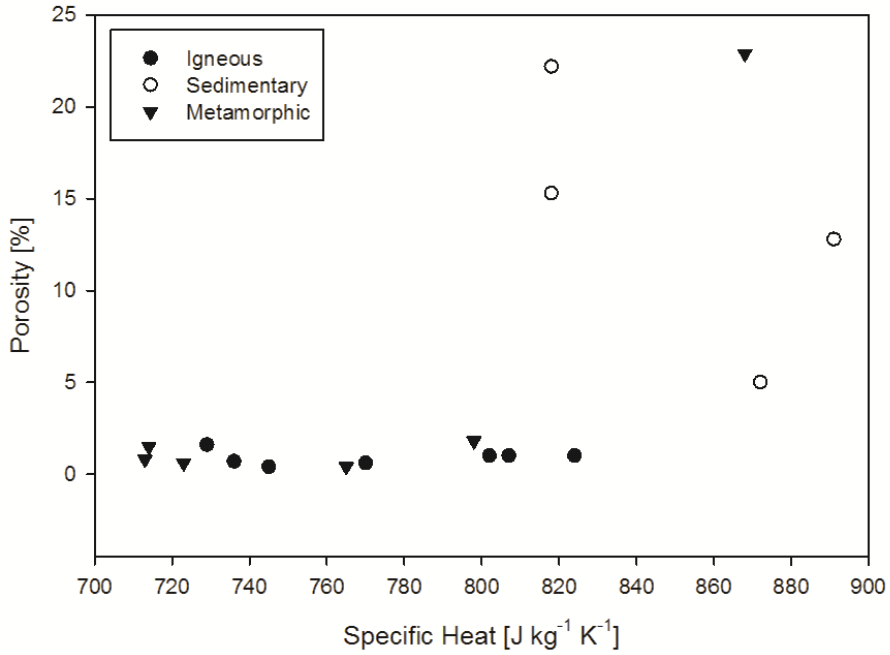

Fig. 7-4: Specific heat of all specimens compared to specimen porosity.

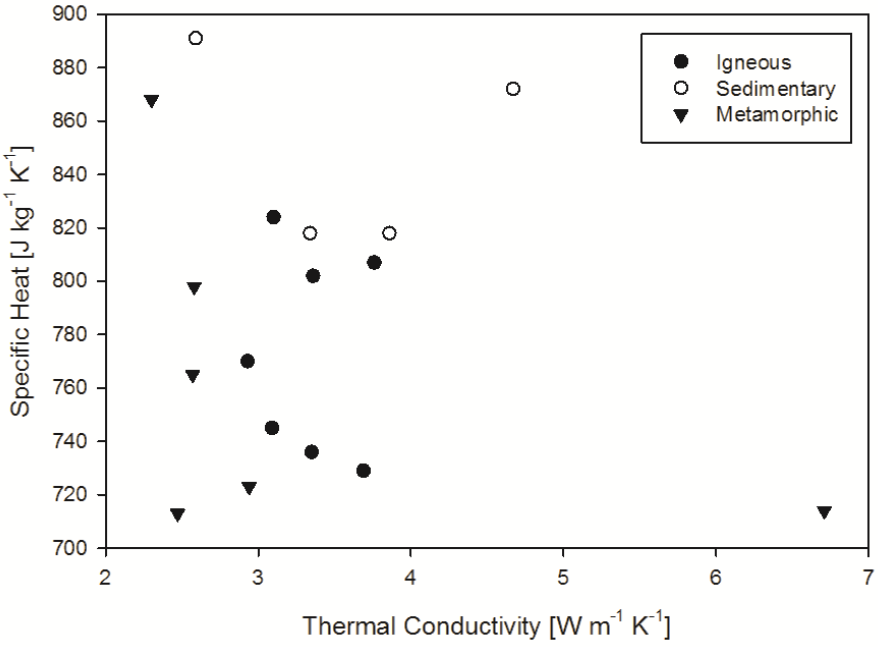

Fig. 7-5: Comparison of thermal conductivity to specific heat for all specimens.

8. APPENDIX B

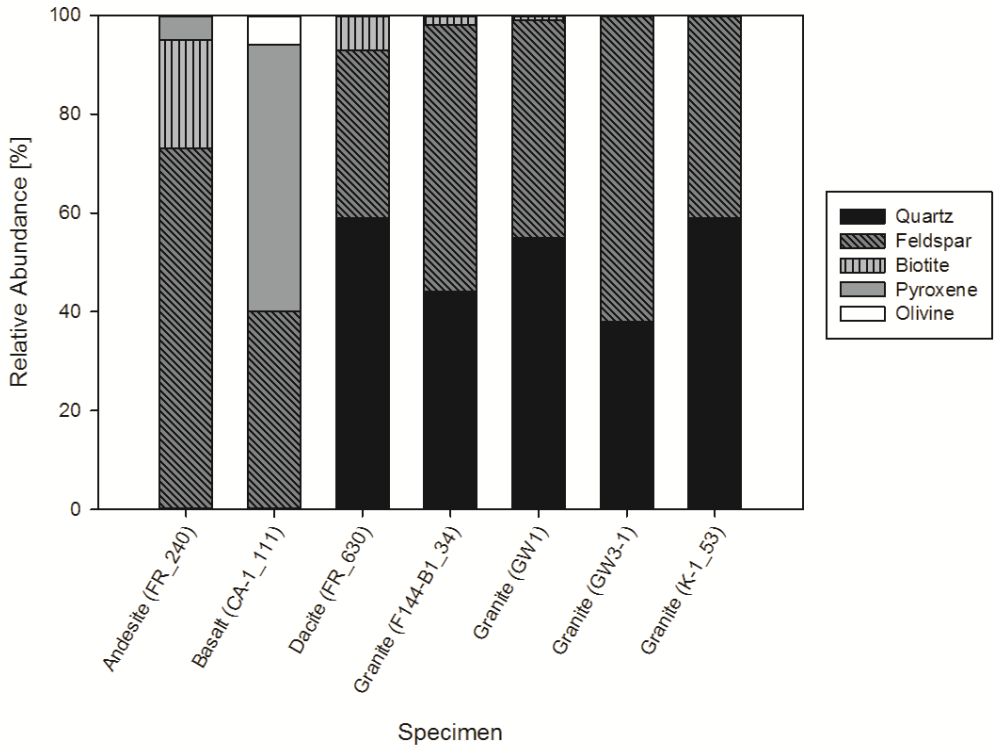

Fig. 8-1: X-ray Diffraction results for igneous specimens.

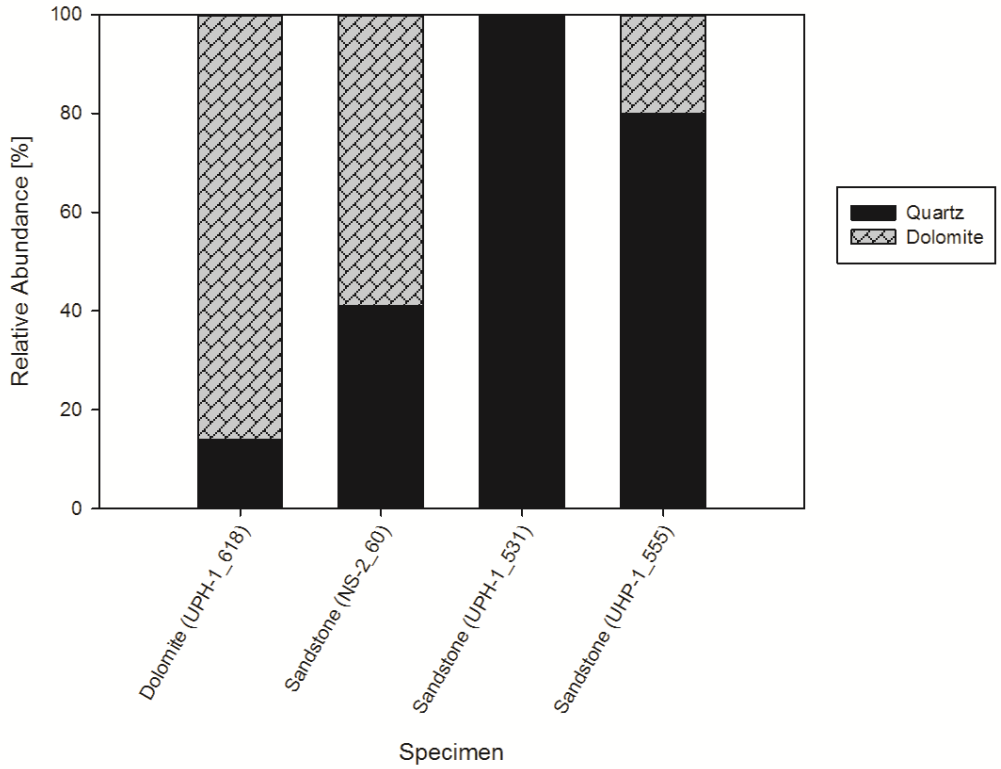

Fig. 8-2: X-ray Diffraction results for sedimentary specimens.

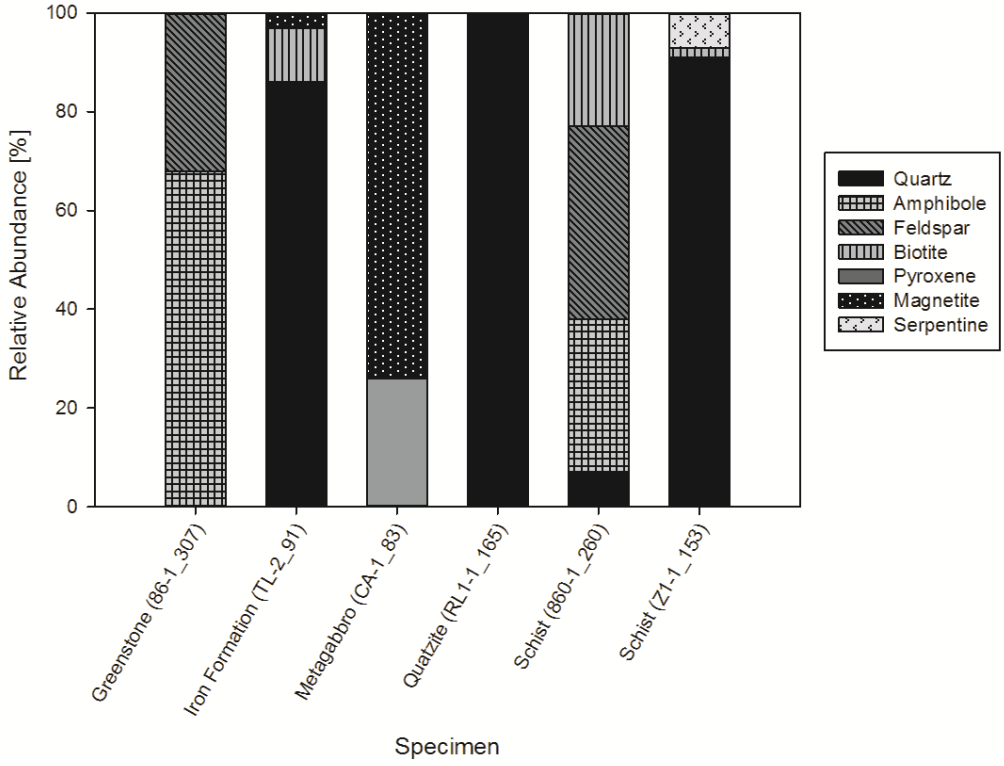

Fig. 8-3: X-ray Diffraction results for metamorphic specimens.

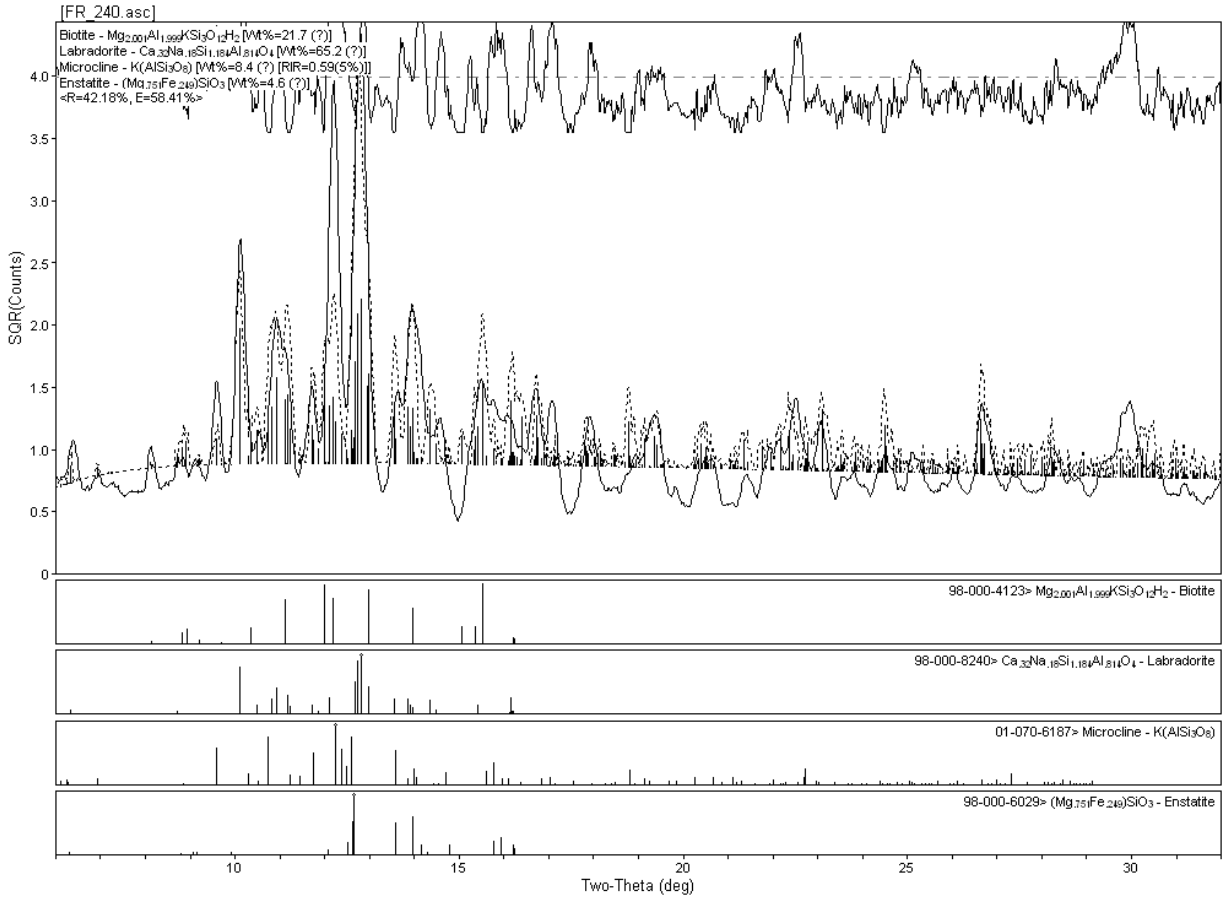

Fig. 8-4: XRD pattern for FR_240 (andesite).

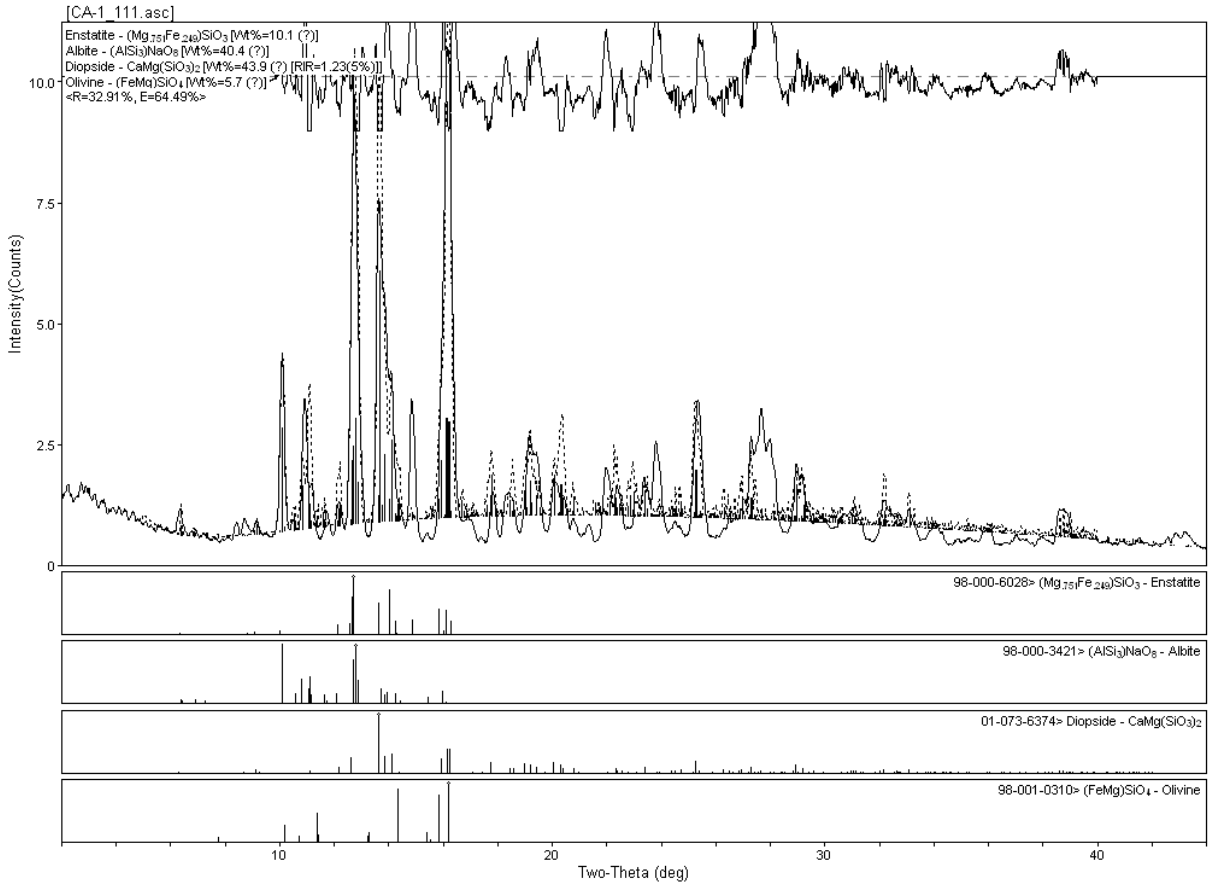

Fig. 8-5: XRD pattern for CA-1_111 (basalt).

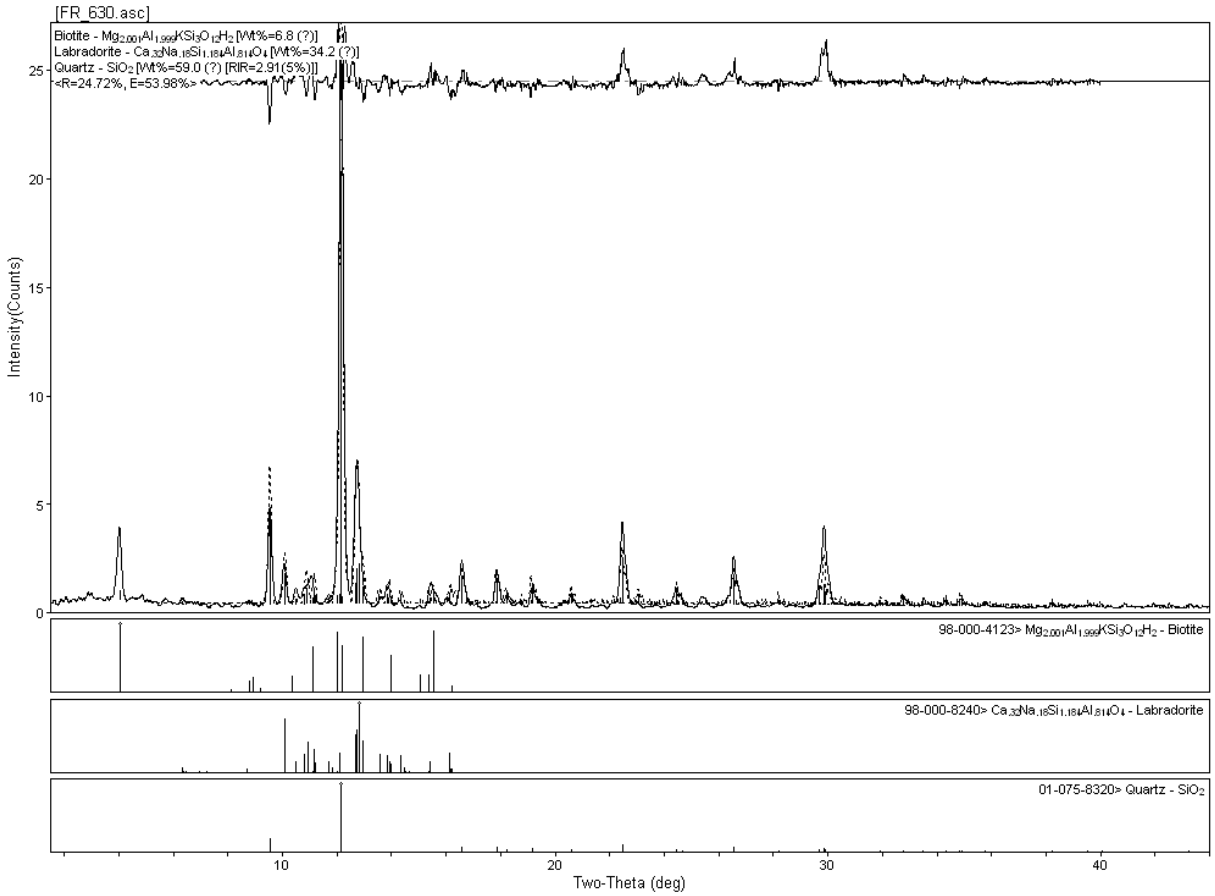

Fig. 8-6: XRD pattern for FR_630 (dacite).

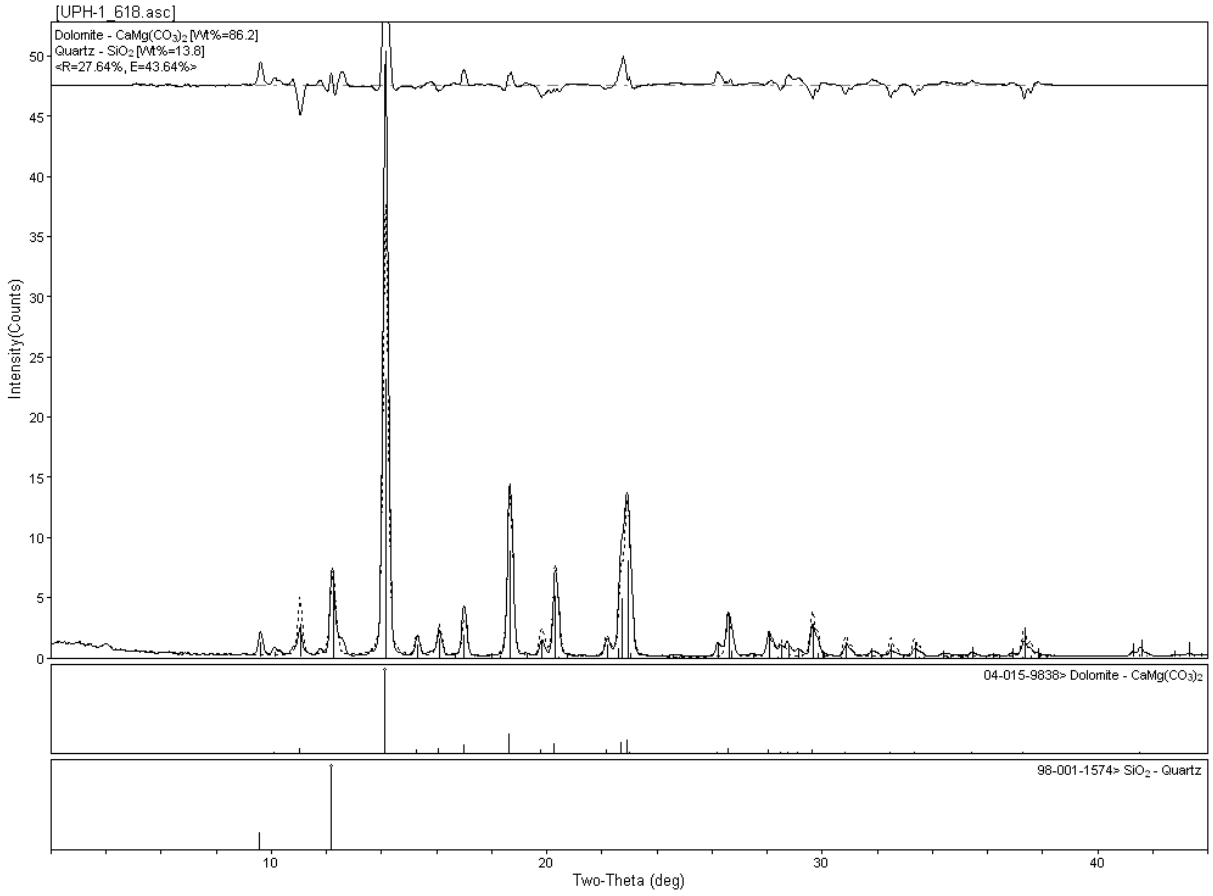

Fig. 8-7: XRD pattern for UPH-1_618 (dolomite).

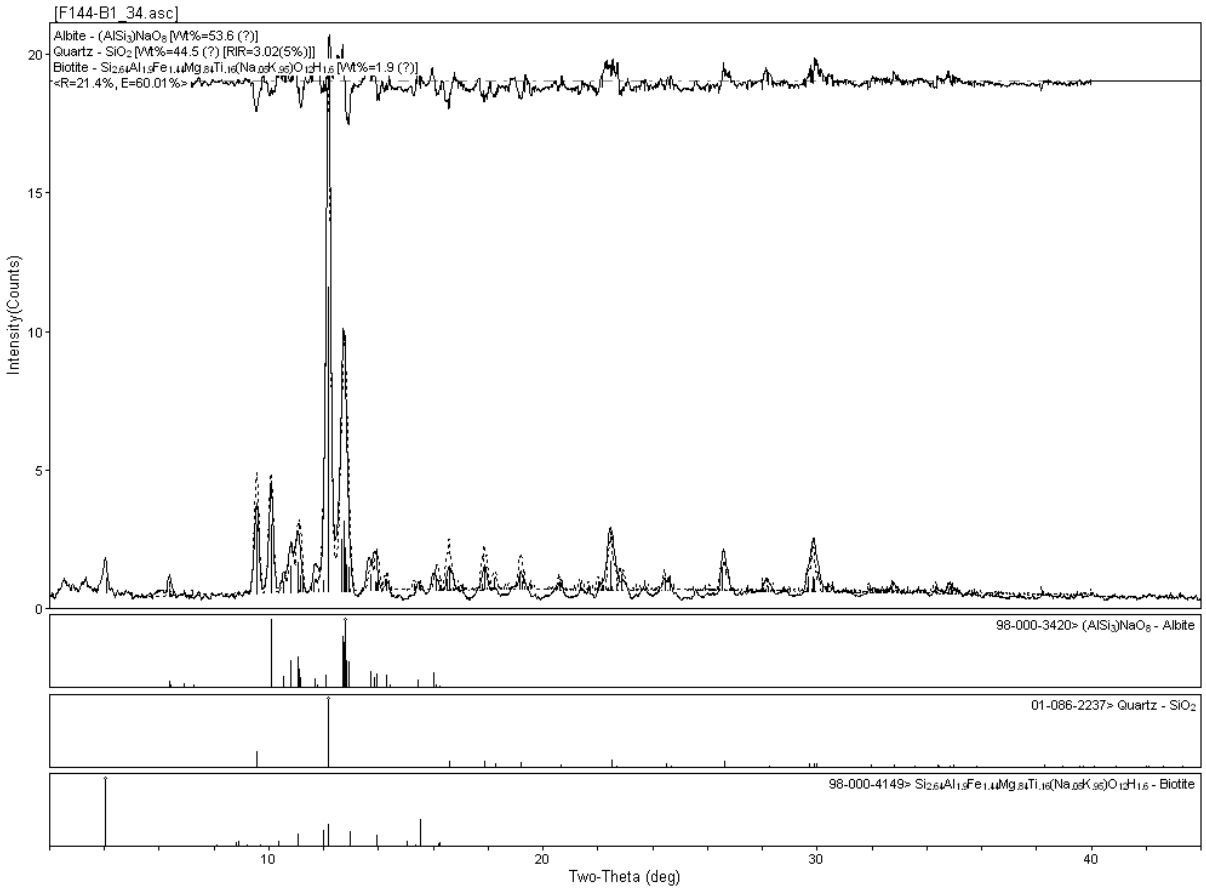

Fig. 8-8: XRD pattern for F144-B1_34 (granite).

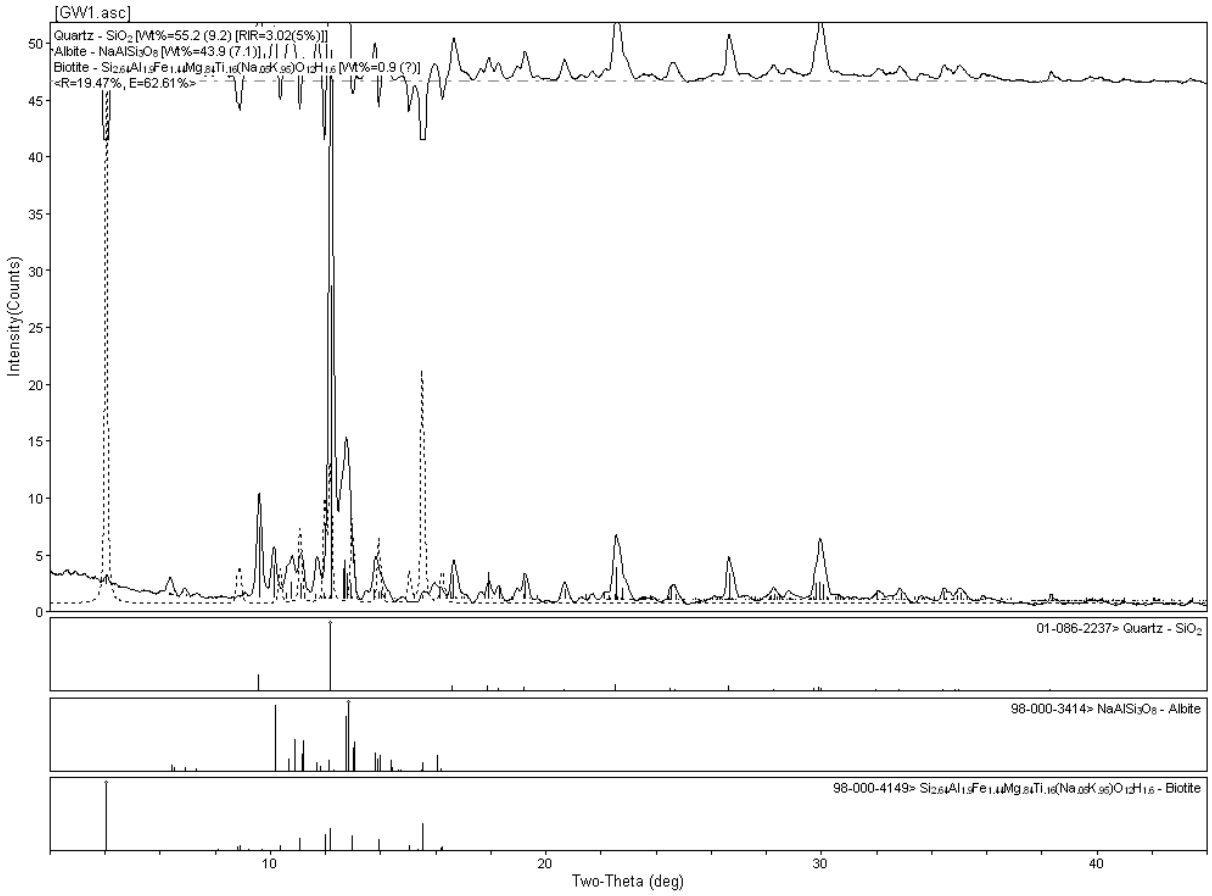

Fig. 8-9: XRD pattern for GW1 (granite).

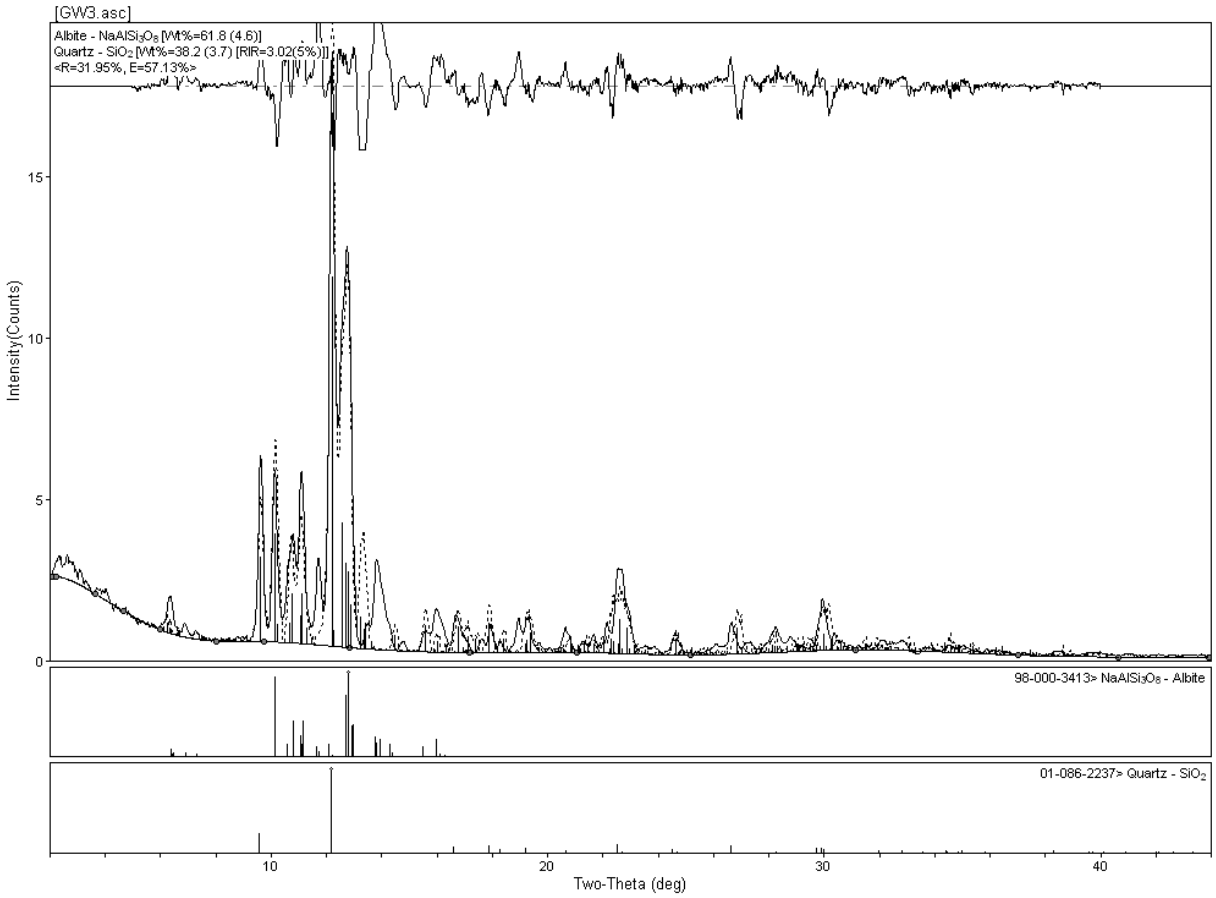

Fig. 8-10: XRD pattern for GW3 (granite).

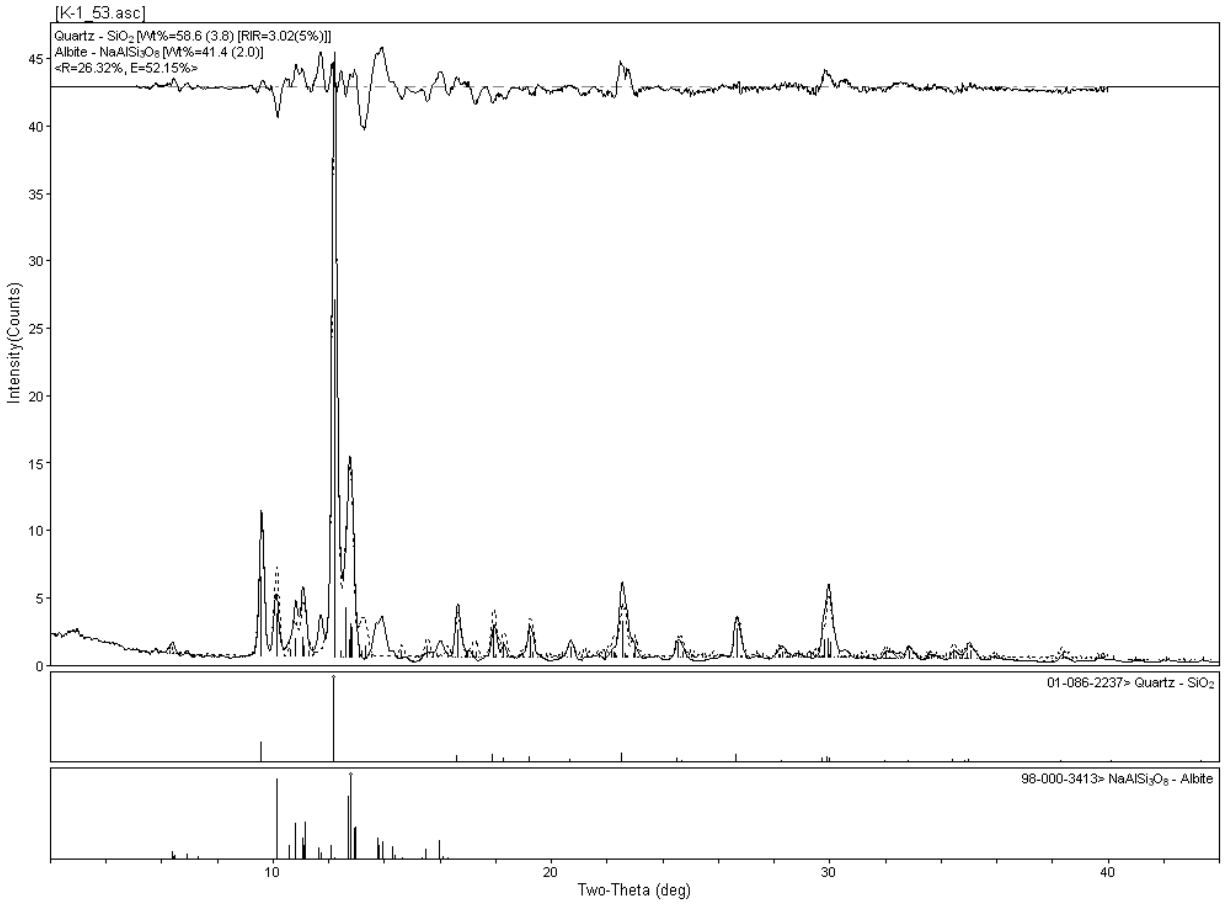

Fig. 8-11: XRD pattern for K-1_53 (granite).

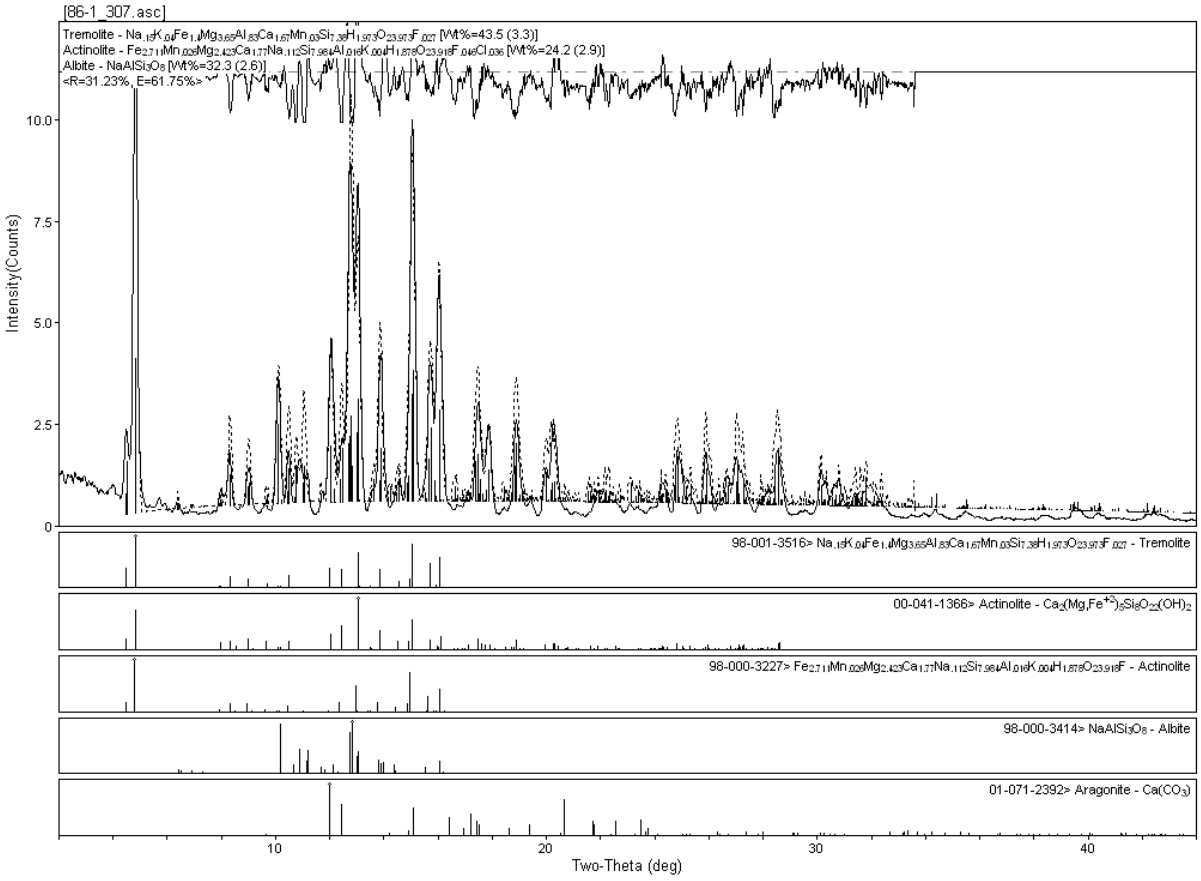

Fig. 8-12: XRD pattern for 86-1_307 (greenstone).

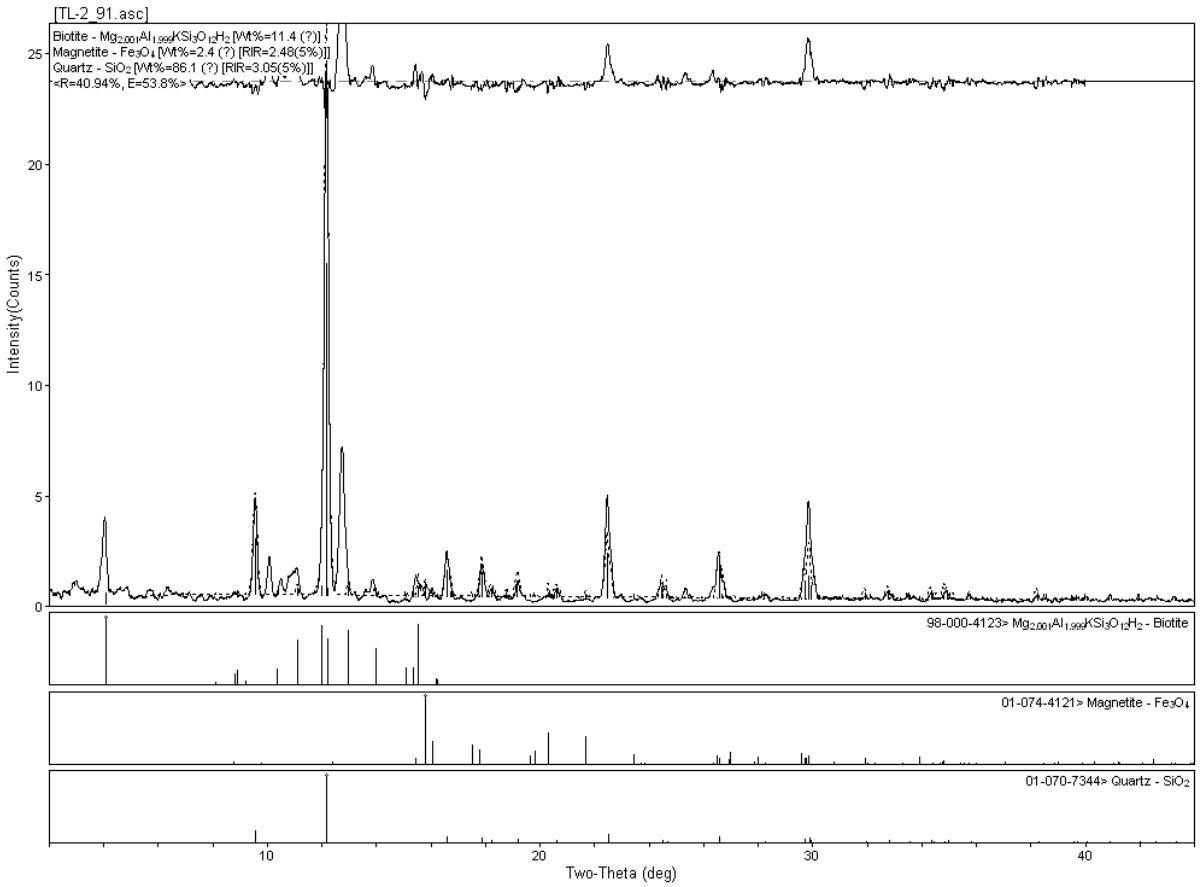

Fig. 8-13: XRD pattern for TL-2_91 (iron formation).

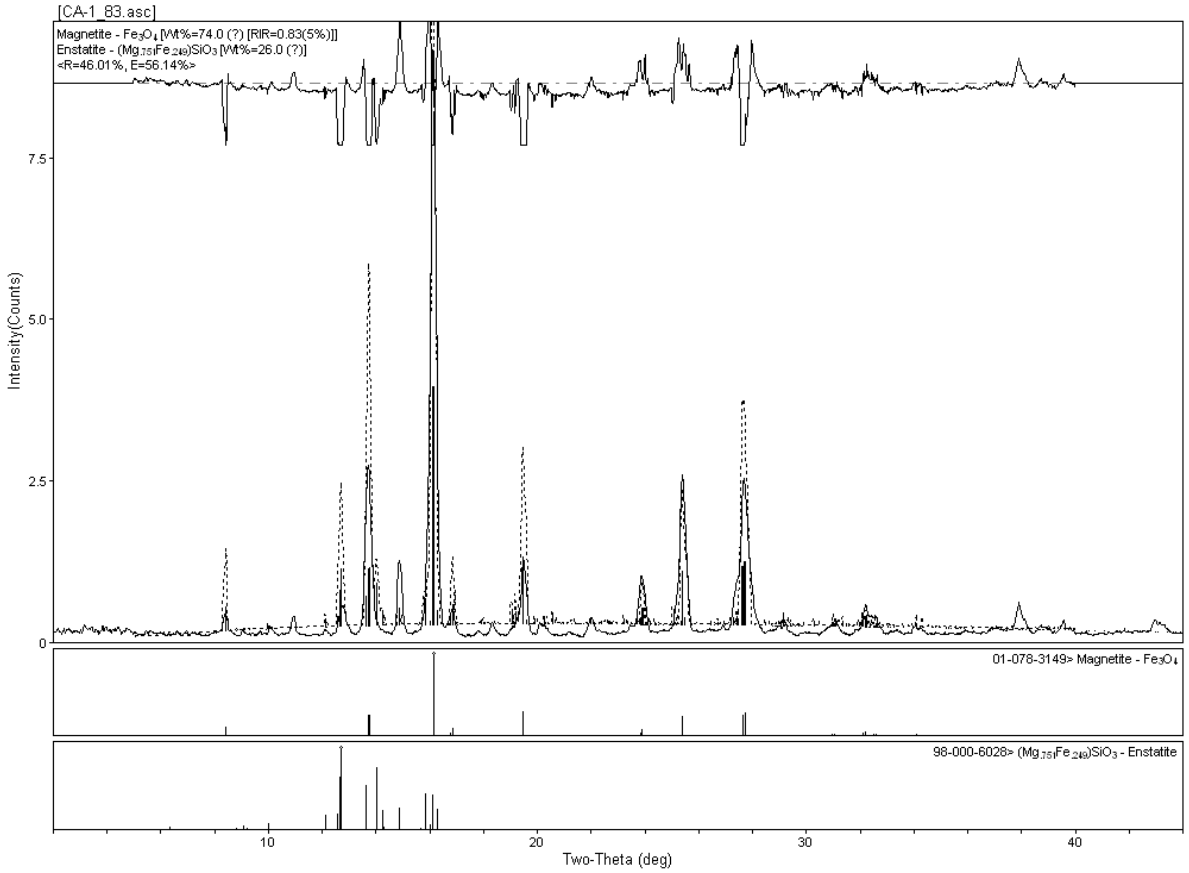

Fig. 8-14: XRD pattern for CA-1_83 (metagabbro).

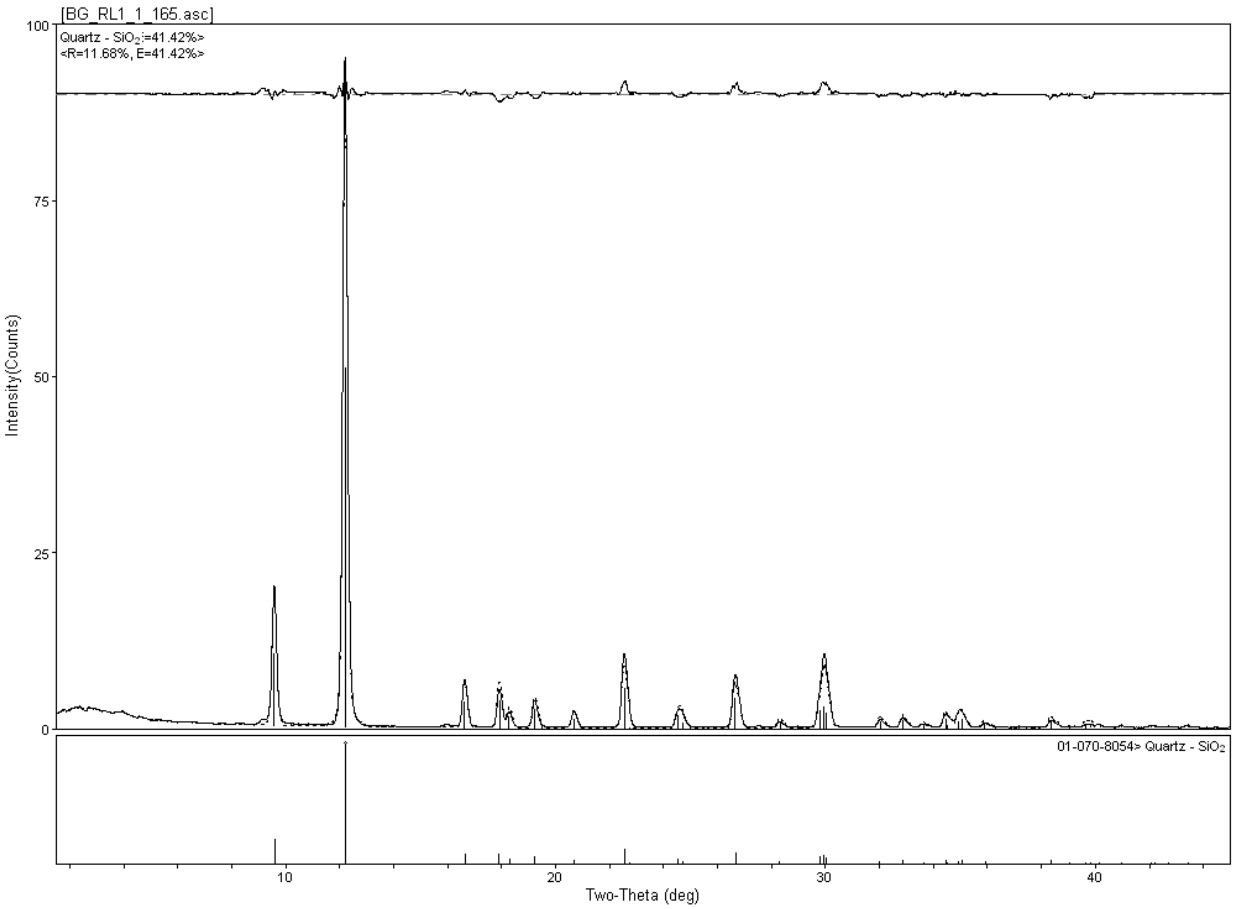

Fig. 8-15: XRD pattern for RL1-1_165 (quartzite).

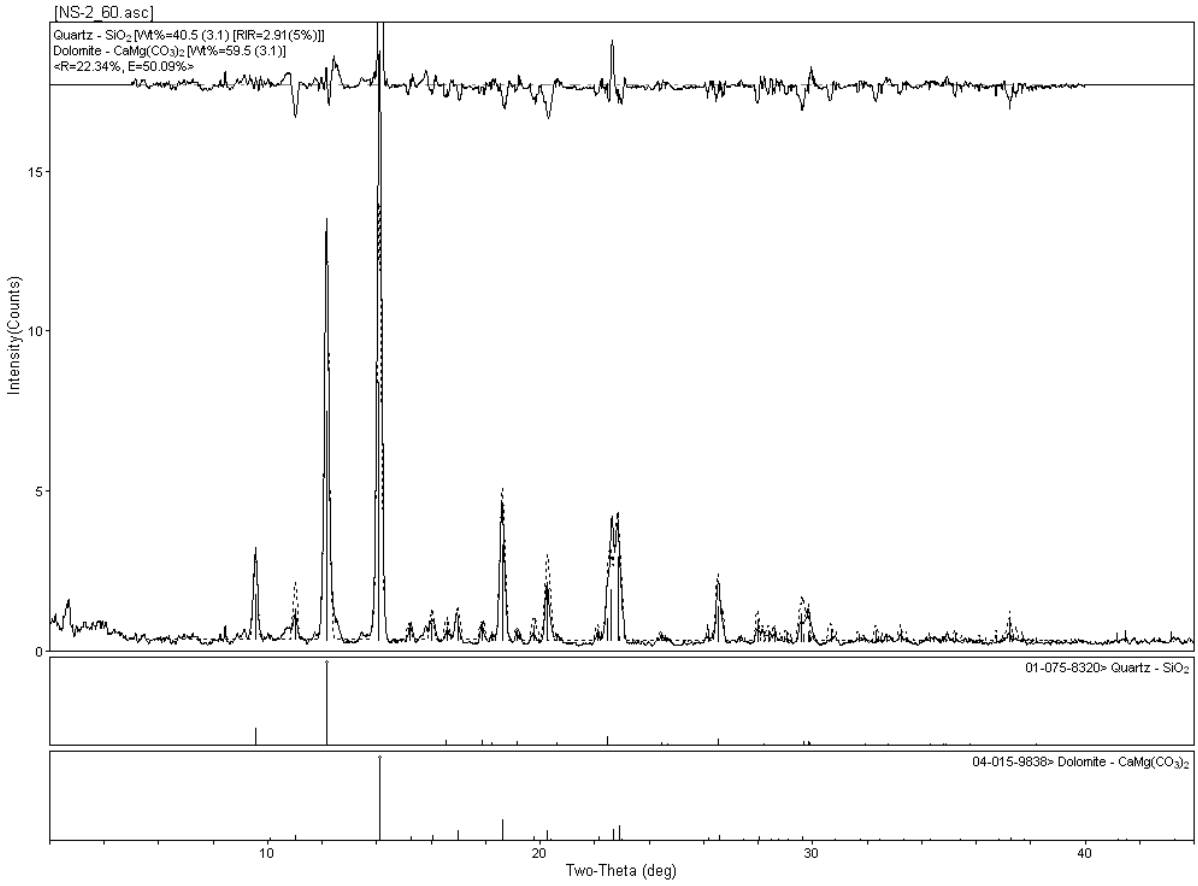

Fig. 8-16: XRD pattern for NS-2_60 (sandstone).

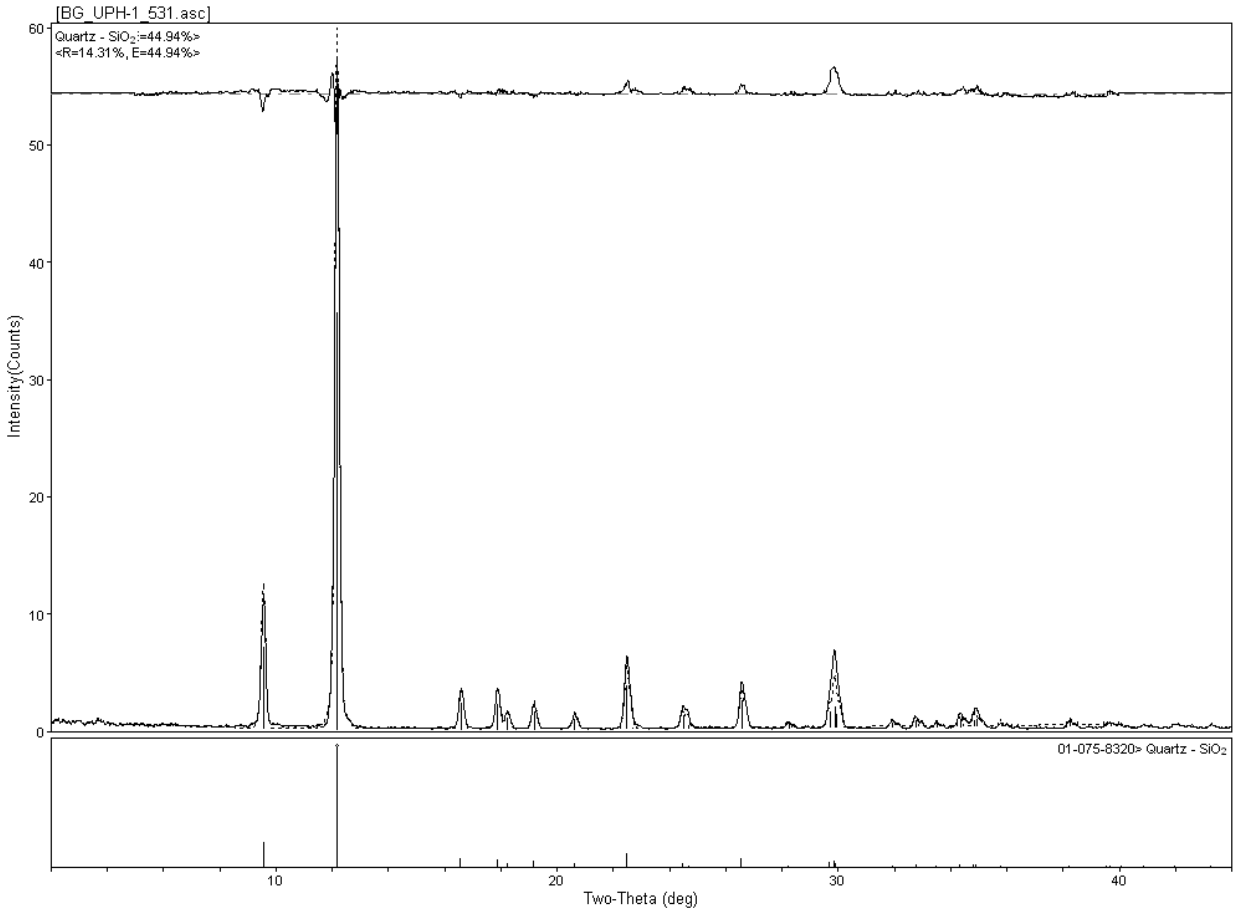

Fig. 8-17: XRD pattern for UPH-1_531 (sandstone).

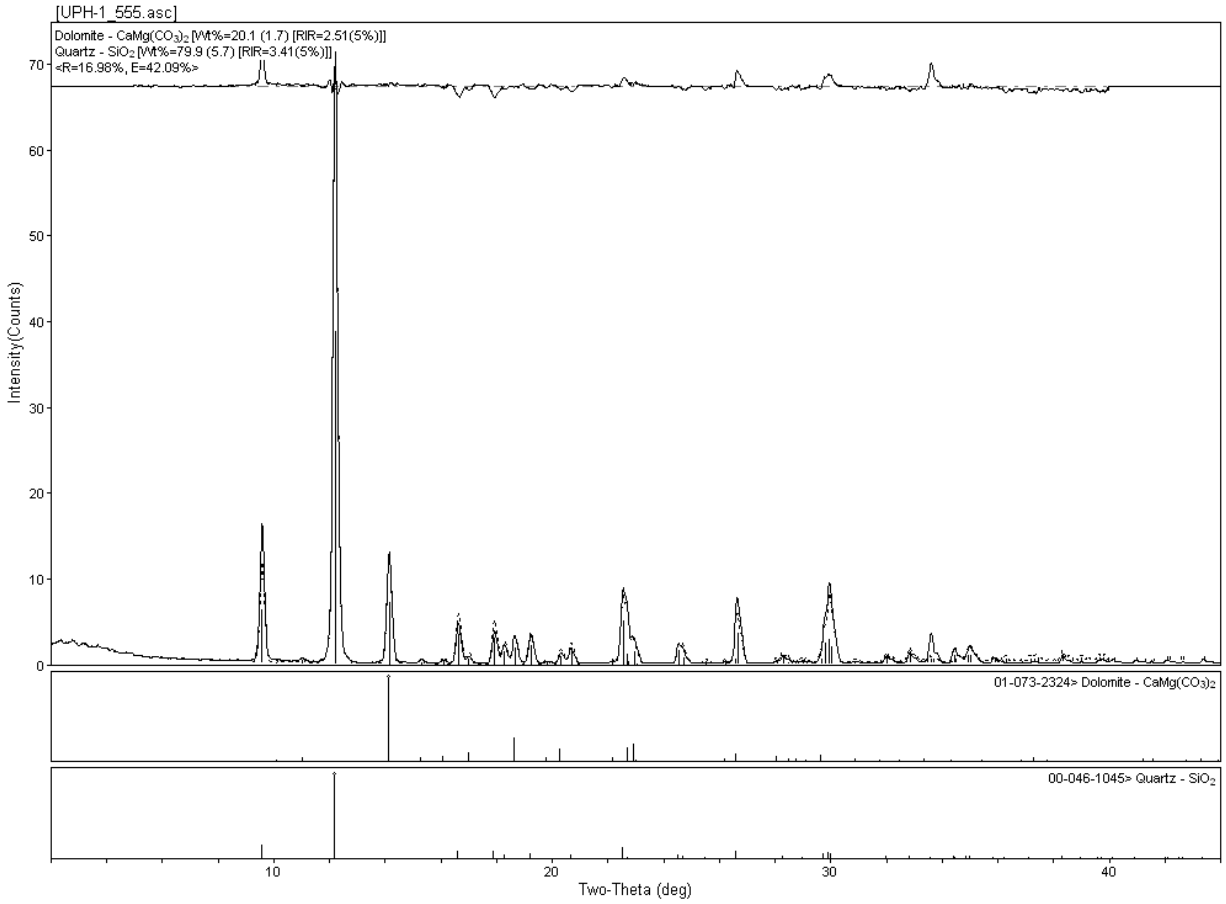

Fig. 8-18: XRD pattern for UPH-1_555 (sandstone).

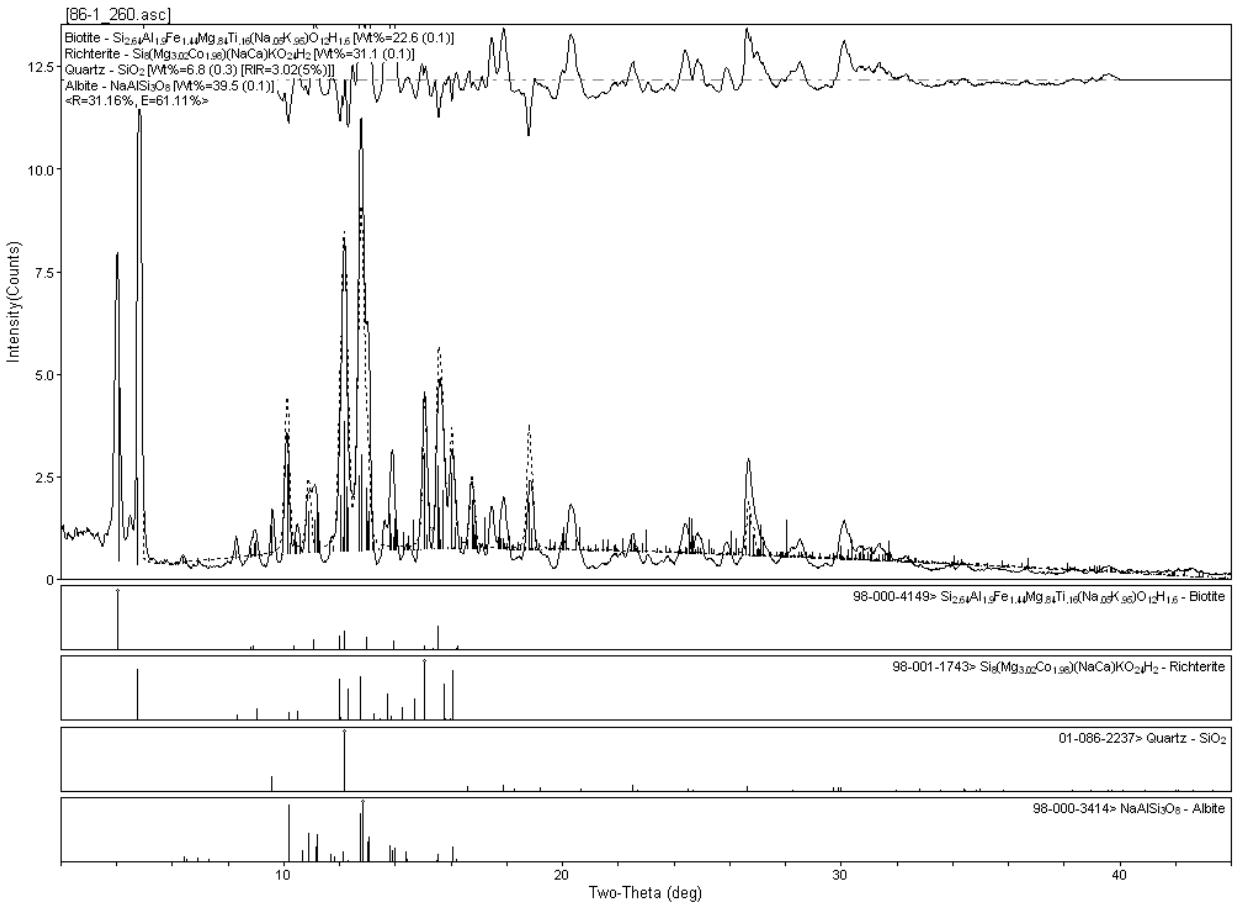

Fig. 8-19: XRD pattern for 86-1_260 (schist).

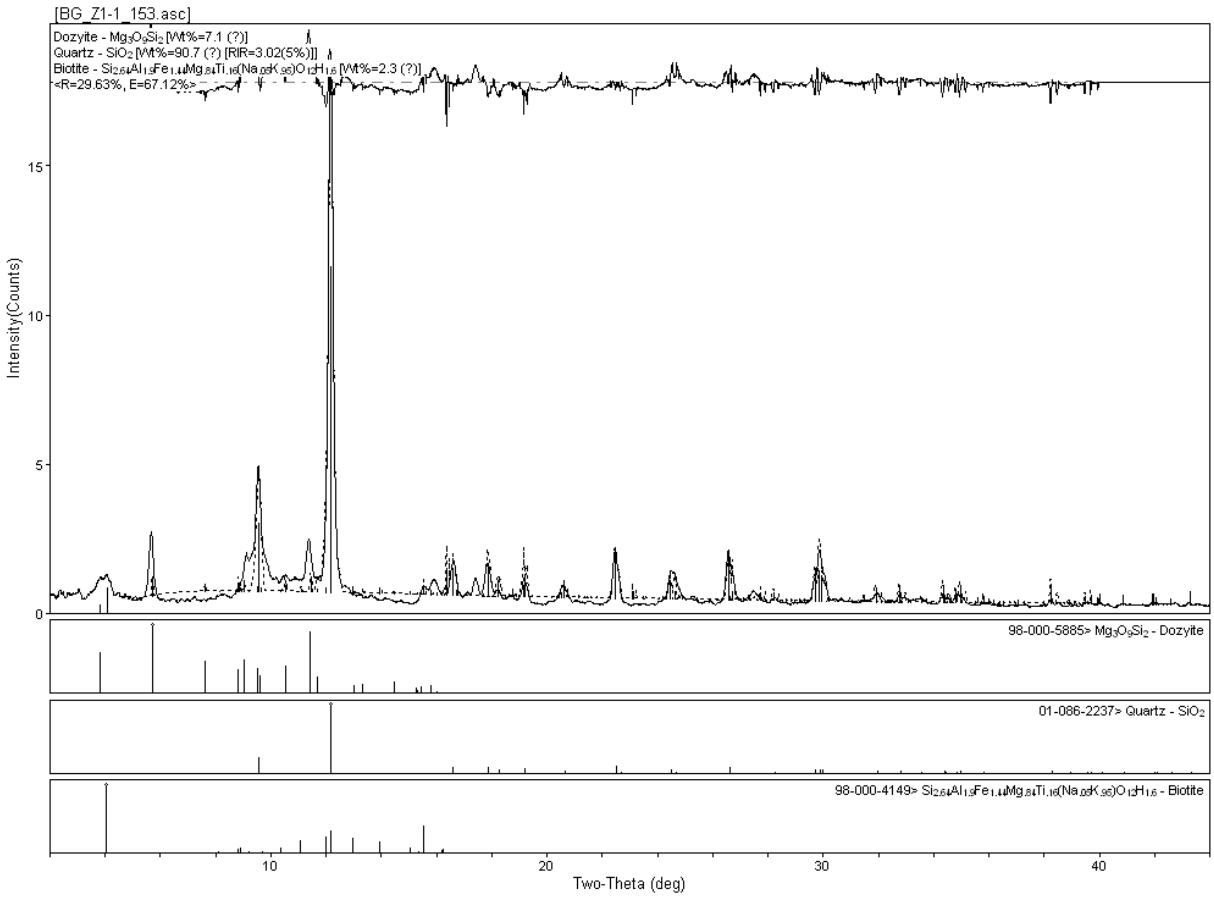

Fig. 8-20: XRD pattern for Z1-1_153 (schist).

9. APPENDIX C

9.1. Methods for KD-2 Pro Testing

All rock thermal conductivity tests were run using the RK-1 sensor (57mm in length, 4 mm in diameter). The testing procedure was based off of Decagon Devices Operator's Manual. The KD2 Pro procedure complies with ASTM D5334-08 and IEEE 442-03. Holes were drilled into each rock specimen using a Bosch SDS-plus Bulldog rotary hammer with a 3.97-mm drill bit. The specimens were left for at least 24 h to return to equilibrium with room temperature. Arctic Alumina thermal grease was then inserted into the drill hole before the RK-1 sensor was inserted. The RK-1 sensor was inserted and left in the specimen for five min to allow it to equilibrate with the specimen before the test was started. Each test was run using a ten-min read time. Fig. 9-1 shows how the KD2 Pro thermal probe was inserted into the rock specimens.

This testing method is based on the transient line heat source method to measure thermal conductivity (Decagon Devices, Inc., 2008-2012). The probe used in this method consists of a heater and temperature sensor. Ideal conditions for this method are as follows: the probe diameter is very small and the length is 100 times its diameter, the probe is in intimate contact with the surrounding materials, and the temperature of the material being tested does not change throughout the measurement. The temperature and thermal property calculations are based on the Single Needle Algorithm in which heat is applied to the probe for a time, t_h, and the

temperature is monitored during heating for an additional time t_h after heating. The temperature during heating is calculated from:

$$T = m_0 + m_2 t + m_3 lnt \quad [31]$$

where m_0 is the ambient temperature during heating, m_2 is the rate of background temperature drift, and m_3 is the slope of the line relating temperature to logarithm of temperature. The thermal conductivity is calculated from:

$$\lambda = \frac{q}{4\pi m_3} \quad [32]$$

Equations [31] and [32] act as long-time approximations of the exponential integral equations thus the final 2/3 of measured data are used for calculations. This reduces the effect of contact resistance on the calculations and allows for the problem to be solved using a non-linear least squares analysis.

Fig. 9-1: KD2 Pro set up with the RK-1 probe in Sample FR (Precambrian Andesite).

9.2. Results for KD-2 Pro Testing

Table 9-1: Thermal conductivity data obtained using the KD2 Pro RK-1 probe.

Sample ID	Formation	Rock Type	ρ [kg/m^3]	λ [W m^{-1} K^{-1}]	Err	Temp$_0$ [K]
86-1_260	Precambrian	Schist	2880	1.88	0.027	299.8
86-1_307	Precambrian	Greenstone	2956	1.83	0.024	298.0
CA-1_83	Precambrian	Metagabbro	3722	1.91	0.025	299.5
FR_240	Precambrian	Andesite	2808	1.59	0.025	297.8
GW1	Precambrian	Granite	2578	4.20	0.006	295.6
GW3-1	Precambrian	Granite	2616	4.16	0.008	295.1
TL-2_91	Iron Formation	Iron Formation	3004	1.34	0.004	298.6
UPH-1_555	Jordan	Sandstone	2347	2.26	0.023	298.1
UPH-1_618	St. Lawrence	Dolomite	2678	2.50	0.023	297.8

10. APPENDIX D

10.1. DISH Field Project

To fully evaluate the viability of a deep (300 m) geothermal exchange system in Wisconsin, a novel ground source heat pump system, the *Deep, Insulated, Single Hole geothermal heat pump* (DISH) system was installed and instrumented. The premise of the DISH system (Fig. 10-1) is to provide higher EWT found at greater depth to a heat exchanger, while still using the efficient and durable closed-loop system. Due to the high concentrations of radioactive elements in Wisconsin's granite bedrock, a higher EWT (> 305.15 K) is possible by drilling to greater depths than the typical ground source systems. Conventional ground heat exchangers consist of one or more U-shaped loops of high-density polyethylene (HDPE) tube (absorber pipes) inserted into a borehole. The heat transfer from the surrounding soil or rock to the heat carrier fluid (or vice versa) takes place through these absorber pipes.

The DISH system was installed at a residence in Adams County. A closed-loop GSHP is being installed in a 15-cm-diameter borehole using 5-cm SDR 11 HDPE fused earth loop. The loop was insulated to a depth of approximately 60 m with a PVC casing. A 300-m boring is being drilled, logged with geophysics, and fully instrumented to measure energy consumption and heat transfer through the system. The system will be evaluated for performance, efficiency (COP), and economic return in direct comparison to a series of shallower (55-m-deep) geothermal borings.

In addition, a thorough life cycle analysis (LCA) will be completed for cost, greenhouse gas (GHG) emissions and energy balance.

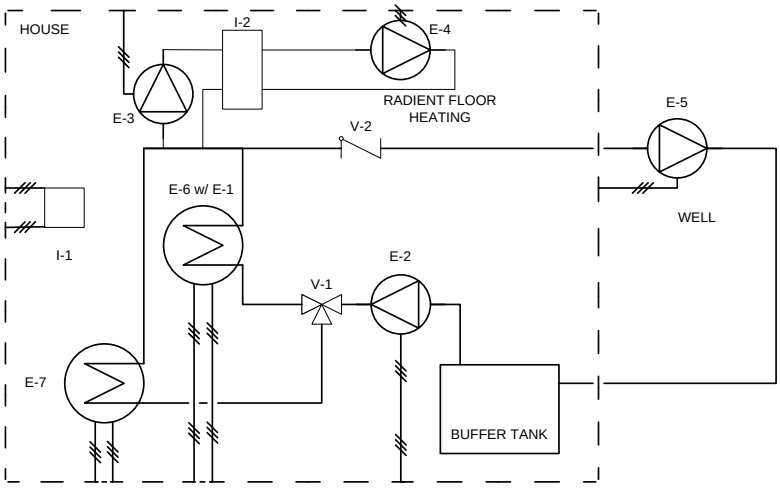

Legend:
E-1: Pump inside water to water heat exchanger
E-2 thru E-5: 115 V pump
E-6: Water to water heat exchanger
E-7: Water to air heat exchanger
I-1: Circuit breaker
I-2: Plate frame heat exchanger
V-1: Directional valve
V-2: Check valve

Fig. 10-1: DISH system.

10.2. Monitoring Instruments

The Adams County DISH geothermal exchange system was instrumented with monitoring equipment purchased from Campbell Scientific. Two CR10X dataloggers were installed to record all of the data collected at the field site, one for weather data and one for power consumption, water flow, and temperature. The datalogger used to monitor power consumption and water properties also uses two SDM-SW8A 8 Channel Switch Closure Modules to provide additional voltage pulse channels needed for power consumption measurements. The system has four 115 V, 0.65 A pumps, one 230 V, 30 A water-to-water heat exchanger, and one 230 V, 30 A water-to-air heat exchanger. The system is be connected to an electrical box running at 230 V, 60 A.

To determine energy use of the DISH system, current transducers and Advanced Pulse WattNodes were used. Four 5-A AC-powered current transducers (MAGNELAB SCT 0400-005) were attached to high efficiency Grundfos pumps (ALPHA 15-55 F/FR/SF/LC). Six 70-A AC-powered current transducers (ACT-0750-070) were attached to the WaterFurnace NV036 (7 series water to air) and NSW025 (water to water) heat exchangers, as well as to the electrical box housing the circuits for the system. These current transducers have magnets that clamp around the power source creating a magnetic field which then provides a voltage reading to the datalogger or WattNode. Four Advanced Pulse WattNodes (WBM-3Y-208-P) were used to measure power for each component of the system. In addition to monitoring power consumption, the water conditions were monitored to determine water

temperature and flow rate. For this, fiber optic cables, thermistors (Campbell Scientific 109SS-L) and five flow meters (Grundfos VFS 2-40 QT) were used. To monitor site weather conditions, a Campbell Scientific weather station was installed; this includes an anemometer and vane crossarm for wind speed and direction (03001 Wind Sentry), a temperature and relative humidity probe (CS500), a pyranometer for solar radiation (LI200X), and a tipping bucket rain gage for precipitation (TE525). The fully instrumented schematic of the DISH can be seen in Fig. 10-2 through Fig. 10-9.

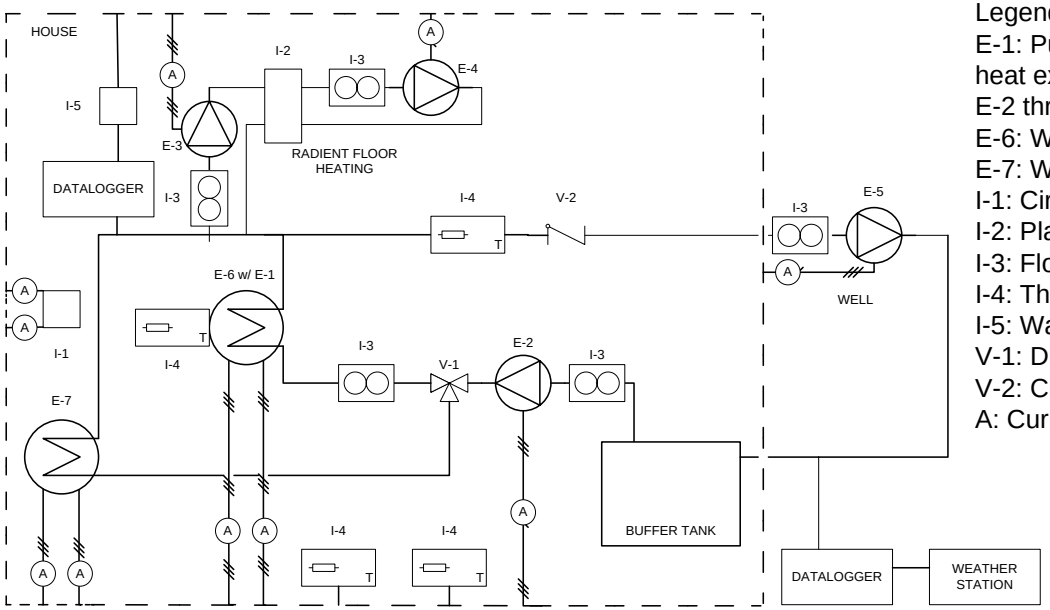

Legend:
E-1: Pump inside water to water heat exchanger
E-2 through E-5: 115 V pump
E-6: Water to water heat exchanger
E-7: Water to air heat exchanger
I-1: Circuit breaker
I-2: Plate frame heat exchanger
I-3: Flow meters
I-4: Thermistors
I-5: WattNodes
V-1: Directional valve
V-2: Check valve
A: Current sensor

Fig. 10-2: Instrumented DISH system schematic.

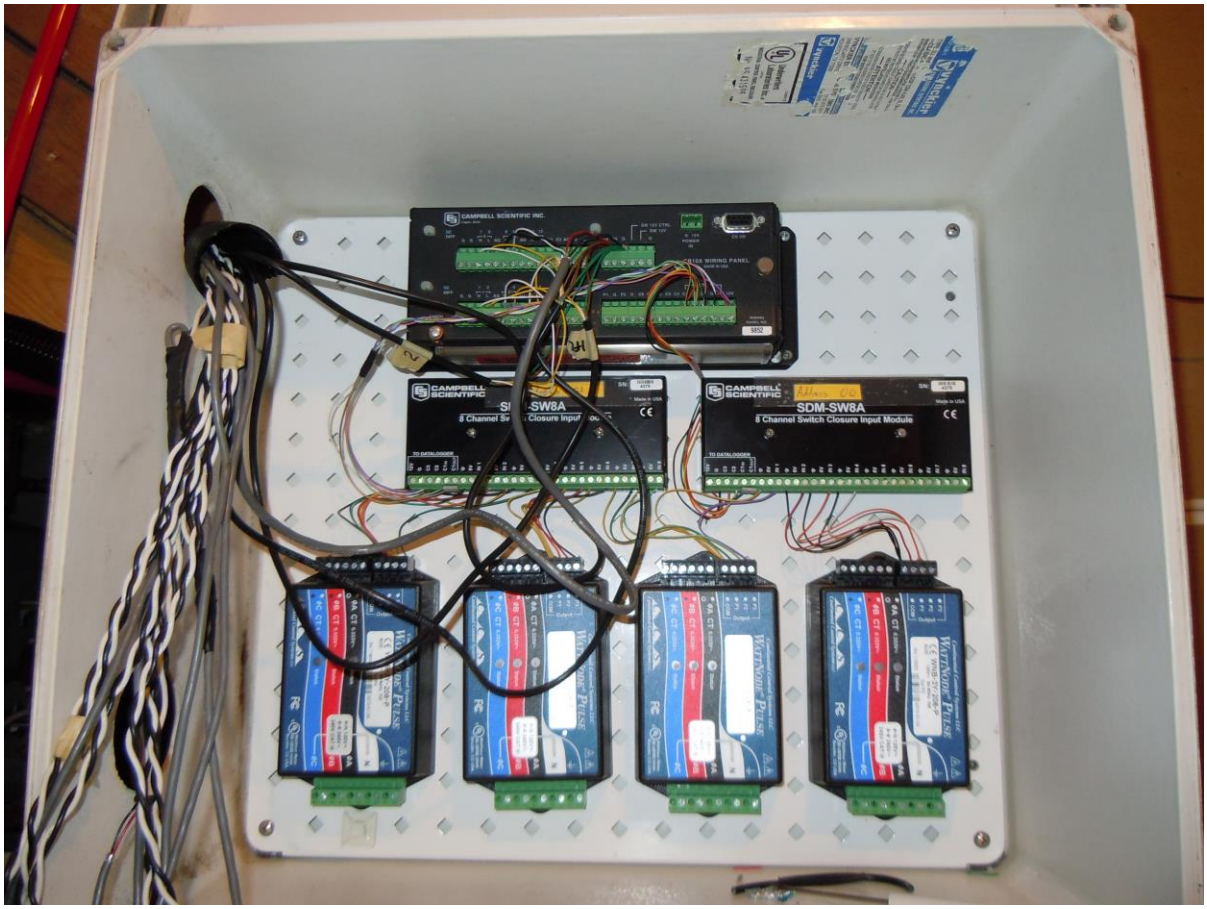

Fig. 10-3: WattNode, flow meter and current transducer hook up.

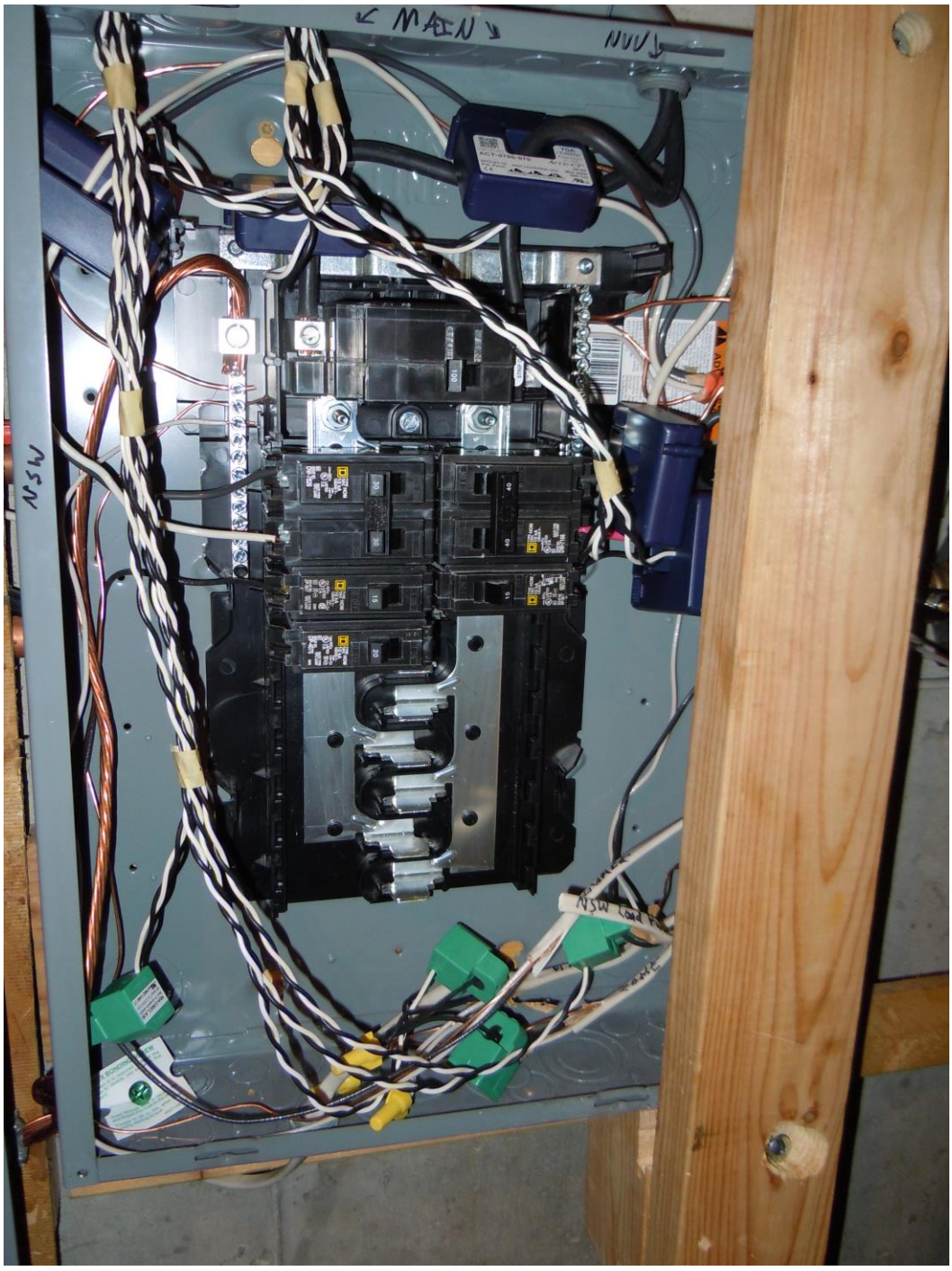

Fig. 10-4: Current transducer placement in electrical box.

Fig. 10-5: Flow meter (1, 2, 3, and 4) placement near water storage tanks.

Fig. 10-6: Flow meter (5) placement near water-to-water heat exchanger.

Fig. 10-7: Wind vane and solar radiation sensors on roof of house.

Fig. 10-8: Tipping bucket, relative humidity and temperature sensors on roof of house.

10.3. Theory and Data Reduction

10.3.1. Electrical Power

To determine the electrical power consumption of the DISH system, the voltage and corresponding current running through the system will be measured though the WattNodes, producing a power measurement. Power can be calculated using:

$$P = V * I \text{ [W]} \quad [33]$$

where P is power [W], V is voltage [V], and I is current [A]. The V and I of the system will be collected using voltage and current transducers.

The current transducers collect current measurements based on the theory of the Hall Effect. The Hall Effect is the production of a voltage difference across an electrical conduction that occurs when it is placed transverse to an electric current passing through the conductor and perpendicular to a magnetic field (Hall, 1879). The current transducers have a measurement multiplier of 0.015 with zero offset.

The power measurements will be obtained by using an Advanced Pulse WattNode which is a RMS AC watt-hour transducer with a pulse output (solid state relay course) proportional to kWh consumed. Each WattNode can handle power measurement of three system components. For each component, current sensors running from the power line were attached to the left side of the WattNode and wires spliced from the power line were attached to the right side. The current and voltage readings obtained by the WattNode are then converted into pulse outputs using one

or more photocouplers. Energy and power for the system can be calculated based on the following equations:

$$\frac{Wh}{Pulse} = \frac{CTamps}{40} \quad [34]$$

$$E = \frac{Wh}{Pulse} * PC \text{ [W-hr]} \quad [35]$$

$$P = \frac{Wh}{Pulse} * 3600 * PF \text{ [W]} \quad [36]$$

where CTamps is the current transducer amperage rating [A], PC is the WattNode pulse count, and PF is the WattNode pulse frequency.

10.3.2. Water Temperature

Some water temperature measurements will be taken using a thermistor temperature probe (109SS-L). Thermistors are thermally sensitive resistors composed of a semiconductor material that changes its resistance with temperature (Dunnicliff, 1988). In response to the excitation voltage of 2500 mV prescribed, the datalogger will measure the voltage across the 24,900 Ω resistor (Campbell Scientific, Inc., 1995-2007). The resistance of the thermistor (R_T) can then be corrected to a temperature measurement (T) using:

$$T = \frac{1}{(1.13*10^{-3})+(2.34*10^{-4})*\ln(R_T)+(8.77*10^{-8})*(\ln(R_T))^3} \text{ [K]} \quad [37]$$

Each thermistor has error of ± 0.6 K.

Borehole water temperature measurements will be taken using a fiber optic DTS technique. This technique is based on the optical time domain reflection (OTDR) which uses laser pulses down the fibers to detect changes in temperature. When the fiber optic cables experiences a temperature change, the fibers expand or

contract, scattering the light from the laser pulse. The measured backscatter can then be correlated to a temperature value (Hartog & Gamble, 1991; Yamano & Goto, 2005).

10.3.3. Flow Rate

The Grundfos VFS 2-40 QT flow sensor is based on the principle of vortex shedding behind a bluff body (Grundfos). The bluff body is located in the middle of the vortex flow sensor within the path of the fluid. When the fluid passes the bluff body, disturbances in the flow (vortices) are created. Downstream from the bluff body, a micro-electromechanical systems (MEMS) sensor detects pressure pulses in the flowing fluid. The vortices created by the bluff body detach periodically from either side of the body and are carried downstream which creates zones of high or low pressure (Von Karman Vortex Street). The pressure differences match the frequency of the vortices and the length between the vortices corresponds to a defined fluid volume, thus the total flow can be calculated by counting the vortices as they pass. The MEMS sensor detects the pressure pulses generated by the vortices and converts the calculated flow volume into an electrical output single that the datalogger can read. The flow sensor on the flow meter has a multiplier of 0.01267 and an offset of -4.333, and the temperature sensor has a multiplier of 0.03333 and an offset of -16.667 (Grundfos).

10.3.4. Wind Speed and Direction

The anemometer has a multiplier of 0.750 and an offset of 0.2 (Campbell Scientific, Inc., 1995-2007). To determine the wind speed from the anemometer cup wheel output frequency (f_o (Hz)), the following should be used:

$$v = (0.7500 * fo) + 0.2 \text{ [m/s]} \quad [38]$$

To get wind direction, the wind vane uses a 10 kΩ azimuth potentiometer (Campbell Scientific, Inc., 1995-2007) in a half bridge circuit as shown in Fig. 10-9. Using the EX-DEL-SE (P4) Instruction, the datalogger will output the measured voltage, V_s. This occurs because Instruction 4 outputs a precise excitation voltage (V_x) and measures the voltage between the wiper (R_s) and the analog ground (V_s). The resistance between R_s and V_s varies with direction and can be related with:

$$V_s = \frac{Vx*Rs}{Rt+Rs} \text{ [V]} \quad [39]$$

R_s will reach its maximum value just before the wind vane crosses over from the west side of north to the east side of north (at this point R_s = 0 Ω). At an excitation voltage (V_x) of 2500 mV, V_s reaches its maximum value. Thus, the multiplier to convert V_s into degrees is 355 degrees/2500 mV = 0.142 degrees/mV with an offset of zero (for the CR10X).

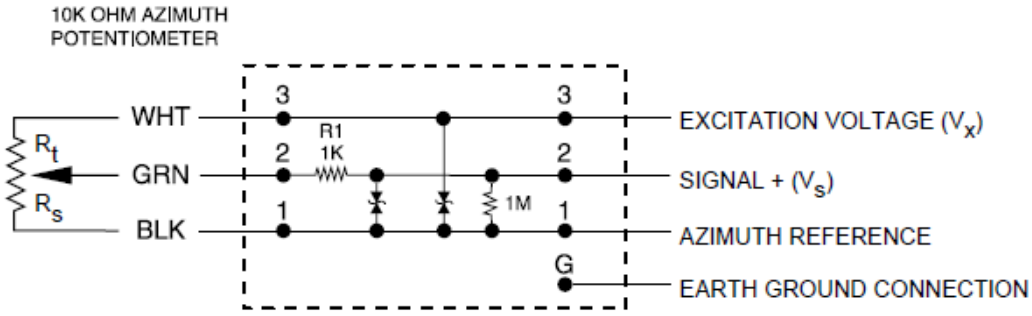

Fig. 10-9: Campbell Scientific 03001 Wind Sentry's wind vane potentiometer in a half bridge circuit (Campbell Scientific, Inc., 1995-2007).

10.3.5. Air Temperature and Relative Humidity

The CS500 measures air temperature and relative humidity (Campbell Scientific, Inc., 1995-2007). The air temperature measurement by the temperature probe has an offset and multiplier of 0.1 degrees/mV and -40 K respectively. Thus, the measurements recorded by the datalogger can be directly corrected into physical air temperature. Similarly, the relative humidity probe has a multiplier of 0.1 %/mV with zero offset and can also be directly corrected into physical relative humidity.

10.3.6. Solar Radiation

The LI200X Pyranometer measures the incoming solar radiation using a silicon photovoltaic detector (Campbell Scientific, Inc., 1995-2007). The photovoltaic detector outputs a short-circuit current that is directly proportional to the incident solar radiation (Kerr et al., 1967). The output current is then converted into voltage by a shunt resistor. This allows the datalogger to directly collect sun and sky radiation measurements made by the pyranometer. To determine solar radiation, the values collected by the datalogger must be multiplied by 200 to obtain an average energy flux density in [W/m^2].

10.3.7. Precipitation

Precipitation measurements will be made by the Campbell Scientific TE525 Tipping Bucket Rain Gage. This bucket has a 15.24-cm collector that will tip when full, activating a switch closure that is output to the datalogger (Campbell Scientific, Inc., 1995-2007). Each bucket tip correlates to 0.254 mm of rainfall.

10.4. Future Work

Collection and analysis of data from the DISH site must be completed. Sensor offsets and multipliers were accounted for during datalogger programming but should be verified. With the collected data, the DISH system will be evaluated for performance, efficiency (COP), and economic return. In addition, a thorough LCA will be completed for cost, GHG emissions, and energy balance.

REFERENCES

ASHRAE. (2007). Geothermal Energy. In *2007 ASHRAE Handbook - HVAC Applications.* American Society of Heating, Refrigerating and Air-Conditioning Engineers.

ASTM International. (2009). *Standard Test Method for Thermal Conductivity of Solids by Means of the Guarded-Comparative-Longitudinal Heat Flow Technique.* West Conshohocken, PA: ASTM International.

Attig, J. W., Bricknessl, M., Carson, E. C., Clayton, L., Johnson, M. D., Mickelson, D. M., & Syverson, K. M. (2011). *Glaciation of Wisconsin: Educational Series 36, Fourth edition.* Madison, WI: Wisconsin Geological and Natural History Survey.

Blackwell, D. D., Negraru, P. T., & Richards, M. C. (2007). Assessment of the Enhanced Geothermal System Resource Base of the United States. *Natural Resources Research*, 283-308.

Campbell Scientific, Inc. (1995-2007). Instruction Manuals. Logan, UT: Campbell Scientific, Inc.

Čermák, V., & Rybach, L. (1982). Thermal Properties. In K.-H. Hellwege, *Landolt-Bornstein numerical data and functional relationships in science and technology: New Series, Group V. Geophysics and Space Research, v. 1 Physical Properties of Rocks, Subvolume a: Springer-Verlag* (pp. 305-371). Berlin.

Clauser, C. (2009). Heat Transport Processes in the Earth's Crust. *Surveys in Geophsyics*, 163-191.

Clauser, C., & Huenges, E. (1995). Thermal Condcutivity of Rocks and Minerals. In T. Ahrens, *Rock Physics and Phase Relations - a Handbook of Physical Constants, AGU Reference Shelf, Vol. 3* (pp. 105-126). Washington.

Danko, G., & Mousset-Jones, P. (1989). A Simultaneous Measurement of In-Situ Thermal Conductivity and Diffusivity at the Waldo Mine. *Proceedings of the 4th US Mine Ventilation Symposium*, (pp. 287-296). Berkeley, CA.

Danko, G., & Mousset-Jones, P. (1991). A Probe Method for Measuring In Situ Rock Thermophysical Properties. *High Lever Radioactive Waste Management* (pp.

555-563). Las Vegas, Nevada: American Society of Civil Engineers and the American Nuclear Society.

Dean, R., & Dixon, W. (1951). Simplified Statistics for Small Numbers of Observations. *Analytical Chemistry*, 636-638.

Decagon Devices, Inc. (2008-2012). *KD2 Pro Thermal Properties Analyzer Operator's Manual Version 12.* Pullman, WA: Decagon Devices, Inc.

Department of Energy. (2013, February 20th). *Choosing and Installing Geothermal Heat Pumps*. Retrieved from ENERGY.GOV: http://energy.gov/energysaver/articles/choosing-and-installing-geothermal-heat-pumps

Dickie, E. (2010). *Energy Exchange.* Canada.

Dickson, M. H., & Fanelli, M. (2004). *What is Geothermal Energy.* Pisa, Italy: International Geothermal Association.

Dott, R. H., & Attig, J. W. (2004). *Roadside Geology of Wisconsin.* Missoula, Montana: Mountain Press Publishing Company.

Dunnicliff, J. (1988). *Geotechnical Instrumentation for Monitoring Field Performance.* United States of America: John Wiley & Sons, Inc.

Eklöf, C., & Gehlin, S. (1996). *TED: A Mobil Equipment for Thermal Response Test.* Luleå, Sweden: Luleå University of Technology.

Energy Information Administration. (2011). *Annual Energy Review 2011.* Washington: Department of Energy.

Figliola, R. S., & Beasley, D. E. (2000). *Theory and Design for Mechanical Measurements: Third Edition.* John Wiley & Sons, Inc.

Grundfos. (n.d.). *Grundfos Data Sheet: VFS 2-40 QT.* Bjerringbro, Denmark: Grundfos.

Grundfos. (n.d.). *Grundfos Direct Sensor: Vortex flow.* Bjerringbro, Denmark: Grundfos.

Hall, E. (1879). On a New Action of the Magnet on Electric Currents. *American Journal of Mathematics*, 287-292.

Hanley, E., Dewitt, D., & Roy, R. (1987). The Thermal Diffusivity of Eight Well-Characterized Rocks for the Temperature Range 300-1000 K. *Engineering Geology*, 31-47.

Hartog, A., & Gamble, G. (1991). Photonic distributed sensing. *Physics World*, 45-49.

Horai, K., & Simmons, G. (1969). Thermal Conductivity of Rock-Forming Minerals. *Earth and Planetary Science Letters 6*, 359-368.

Jaupart, C., & Mareschel, J. (2011). *Heat Generation and Transport in the Earth.* New York: Cambridge University Press.

Kavanaugh, S., Rafferty, K., & Geshwiler, M. (1997). *Ground-source heat pumps: Design of geothermal systems for commercial and institutional buildings .* Atlanta: American Society of Heating, Refrigerating and Air-Conditioning Engineers.

Kerr, J., Thurtell, G., & Tanner, C. (1967). An Integrating Pyranometer for Climatological Observer Stations and Mesoscale Networks. *Journal of Applied Meteorology*, 688-694.

LaBerge, G. L. (1984). The Geologic History of Wisconsin. *Rocks and Minerals, volume 59*, 61-73.

Lund, J., Sanner, B., Rybach, L., Curtis, R., & Hellström, G. (2004, Septermber). GEOTHERMAL (GROUND-SOURCE) HEAT PUMPS A WORLD REVIEW. *GHC Bulletin*, pp. 1-10.

Mursky, G., Anderson, J., Cook, T., & Meddaugh, W. (1988). *Uranium and thorium data for selected Precambrian rock units in Northern Wisconsin.* Madison, Wisconsin: University of Wisconsin-Extension Geological and Natural History Survey.

Neuerburg, G. (1955). Uranium in ingenous rocks of the united states. *Geology of Uranium and Thorium, International Conference* (pp. 55-64). Geneva, Switzerland: United States Government Printing Office.

Niencheski, H., & Müller, F. (2008). Heat Transfer Study in a Rig of Thermal Conductivity Measurement Based on ASTM E1225 Standard. *ENCIT.* Belo Horzonte, MG: ABCM.

Omer, A. M. (2008). Ground-source heat pumps systems and applications. *Renewable and Sustainable Energy Reviews*, 344-371.

Pansini, A. (1999). *Electrical Transformers and Power Equipment, 3rd ed.* Lilburn, GA: The Fairmount Press, Inc.

Penn, G. (2000). *Emissions and Economic Analysis of Ground Source Heat Pumps in Wisconsin.* Energy Center of Wisconsin.

S.W. Bailey X-ray Diffraction Laboratory, Dept of Geoscience UW-Madison. (2011). *RIGAKU Rapid II Operating Instructions, Version 1.* Madison, WI.

Schärli, U., & Rybach, L. (2001). Determination of specific heat capacity on rock fragments. *Geothermics*, 93-110.

Schneider, A. F. (1983). Wisconsinan Stratigraphy and Glacial Sequence in Southeastern Wisconsin. *Geoscience Wisconsin, volume 7*, 59-85.

Science First. (2003). 15-120 Aneroid Calorimeter Instructions and Applications. Buffalo, NY: Science First.

Slifka, A. (2000). Thermal-Conductivity Apparatus for Steady-State, Comparative Measurement of Ceramic Coatings. *Research of the National Institute of Standards and Technology*, 591-605.

Smith, G. L., & Simo, J. A. (1997). Carbonate Diagenesis and Dolomitization of the Lower Ordovician Prairie Du Chien Group. *Geoscience Wisconsin, volume 16*, 1-16.

Stacey, F. D., & Davis, P. M. (2008). *Physics of the Earth: Fourth Edition.* Cambridge: Cambridge University Press.

Touloukain, Y., Judd, W., & Roy, R. (1981). *Physical Properties of Rocks and Minerals, vol. II-2.* Perdue Research Foundation.

Turcotte, D. L., & Schubert, G. (1982). *Geodynamics: Applications of Continuum Physics to Geological Problems.* New York: John Wiley & Sons.

Tye, R., & Riko, U. (1996). Reference Materials and Transfer Standars for Use in Measurements on Low Thermal Conductivity Materials and Systems. *Thermal Conductivity 23*, 419-430.

U.S. Energy Information Administration. (2012, May 17). *Wisconsin: Data*. Retrieved from eia Idependent Statistics & Analysis Web site: http://www.eia.gov/state/state-energy-profiles-data.cfm?sid=WI

US Environmental Protection Agency. (1993). *Space Conditioning: The Next Frontier.* US Environmental Protection Agency.

US Environmental Protection Agency. (1997). *A short primer and environmental guidance for geothermal heat pumps.* US Environmental Protection Agency.

US Environmental Protection Agency. (2013, February 20th). *Energy Star Website*. Retrieved from http://www.energystar.gov/index.cfm?fuseaction=find_a_product.showProductGroup&pgw_code=HP

Van Schmus, W. (1995). Natural Radioactivity of the Crust and Mantle. In T. Ahrens, *Global Earth Physics: A Handbook of Physical Constants* (pp. 283-291). Washington, D.C.: American Geophysical Union.

Vosteen, H., & Schellschmidt, R. (2003). Influence of temperature on thermal conductivity, thermal capacity and thermal diffusivity for different types of rock. *Physics and Chemistry of the Earth*, 499-509.

Walker, B. (2012). Personal Communication.

Waples, D. W., & Waples, J. S. (2004). A Review and Evaluation of Specific Heat Capacities of Rocks, Minerals, and Subsurface Fluids. Part 1: Minerals and Nonporous Rocks. *Natural Resources Research*, 97-122.

WaterFurnace International, Inc. (2012). *7 Series 700A11 Specification Catalog.* Fort Wayne, IN: WaterFurnace International, Inc.

Wenner, J. M., & Lloyd, M. A. (2006). Trace-Element Signatures and Techtonic Affinities of Proterozoic A-Type Granites and Rhyolites in Central Wisconsin. *Geoscience Wisconsin, volume 17*, 35-51.

Wisconsin Geological and Natrual History Survey. (2005, April 29). *Bedrock Geology of Wisconsin [map]*. Retrieved from Wisconsin Geological and Natrual History Survey: http://wisconsingeologicalsurvey.org/pdfs/pgszpdf/bedrock_geology.pdf

Wisconsin Office of Energy Independence. (2010). *2010 Wisconsin Energy Statistics.* Madison, WI: Wisconsin Office of Energy Independence.

Wisconsin Perspective. (2006). Ground-Source Heat Pumps. *A Publication for Wisconsin/ U.P. Plumbing-HVAC-Mechanical and Related Industries*, p. 14.

Yamano, M., & Goto, S. (2005). Long-term monitoring of the temperature profile in a deep borehole: Temperature variations associated with water injection experiments and natural groundwater. *Physics of the Earth and Planetary Interiors*, 326-334.